168
84

To the Graduate Council:

I am submitting herewith a thesis written by Mukund J. Godbole entitled "Rapid Solidification and Excimer Laser Processing Studies in Iron-based Alloys." I have examined the final copy of this thesis for form and content and recommend that it be accepted in partial fulfillment of the requirements for the degree of Master of Science, with a major in Metallurgical Engineering.

A Pedraza

Antonio J. Pedraza, Major Professor

We have read this thesis
and recommend its acceptance:

Ben S. Covino

D. H. Hownder

Accepted for the Council:

C. W. Minkel

Vice Provost
and Dean of The Graduate School

STATEMENT OF PERMISSION TO USE

In presenting this thesis in partial fulfillment of the requirements for a Master's degree at The University of Tennessee, Knoxville, I agree that the Library shall make it available to borrowers under rules of the Library. Brief quotations from this thesis are allowable without special permission, provided that accurate acknowledgement of the source is made.

Permission for extensive quotation from or reproduction of this thesis may be granted by my major professor, or in his absence, by the Head of the Interlibrary Services when, in the opinion of either, the proposed use of the material is for scholarly purposes. Any copying or use of the material in this thesis for financial gain shall not be allowed without my written permission.

Signature 

Date June 1986

RAPID SOLIDIFICATION AND EXCIMER LASER PROCESSING STUDIES IN IRON-BASED ALLOYS

A Thesis

Presented for the

Master of Science

Degree

The University of Tennessee, Knoxville.

Mukund J. Godbole

June 1986

DEDICATION

I dedicate this thesis to my beloved parents,

Aai and Bhau

ACKNOWLEDGEMENTS

The author would like to express deep gratitude to his major professor, Dr. A. J. Pedraza, for his unceasing guidance, patience, and support through the entire duration of this research. His constant encouragement and personal involvement were important ingredients that made this effort truly enjoyable.

The author is thankful to Dr. D. H. Lowndes and Dr. B. F. Oliver for making the equipment available in carrying out this research and for the helpful discussions during the course of this research.

The financial support provided through teaching assistantship by the Department of Materials Science and Engineering, The University of Tennessee, Knoxville is gratefully acknowledged.

The help received from Mr. Ted A. Long, head of the departmental electronics shop, and his efficient group: Mr. Stephen A. Stiner, Mr. Michael R. Neal and Mr. Ronald L. Johnson in the X-ray and furnace equipment is deeply appreciated.

Thanks are extended to Mr. H. B. Thompson, head of the departmental machine shop and his helpful group: Mr. Jack French, Mr. Raymond Bellamy and Mr. Doug Fielden for their assistance in solving mechanical equipment problems.

Special gratitude is expressed to Mr. Bob L. McGill for his help with the scanning electron microscope, and to Mr. Albert W. J. Carter and Ms. Aileen Cagle for supplying laboratory materials.

Use of the electron microscope facilities at the Oak Ridge National Laboratory is appreciated. Special thanks are due to Mr. Jerry

Lehman and Dr. Jim Bentley for their assistance with the microscope. Scanning electron microscopy work performed by Mr. Ted Nolan and Ms. Mary Hughes is truly appreciated.

The author is grateful to the office staff: Ms. Phyllis Davis, Ms. Sancy Hail, Ms. Betty Frazier, Ms. Sue Turner, Ms. Phyllis Klindt, Ms. Kay Davis and Ms. Inez McDonald for their support and help with the official matters.

And at last as usual, the author would like to thank his fellow graduate students for their part in making this place what it is.

ABSTRACT

Pure iron was irradiated using ultraviolet pulsed excimer laser wavelengths of 249nm and 308nm, in order to study the effects of extremely high heating and cooling rates on the phase transformation sequence and upon the specimen surface. The thickness of the molten layer was found to be a function of the laser power output, reaching a maximum at 1.5μm for $4.5J/cm^2$. Surface damage in the form of the ripples also increased with the laser output power and became very pronounced between 3.5 and $4.7J/cm^2$, the maximum energy density used in the experiments. The optimum energy density, which gives uniform melting with the least surface damage, was determined to be $3.0J/cm^2$ and was used for all the subsequent experiments.

A surface sensitive X-ray diffraction (SSXD) technique was developed for studying structural changes in the near surface region (~1μm) and was tested on an $Fe_{80}B_{20}$ alloy which is a ready glass former. Using the SSXD technique, the thickness of the amorphous layer formed on the surfaces of alloys by laser irradiation treatment was measured precisely. It was determined that the ability of an alloy to amorphize is strongly dependent on the starting microstructure. Fe_3B metastable phase formed during splat quenching was identified and its role in the amorphization process was analysed. It was concluded that fine microstructure and the presence of the Fe_3B phase increase the glass forming ability of the $Fe_{80}B_{20}$ alloy system under pulsed laser irradiation.

Fe-Zr alloys with 5, 10, 12 and 15 at% Zr were processed with the 'hammer and anvil' apparatus. With sample weights of 40 mg or less,

the 10 and 12 at%Zr alloys amorphize on splat quenching, while 5 and 15 at%Zr remain crystalline independently of the sample weight. With sample weight of 80 mg, all four alloys render crystalline, though metastable, phases upon splat quenching. Ferrite and Fe_2Zr (an intermetallic that is metastable at the compositions used) were identified as the phases present in all of the as splat quenched crystalline samples, using the X-ray diffraction method. In samples that were partially amorphous, three different crystalline phases were identified by TEM and STEM as being embedded in the amorphous matrix.

Pulsed laser irradiation of as splat quenched crystalline samples gives amorphous structure in the composition range of 10 and 15 at% Zr.

TABLE OF CONTENTS

CHAPTER		PAGE
1.0	INTRODUCTION	1
2.0	INTERACTION OF LASER WITH METALS	4
2.1	Coupling of Laser Beam Energy with Metals	4
2.2	Concept of Laser Heating and Cooling	10
2.3	Dislocation Generation by Laser Irradiation	13
2.4	Surface Damage	15
3.0	METALLIC GLASSES	17
3.1	What are Metallic Glasses?	17
3.2	Techniques for Glass Formation	18
3.3	Glass Forming Alloy Systems	21
3.4	Kinetics of Glass Formation	22
4.0	IRON AND ITS ALLOYS	30
4.1	Pure Iron	30
4.2	Iron Base Alloy Systems	31
5.0	SAMPLE PREPARATION AND EXPERIMENTAL PROCEDURE	36
6.0	RESULTS	43
6.1	Pure Iron	43
6.2	Iron-Boron System	53
6.3	Iron-Zirconium System	64
7.0	DISCUSSION	86
7.1	Pure Iron	86
7.2	Iron-Boron System	94
7.3	Iron-Zirconium System	97

CHAPTER PAGE

8.0 CONCLUSIONS 103

8.1 Pure Iron 103

8.2 Iron-Boron System 103

8.3 Iron-Zirconium System 104

LIST OF REFERENCES 105

APPENDICES 111

APPENDIX 1 112

APPENDIX 2 117

VITA 119

LIST OF FIGURES

FIGURE PAGE

1. Variation of temperature with time at selected melt depths. 5
2. Normal spectral reflectance of Iron. 8
3. Melt depth versus total time for different uniform absorbed heat fluxes obtained via a numerical technique. 11
4. Apparatus for splat quenching technique. 20
5. a) Fe-B system, b) Crystal structure of stable and metastable phases in iron rich Fe-B alloys, c) Cu-Zr system, d) Pd-Si system. 23
6. Calculated variation of the logarithm of the frequency (in $cm^{-3}s^{-1}$) of homogeneous nucleation of crystals in an undercooled liquid with reduced temperature for various assignments of $\alpha\beta^{1/3}$. 26
7. Time-Temperature-Transformation curves (solid lines) and the corresponding Continuous-Cooling-Transformation curves (dashed lines) for the indicated systems. 28
8. Amorphous phase formation in Fe-Zr-B system and composition dependence of crystallization temperature. 35
9. A schematic ray diagram of the lens system used for obtaining a range of energy outputs. 38

FIGURE PAGE

10. A typical user program used in X-ray diffraction work. 41

11. Diffraction marks produced at the edge of the masking tape. 44

12. Uniform melting of the pure iron polished surface observed at 2.5J/cm^2. 45

13. An unmolten island in a laser irradiated pure iron sample. 47

14. Pure iron reflectivity measurement. 48

15. Pure iron sample irradiated with an energy density of 3.0J/cm^2. The left side of the image is irradiated while the right side is unirradiated. The single grain boundary runs through both regions. 50

16. Laue back-scattered X-ray diffraction patterns for pure iron single crystal sample before and after laser irradiation. 51

17. A schematic illustration of the 'step-by-step surface removal by mechanical polishing' method used to determine the melt depth. 52

18. Melt depth of the laser irradiated pure iron specimens as a function of the input energy density. 54

19. As sintered and annealed $Fe_{80}B_{20}$ structure showing precipitates of Fe_2B in ferrite matrix. 55

FIGURE PAGE

20. The X-ray diffractometer scan of the diffracted intensity vs. the 2θ angle for the as sintered and annealed sample of $Fe_{80}B_{20}$ alloy. 56

21. As splat quenched microstructure of the $Fe_{80}B_{20}$ alloy. 58

22. The X-ray diffractometer scan of the diffracted intensity vs. the 2θ angle for the splat quenched sample of $Fe_{80}B_{20}$ alloy. 59

23. The comparison of the X-ray diffraction patterns in as sintered and annealed condition and in as splat quenched condition. 60

24. Sintered and annealed $Fe_{80}B_{20}$ after laser irradiation. 62

25. The comparison of the X-ray diffraction patterns in the splat quenched condition before and after laser irradiation. 63

26. The X-ray diffractometer scan of the diffracted intensity vs. the 2θ angle for an amorphous ribbon of $Fe_{80}B_{20}$ alloy prepared by the melt spinning technique. 65

27. The X-ray diffractometer scan of the diffracted intensity vs. the 2θ angle for an as splat quenched amorphous and as splat quenched

FIGURE PAGE

crystalline sample of $Fe_{90}Zr_{10}$ alloy. 67

28. The Fe-Zr phase diagram 68

29. The cross-section of an $Fe_{90}Zr_{10}$ as splat quenched amorphous film showing the presence of a crystalline layer beneath each surface. 69

30. TEM image of an $Fe_{90}Zr_{10}$ as splat quenched amorphous sample showing a distribution of fine precipitates. The corresponding diffraction patterns in the amorphous matrix(left) and in the matrix with the precipitates(right). 70

31. TEM image of the spherulitic precipitates in the $Fe_{90}Zr_{10}$ as splat quenched amorphous film at four magnifications. 72

32. A diffraction pattern from a Zr-rich precipitate. 74

33. The lattice parameter vs. the composition curve for a metastable β-Zr phase showing an upward concave nature. 75

34. TEM image of the $Fe_{90}Zr_{10}$ as splat quenched amorphous film showing a dispersion of Fe-rich fine precipitates. 76

35. A diffraction pattern from an Fe-rich precipitate. 78

36. As splat quenched crystalline microstructure of the $Fe_{90}Zr_{10}$ alloy. 79

FIGURE PAGE

37. The X-ray diffraction pattern for an as splat quenched $Fe_{90}Zr_{10}$ alloy before and after laser irradiation. 80

38. The X-ray diffraction pattern for an as splat quenched $Fe_{85}Zr_{15}$ alloy before and after laser irradiation. 81

39. Microstructure of a crystallized amorphous film of an $Fe_{90}Zr_{10}$ alloy. 84

40. The amorphous layer formed on laser irradiation on an $Fe_{90}Zr_{10}$ alloy. 85

41. Schematic temperature vs. beam intensity curves showing the temperature fluctuation ΔT caused by a fluctuation in the beam intensity ΔI in various cases. 88

42. Position profiles of melt fronts in Si and Al after irradiation with a pulsed ruby laser. 91

CHAPTER 1

INTRODUCTION

Metallic glasses have generated a lot of interest lately, both at academic institutions and industrial research centers. Since their discovery by rapid solidification techniques, about 25 years ago, many metallic systems have been found to exhibit glass forming tendencies. When cooled at cooling rates below certain critical values, the liquids solidify to form a crystalline structure. It is the crystalline form of the solid metal which has been used so far for various applications. When those liquids are rapidly cooled at cooling rates exceeding 10^6K/s, they freeze into a non-crystalline structure called glasses. These glasses consist of clusters of atoms which exhibit SRO - short range order. Cluster models have been observed to exhibit unusual symmetries such as five fold axis of symmetry etc.

The main advantage of metallic glasses is that they can be produced in useful form quite economically. These glasses are strong, tough, corrosion resistant and cost efficient. From a manufacturing point of view, it is estimated that about four to five times less energy is consumed in going from liquid metal to a thin metallic glass strip than would be consumed by conventional metallurgical processing, viz. starting from an ingot to rolling of thin strips with all the intermediate steps.

The fine thickness of the strip (40-70 μm) is a stringent limitation which restricts the industrial applications. Also only a few alloys are easy glass formers, which further restricts the applica-

bility. One promising technique for improving the performance of the bulk material is producing a surface layer of amorphous material. This surface modification treatment can be performed by laser irradiation, thus making the surface tough, strong and corrosion resistant.

Lasers are also used for a number of other industrial applications. In particular, in the case of materials, the high power CO_2 laser developed during the last decade has made the laser heat treatment industrially viable. Moreover in industry, the laser has been continuously implemented as a multiple purpose tool.

Apart from the applications listed above, lasers have been found useful for surface hardening processes. Lasers are especially useful because of their energy efficiency, versatility and precision. The laser heat treated surfaces are less distorted and show negligible stress concentration. Some of the major advantages of laser processing with respect to surface modification by ion implantation are that lasers do not require vacuum and have high productivity and reproducibility.

The application of laser processing to materials has a number of limitations which somehow counterbalance the already mentioned advantages. And hence laser processing has not dominated the field of heat treatment, welding, cladding and surface treatment.

Laser installations involve high initial investment and there is fear of obsolescence because of constant improvement in equipment design. Today's lasers work at about 1% to 2% efficiency i.e. the output power is only 1% or 2% of the input power. Hence, there is a great opportunity for improvement. Available literature and technical data

are not enough to encourage the manufacturers to opt for laser processing on a large scale. There are other minor limitations such as occasional necessity of an absorbing coating to improve laser beam-work piece interaction. Also maximum laser-treated surface thickness is of the order of a few microns which may not be sufficient for certain applications.

A lot of attention has been focussed on iron and its alloys. Because of their applicability as a magnetic material, a lot of research is being carried out to evaluate iron based easy glass formers.

This research is part of a systematic analysis of the effect of laser irradiation of iron alloys with particular emphasis on alloys that are known to be easy glass formers.The effects of laser heating upon the phase transformation in pure iron have been assessed. The possibility of plasma formation and consequent evaporation of a surface layer has been evaluated. Surface damage and incident beam energy have been correlated and the optimum energy for maximum melt depth with least surface damage has been established. Amorphous formation on the surface of an easy glass former alloy has been proven and a technique has been developed in this study to measure the layer thickness by a non-dustructive testing method. Fe-B and Fe-Zr systems have been employed and a correlation has been established between the glass forming tendency and the various other factors such as microstructure, solute solubility, sample weight and the effect of metastable phases present in the structure.

CHAPTER 2

INTERACTION OF LASER WITH METALS

LASER - Light Amplification by Stimulated Emission of Radiation - is a source of intense power which can be used to rapidly heat, melt and eventually vaporise the surface of a metal or an alloy. By scanning a pulsed or a continuous laser beam across a surface, it is possible to produce a thin molten zone that is rapidly cooled by conduction of heat into the adjacent substrate. The more important process during the laser interaction with metals is heat generation.[1] The temperature rise is determined by the laser power, pulse duration, absorption coefficient, specific heat and thermal diffusivity of the material.

The cooling rates obtained in laser irradiation experiments vary in the range of 10^8 to 10^{12} K/s. The mathematical treatment by Greenwald et al.[2] dealing with laser irradiation of metals shows that the time of heating and cooling of the irradiated surface is nearly the same. Figure 1 shows the variation of temperature with time at selected melt depths.

2.1 Coupling of Laser Beam Energy with Metals

The interaction of laser radiation with condensed matter, i.e. the process of energy deposition in such interactions, has been explained using certain fundamental mechanisms. The major interaction is through the excitation of valence and conduction electrons by the photons in the energy range of laser light i.e. from infrared to ultraviolet wavelengths. These properties are generally referred to as

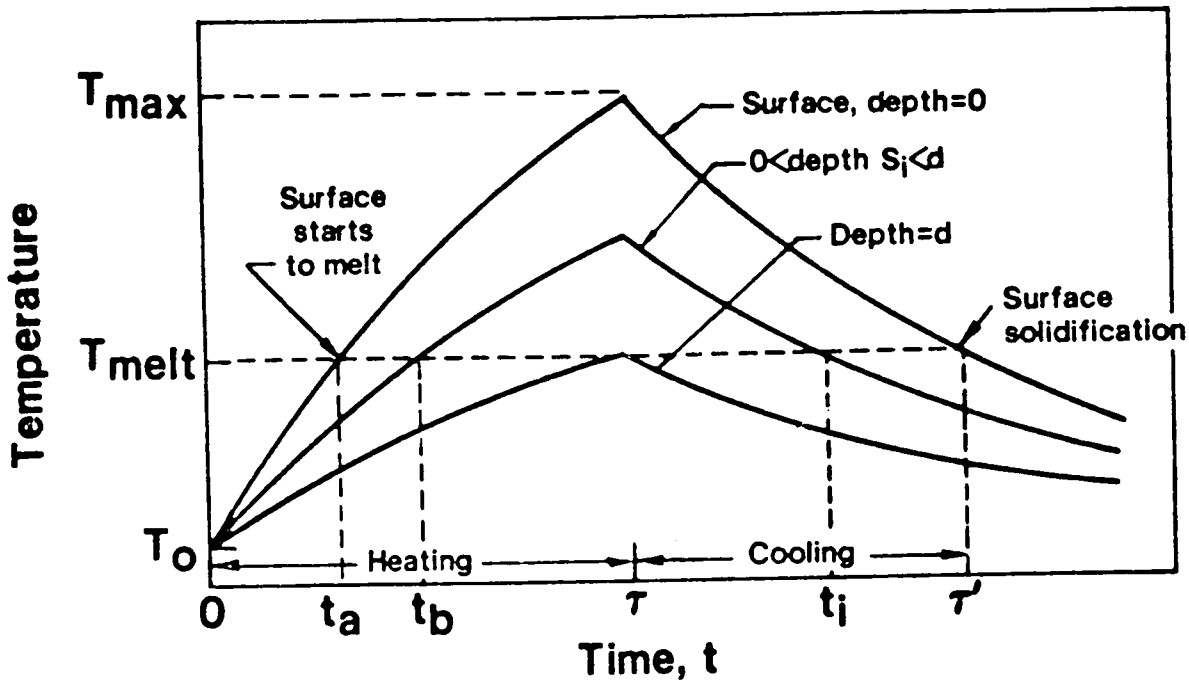


Fig. 1 - Variation of temperature with time at selected melt depths.

Source: L.E.Greenwald, E.M.Breinan and B.H.Kear, "Laser-Solid Interactions and Laser Processing -1978" Materials Research Society Publication edited by S.D.Ferris, H.J.Leamy and J.M.Poate, (1979), 189

'optical properties' because of the long wavelengths that are in the range of visible light.

In metals, the energy is mostly absorbed by the conduction electrons because of their high free electron density and hence the penetration of electromagnetic waves is much less than in non-metallic materials. Free electrons accelerate as a result of energy absorption from the field, but because the external field is periodically changing, the electrons re-radiate their kinetic energy which is the cause of reflection. Thus in order to transfer energy to the lattice, the excited electrons must collide with the atoms of the crystal. The relaxation time of the energy transfer is about 10^{-12} s.

The response of matter to light can be adequately described in terms of two macroscopic quantities, the real and the complex components of the refractive index $\langle n \rangle$ given as[3]

$$\langle n \rangle = n + ik$$

where n is the ratio of the phase velocities in vacuum and in the material and k describes the damping of light waves across the material. Also the reflectivity R and the absorption coefficient α can be used for describing the degree of coupling, and are related to the refractive index by

$$R = \frac{(n-1)^2 + k^2}{(n+1)^2 + k^2}$$

$$\alpha = \frac{4\pi k}{\lambda}$$

The change of power density as the laser light travels through the material can be written as

$$dI = - \alpha(x) I dx$$

where x is the penetration depth and the absorption coefficient α can change because of thermal gradients and phase changes. Integrating the equation, we get

$$I(x) = I_o \exp[-\int_o^x \alpha(x')dx']$$

where I_o is the laser power density that penetrates the first layer of the material.

The value of α for metals is of the order of 1×10^6 cm^{-1} which makes the intensity decrease to e^{-1} after 10nm. The absorption coefficient in metals tends to remain nearly constant in the range of wavelengths of interest as opposed to the case of semiconductors. On the other hand, the reflectivity of metals is related to the plasma frequency of the electron gas and is high for frequencies lower than the plasma frequency. This frequency is characteristic of each material and the reflectivity then strongly decreases above this characteristic value. Figure 2 shows the normal spectral reflectance of iron for a number of different surface conditions[4]. The reflectivity is seen to decrease steeply for a wavelength of 330nm. Clearly, the use of a laser with a wavelength shorter than this critical value will increase the coupling efficiency. In general, the reflectivity of a surface is strongly associated with its condition and temperature as will be discussed in the following section.

In the case of metals, the surface layer δ where heat is produced is much thinner than the thickness of the layer melted by the laser

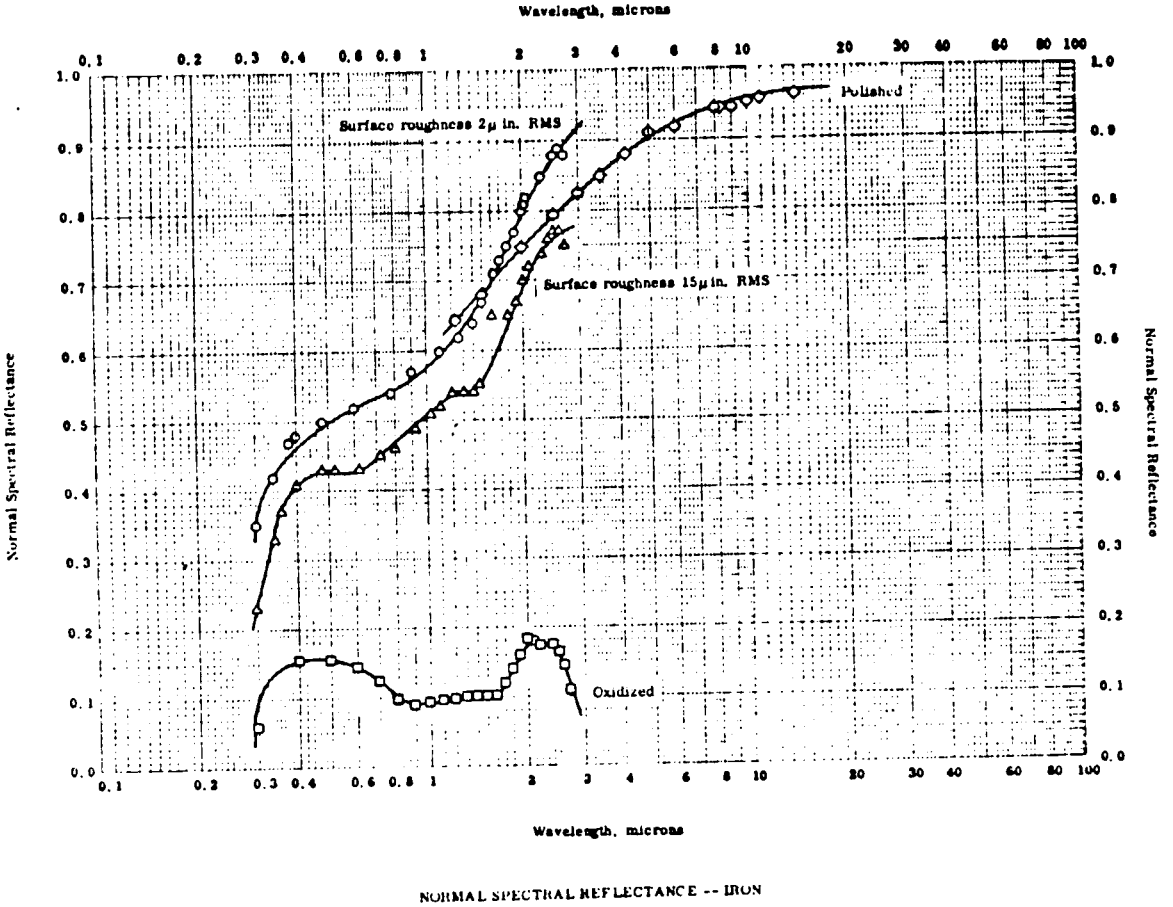


Fig. 2 - Normal spectral reflectance of Iron.
Source: "Thermophysical Properties of High Temperature Solid Materials (TPRC)" Vol. I, The McMillan Company, New York (1967), 602

beam. As an approximation, the laser power density as a function of depth and time can be written as

$$I(x,t) = I_o(t)(1-R)\ e^{-\alpha x}$$

where $I_o(t)$ is the power density output of the laser, and R and α are the average values of reflectivity and absorption coefficient, respectively, in the surface layer δ. The power density absorbed by a layer of thickness x is then

$$I(x,t) = I_o(t)(1-R)[1-e^{-\alpha x}]$$

This electromagnetic energy is readily transformed into heat. Using a random walk approximation, the average heat diffusion distance can be estimated as

$$\Delta = \sqrt{2D\tau_\ell}$$

For iron, the thermal diffusivity $D \simeq 6\times10^{-2}$ cm^2/s and setting τ_ℓ as the pulse duration(49ns), we get

$$\Delta \simeq 7.5\times10^{-5} \text{ cm}$$

Comparing this value with that of δ

$$\delta \simeq \alpha^{-1} \simeq 10^{-6} \text{ cm}$$

shows that we may assume $\delta << \Delta$. This implies that we have practically a surface heat source. This treatment has been extensively explained by M.von Allmen[5] and he points out that this limit represents a critical condition for laser irradiation because small fluctations in the beam power density may produce large temperature variations in the layer. In metals, the liquid has a lower surface reflectivity than the solid. Thus surface absorbs more energy when it becomes liquid during laser processing. This phenomenon is known as 'thermal runaway'. The damage threshold energy is usually slightly more than the melting thereshold

energy. Therefore thermal runaway results in either narrowing of the window for damage-free melting or going over the damage threshold energy. In either case, surface damage control becomes difficult.

2.2 Concept of Laser Heating and Cooling

Laser irradiation of metals involves heat absorption and subsequent dissipation primarily by conduction into the solid and only secondarily by convection and radiation from the surface. Depending on the input energy, the metal surface may undergo three phase changes viz. solid-solid, solid-liquid and liquid-vapor. However, because of the large ratio between the diameter of the melted region and the melted depth ($\sim 3 \times 10^3$), the problem of melting followed by solidification may be treated as a one-dimensional problem. The relation used has already been given viz.,

$$I(x,t) = I_o(t)(1-R)e^{-\alpha x}$$

Numerical techniques have been used to determine the solidification characteristics of the melted region, depth of the melted zone etc. Mehrabian et al[6] have shown that the melt depth reaches a certain maximum for a fixed time of irradiation (Figure 3) irrespective of the energy input. Hsu et al[7] used a finite difference explicit method for calculating the temperature profile vs. time, the interface velocities during melting and solidification and the corresponding heating and cooling rates in the surface layer.

Numerical techniques are applied because there is no exact solution for this problem. In general very few cases of melting and solidification can be solved analytically; moreover a number of com-

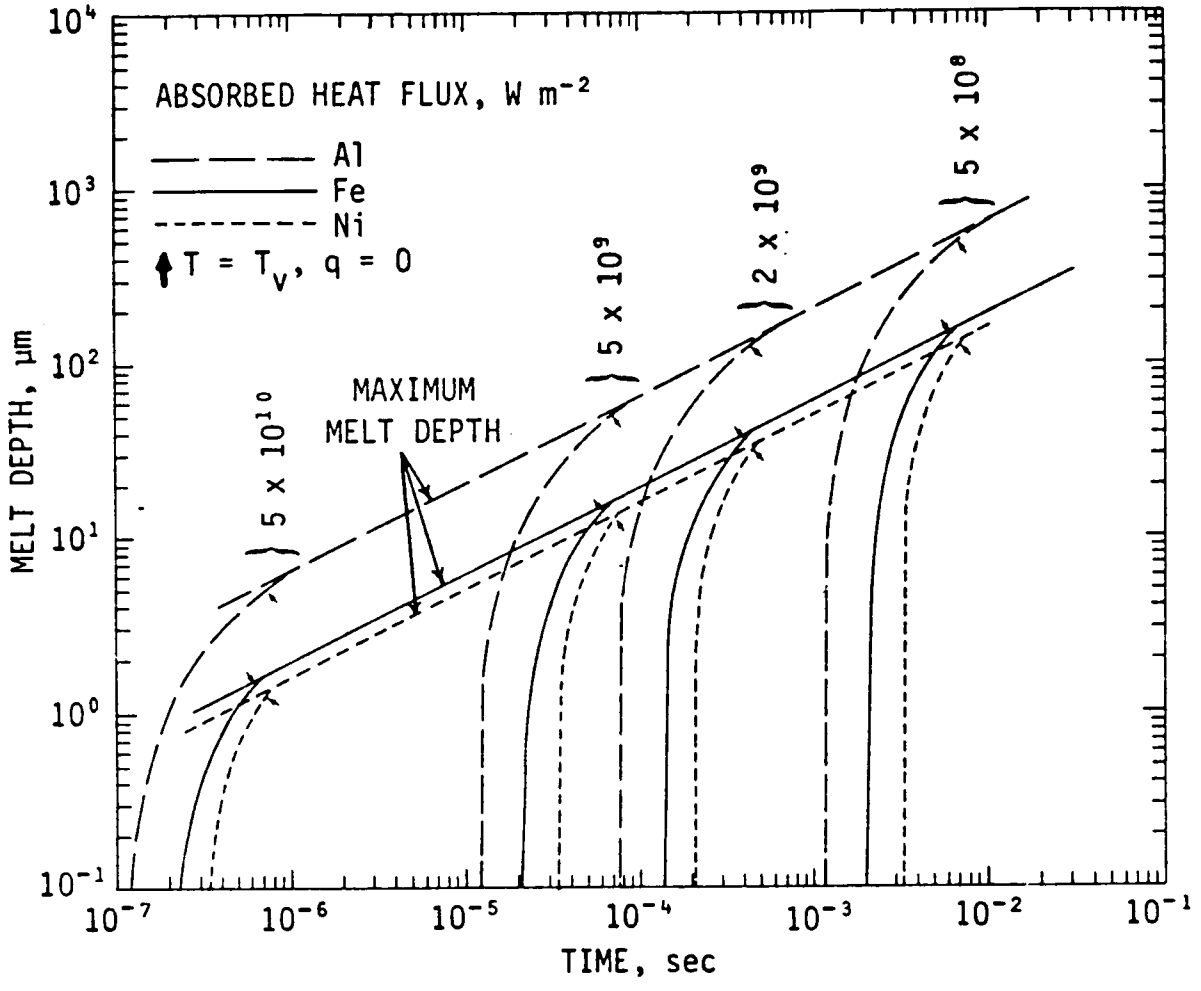


Fig. 3 - Melt depth versus total time for different uniform absorbed heat fluxes obtained via a numerical technique. Arrows indicate times at which a surface reaches its vaporization temperature and heat flux is removed.

Source: R.Mehrabian, S.Kou, S.C.Hsu and A.Munitz,"Laser-Solid Interactions and Laser Processing -1978" Materials Research Society Publication edited by S.D.Ferris, H.J.Leamy and J.M.Poate, (1978), 129

plications are intrinsic of these kind of problems. First of all, the laser pulse is not uniform in intensity and there are spatial and temporal fluctuations in intensity[1]. Although the temporal fluctations may be unimportant for a given pulse, the spatial fluctuations may lead to intensity minima and maxima resulting from interference with the reflected portion of the wavefront. This may result in nonuniform heating in the laser irradiated zone.

Another complication is that the absorption and the reflection coefficients are dependent on the radiation wavelength and surface temperature . For example, in metals, for a fixed wavelength, the reflection coefficient decreases as the temperature increases with a sudden decrease at the melting point. This results in thermal instability as explained before. In the case of silicon, however, the reflectivity increases with temperature.

However, analytical techniques have been successfully used by making certain assumptions. Laser pulse is regarded as a square wave of duration t_p and of uniform intensity I. Considering normal incidence of the pulse on a material with absorption coefficient α, surface reflection coefficient R (both assumed to be independent of temperature), specific heat per unit mass C_v, density ρ and thermal conductivity K, we can determine the characteristic length to which the temperature profile is spread out. This length is given by

$$L = \sqrt{2Dt_p}$$

where D, the diffusivity of the material, is given by

$$D = K / C_v\rho$$

An approximate heating rate can be determined by assuming that the optical absorption depth $1/\alpha$ is small compared to the diffusion length.

In other words, if

$$\alpha\sqrt{2Dt_p} >> 1, \text{ then}$$

the energy absorbed during the laser pulse $(1-R)It_p$ is used to heat a layer of thickness L. The average temperature may be determined to be

$$\Delta T \simeq (1-R)It_p \; / \; C_v \; \rho(2Dt_p)^{\frac{1}{2}}$$

Assuming heating and cooling time to be the same i.e. equal to t_p, we see that the heating or cooling rate can be calculated as

$$\Delta T/t_p = (1-R)I \; / \; C_v \; \rho \; (2Dt_p)^{\frac{1}{2}}$$

The analytical treatment is approximate in nature and serves only as a guideline. As stated earlier, M. von Allmen[5] has analysed this problem emphasizing the aspect of energy deposition based on the detailed electronic structure of the material which in turn is modified as a result of irradiation.

2.3 Dislocation Generation by Laser Irradiation

Nickel single crystals melted with Q-switched Nd-YAG laser radiation exhibit a dislocation microstructure which strongly depends upon the surface orientation. The <100> crystals develop a dislocation cell structure with a dislocation density of 10^{11} to $10^{12} cm^{-2}$. The <111> crystals contain a laterally uniform dislocation network resulting in a much higher dislocation density than for the <100> surface.[8]

The dependence of the dislocation microstructure upon the surface orientation is not yet fully understood, but it may be associated with

the fact that <111> planes are the slip planes in the FCC crystal structure. The same effect has been observed in pulsed laser melting of <111> and <110> Mo crystals cut from the same boule.[9] In this case the <110> crystal has a much higher dislocation density than the <111> crystal. It should be noted that the main slip plane in BCC Mo is the <110>.

The presence of dislocations in the melted region can be explained by three different mechanisms viz. one in which dislocations are created by extremely high thermal stresses caused by steep thermal gradients, other in which dislocations grow epitaxially from the existing ones in the underlying solid layer and a third mechanism according to which the dislocations are formed by condensation of vacancies.[10] The first mechanism does not require the surface to be melted in order to generate dislocations as long as high thermal gradients are present. It is still not quite known which of the above mechanisms is dominant in the case of laser irradiation experiments. Bolling and Fainstein[11] have given an excellent treatment of the phenomenon of formation of dislocations from condensed vacancies on the assumption that excess concentration of vacancies are trapped in the solid by rapid freezing which seems to be a generally accepted view.

Another source of dislocations is the exposure to the shockwave coming from the laser. Fairand and Clauer have reported that exposure to the shockwave generated by a laser pulse increased the strength and the hardness of an aluminum alloy by about 10-30%. The transmission micrographs of shocked samples showed a marked increase in the dislocation density as compared to those which had not been exposed to a

shockwave.[12] But this mechanism can only be operative if the surface is not melted.

2.4 Surface Damage

High energy laser irradiation of a surface shows signs of surface damage in the form of craters, ripples and unevenly wavy surfaces. The craters may be caused by the non-uniform intensity distribution across the cross-section area of the pulsed laser beam. Laser pulses are not uniform in intensity but show spatial and temporal fluctuations in intensity[1]. Lowndes[13] has actually measured the intensity distribution through the cross-section of the laser beam and found a considerable amount of variation in intensity for the KrF laser. The measurements were done using a 0.5mm diameter pinhole which was scanned in two directions. The intensity distribution had a plateau of 20mm width in one direction and had a gaussian distribution with a 3mm width at 90% of peak intensity value in the other direction.

The ripples observed on the surface may have been caused by convection currents in pulsed laser formed melts as reported by Possin et al.[14] They present a theoretical treatment of the phenomenon of surface ripples making use of the approximate solution of the Navier-Stokes equation to determine mass transport. Anthony and Cline[15] attribute the presence of surface ripples to the surface tension gradients which sweep the liquid away from beam impact point. These surface tension gradients are generated by the temperature gradients and curvature on the melt surface. The authors, however, concede that if the residence time of the beam is less than a certain critical value,

the liquid does not have sufficient time to form ripples and thus rippling from surface tension gradients is avoided.

A general observation is that as the input energy of the laser beam to the workpiece increases, the surface irregularities in the form of craters and ripples also increase.

Some preliminary work has shown that when the laser beam is masked before its incidence on the metallic surface, it forms a rim along the mask edge. Interference effects have also been observed in some samples, especially those irradiated with a high beam energy. The presence of the rim is almost uniform, probably due to the interference effect giving an intensity concentration as high as 4 times the original intensity at the mask edge.

CHAPTER 3

METALLIC GLASSES

Metallic glasses have recently become a focus of interest because they can be commercially produced by such techniques as melt-spinning for making ribbons and free jet spinning for wire making. Klements, Willens and Duwez[16] in 1960 reported for the first time that an Au-Si alloy is rendered amorphous when rapidly quenched from the liquid state to -196°C. The amorphous structure obtained from the melt is called a 'Glass' to differentiate it from the amorphous structure obtained by other procedures. In that sense amorphous solids have been produced by vapor and electro-deposition methods since 1930. Since the year 1960, a large number of different alloys have been produced as metallic glasses. Alloy systems such as Au-Si, Pd-Si, Pt-Sb, Cu-Zr were found to exhibit metallic glass formation in a certain range of alloy composition. As techniques were developed to make continuous strips of metallic glass, the alloys of commercial importance were studied and rapid progress was done in the understanding of iron and its alloys.

3.1 What are Metallic Glasses?

Glasses are differentiated from liquids by their high resistance to shear deformation. They differ from crystalline solids in that they lack the atomic periodicity present in crystalline solids. Therefore, the structural characteristics of a glass cannot be uniquely determined directly as in the case of crystalline solids. A few structural models

have been suggested as given below, to account for experimental scattering data obtained for various glasses.

One model assumes that Glasses are micro-crystals of size ~ 1nm which are randomly oriented[17,18]. Another model supports the assumption of highly ordered regions but suggests that these micro-crystals contain symmetry elements which cannot be the basis of an extended three-dimensional lattice[19] e.g. five fold axis of rotation. A third model assumes the glass structure to be a statistical, densely packed configuration of hard spheres known as 'Continuous Random Model'[20,21]. Computer models have been developed by Bennet[22], Adams and Matheson[23], and Sadoc et al.[24]

3.2 Techniques for Glass Formation

Various techniques have been developed for glass formation from the liquid metal. The most important feature of all these techniques is the ability of attaining very high cooling rates. These cooling rates, depending upon the technique, vary in the range from 10^5 to 10^{12}K/s and are necessary for obtaining amorphous metals. In this sense, the cooling medium should posses a sufficiently high heat transfer coefficient and the glass films should be thin enough to facilitate fast heat removal.

An interesting feature to note is that there are other controlling factors associated with the alloy system rather than the process involved. It is observed that, with the same cooling rates, glass is produced in some alloy systems whereas it is not in others. The suppression of crystalline phase formation may be attributed to either

the suppression of nucleation itself or in the presence of nucleii, to the inhibition of interface advance.[10]

The first synthesis of a glass from the liquid metal was done by the 'Gun Technique'[16] in which a metal substrate was used as a quenching medium. In that way, foils could be formed as thin as 100nm, but of non-uniform thickness. The thin foils could be directly used for TEM analysis. The process was restricted in application because of its inability to reproduce the results.

The 'Hammer and Anvil' process is another discontinuous process where a liquid drop is squeezed between a pair of hammer and anvil at a very high speed, thus quenching the drop between two metallic substrates. Kroeger et al[26] have given a detailed assessment of the effect of hammer speed, sample size and initial melt temperature on the cooling rate and efficiency of glass formation from predicted cooling curves assuming Newtonian cooling. Recent versions employ an arc for melting the alloy on a watercooled substrate, thus avoiding crucible problems and making possible the quenching of alloys with melting point up to 2000°C and above.[27] Figure 4 shows a prototype of this 'Hammer and Anvil' or Splat Quenching technique. Other techniques include the 'Twin Roll' technique[28] for continuous production of glass foils, 'Melt Spinning' used commercially, 'Melt Extraction'[29] and 'Pendant Drop Process'.[30] Kavesh[31] has recently reviewed the fabrication procedures of amorphous metals.

There is another category of these processes where a high power laser is used to melt a thin layer of the surface of the sample. After removal of the beam from the melted region, the liquid is quenched by

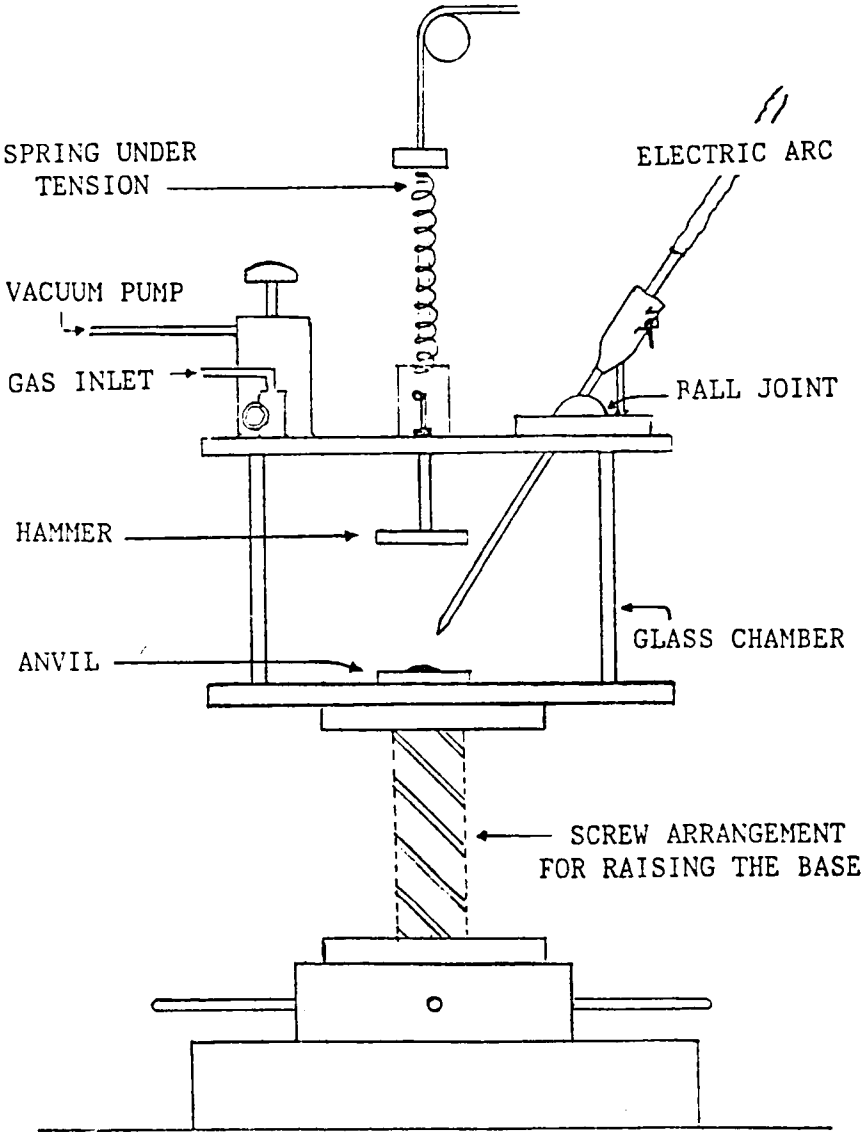


Fig. 4 - Apparatus for splat quenching technique.

the solid material beneath it. The cooling rates attained may be as high as 10^{10} to 10^{12}K/s. Various lasers such as CO_2 laser, Q-Switched Ruby laser, Nd-YAG laser, Excimer laser and picosecond laser have been used for irradiation experiments and a wide spectrum of results has been obtained as a function of different cooling rates attained by the use of different lasers.

3.3 Glass Forming Alloy Systems

Ideally, every liquid would form glass upon cooling if crystallization into one or more phases is avoided[32], i.e. if the cooling rate is high enough to inhibit the processes at the crystal-liquid interface. It should be stressed here that though in principle, glass can be obtained from pure metals, the velocity of quenching may not be attainable. There are a fairly large number of metallic alloys that form glasses under cooling rates compatible with experimental conditions e.g. 10^5 to 10^{10}K/s. A list of glass forming compositions has been presented by Takayama[33] and a periodic table representation of glass forming elements has been published by Masumoto and Maddin.[34]

Polk and Giessen[35] have categorised glass forming systems as 'Major Systems' consisting of two types. One system combines a late transition (or noble) metal and a metalloid e.g. Pd-Si, Ni-P-B, Fe-P-C etc.; the other system combines an early transition and a late transition metal (or Cu) e.g. Ti-Ni, Nb-Ni, Zr-Cu etc.. These authors also refer to 'Miscellaneous Systems' such as Mg-Zn, U-V, (Ti-Zr)-Be etc. and 'Thermally Stable Systems' such as Co-Gd(-Mo) which are formed by sputtering.

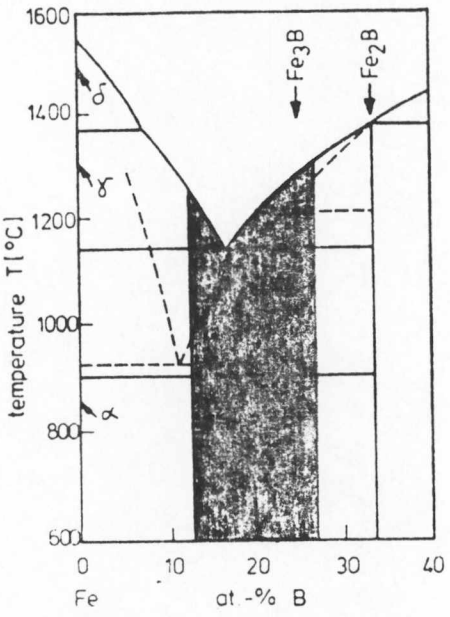
Ease of glass formation is associated with a number of factors. Substantial size difference between alloy component atoms helps in glass formation. It is suggested that, in the case of metal-metalloid glasses[36], the size difference makes a random packed structure possible to have higher packing density than that possible for dense random packing of spheres of one size. These high density structures are relatively stable to the fluctuations necessary for crystallisation to take place.

Phase diagrams give an important clue for ease of glass formation. Systems with a narrow low melting temperature region (single deep eutectic) exhibit relatively high glass forming tendency.[32,37] Figure 5 shows some glass forming system phase diagrams. In the case of the Fe-B phase diagram, for instance, the shaded region is normally accepted as the glass forming composition range. Recent studies have indicated, however, that the conventional glass forming range may be exceeded by using a pico-second laser for irradiation. Lin[38] has reported glass formation in the Fe-B system for a boron content of as low as 5 at% B.

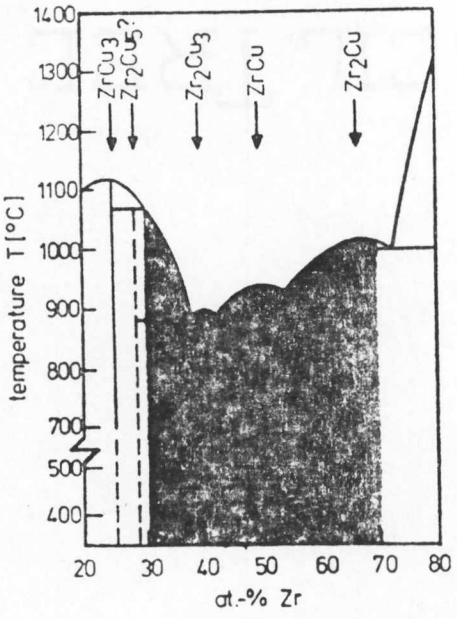
Some of the other factors which influence the glass forming tendency in different alloy systems are valence difference, electronegativity difference, stoichiometry and compositional ordering etc.

3.4 Kinetics of Glass Formation

Glass is considered to be a solid formed by the continuous hardening of the cooled liquid. It is distinguished from a solid formed



α-Fe	bcc	a = 0.287nm
γ-Fe	fcc	a = 0.359nm
Fe_3B	tetragonal Ti_3P type	a = 0.864nm c = 0.428nm
Fe_3B	orthorhombic Fe_3C type	a = 0.543nm b = 0.666nm c = 0.445nm
Fe_2B	tetragonal $CuAl_2$ type	a = 0.511nm c = 0.425nm



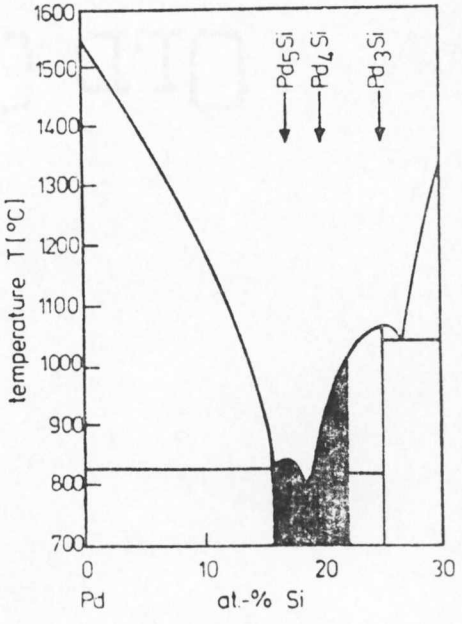


Fig. 5 - a) Fe-B system, b) Crystal structure of stable and metastable phases in iron rich Fe-B alloys, c) Cu-Zr system, d) Pd-Si system, Shaded portion in a), c) and d) indicate glass forming range.

Source: 'Glassy Metals I' edited by H.J.Guntherodt and H.Beck, Springer-Verlag, Vol.46, (1981)

by nucleation and growth where solidification occurs by the motion of the liquid-solid interface. The term 'hardening' implies increasing resistance to shear forces causing the body to flow and permanently change its shape. A quantitative measure of glass forming ability is done in terms of the kinetics of crystallization. One such quantitative measure is the glass transition temperature , T_g. T_g is the temperature at which the atomic mobility is high enough as to allow for diffusive atomic rearrangement to occur in a matter of minutes.

Turnbull[39] has considered the process of nucleation of small crystallites. He assumed that the crystallites have the same composition as the liquid, the nucleation transients are unimportant and the bulk free enthalpy change associated with the transformation of the undercooled liquid to the crystal phase, ΔG_v, is given by the linear approximation $\Delta G_v = \Delta H_f \Delta T_r$ where ΔH_f is the molar enthalpy of fusion and ΔT_r, the reduced undercooling $(T_\ell - T)/T_\ell$. With these assumptions, he showed that the homogeneous nucleation frequency I_v is given by

$$I_v = \frac{k_n}{\eta(T)} \exp\left[\frac{-b\alpha^3\beta}{T_r \Delta T_r^2}\right]$$

where k_n is a kinetic constant, $\eta(T)$ is the shear viscosity at temperature T, b is the nucleus shape constant, T_r is the reduced temperature T/T_ℓ and α and β are dimensionless parameters defined as

$$\alpha = \frac{(NV^2)^{1/3}\sigma}{\Delta H_f}$$

$$\beta = \frac{\Delta S_f}{R}$$

where N is Avogadro's number, V is the molar volume of the crystal, σ is the liquid-crystal interfacial energy and ΔS_f is the molar entropy of fusion. It can be easily observed that the main resistance to nucleation comes from α which is proportional to the liquid-crystal interfacial energy σ. Physically α is the number of monolayers/area of crystal which would be melted at T_ℓ by an enthalpy ΔH equivalent in magnitude to σ.

In metals, $\alpha\beta^{1/3} \simeq 0.5$ which is consistent with their high resistance to homogeneous nucleation up to a large undercooling ΔT_r of about 0.2.[40] Figure 6 shows the upper limiting nucleation frequency vs. reduced undercooling with different values of $\alpha\beta^{1/3}$. The graph shows that I_v rises steeply with ΔT_r, though the value is quite neglible at small undercoolings. With further increase in ΔT_r, I_v increases to a broadly peaked maximum at $T_r = 1/3$, then falls to zero at 0°K. The curves also indicate that liquids with $\alpha\beta^{1/3} > 0.9$ would not crystallize at practically any undercooling by homogeneous nucleation, whereas for $\alpha\beta^{1/3} < 0.25$, it is almost impossible to suppress crystallization even at 0°K.

A related kinetic approach by Uhlmann[41] for a number of non-metallic glass formers, where only a limited amount of crystal growth was taken into account, was adopted by Davies et al[42] for some selected metallic glass formers. The Johnson-Mehl-Avrami treatment of transformation kinetics yields

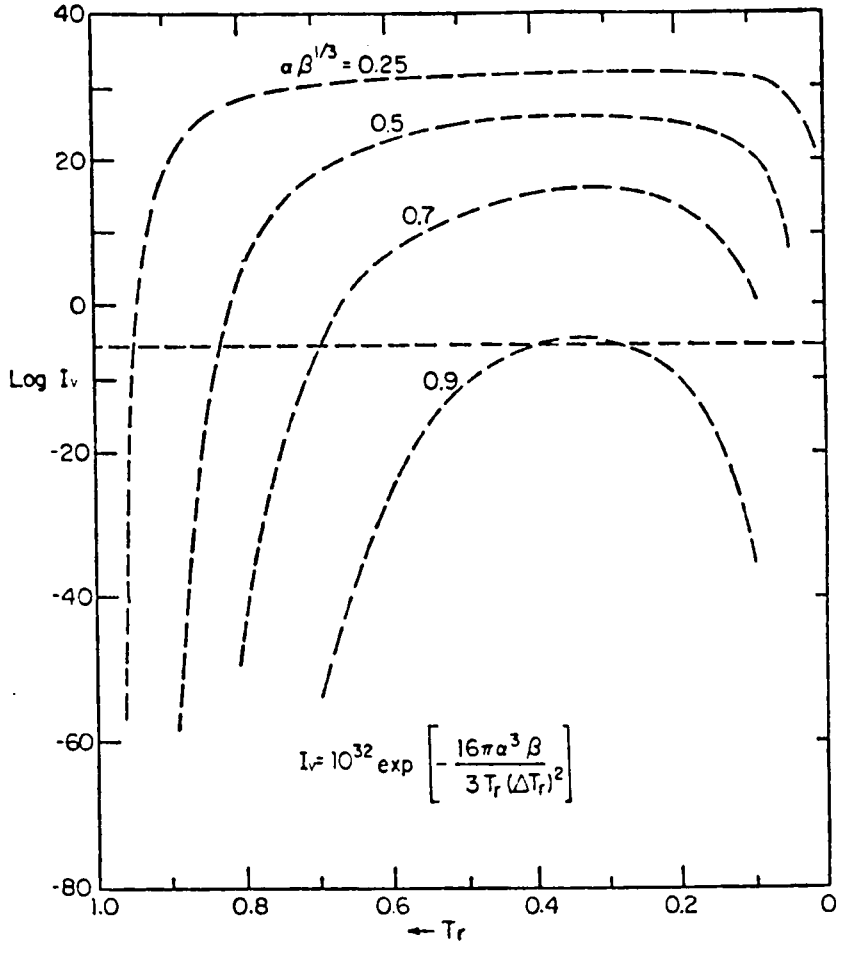


Fig. 6 - Calculated variation of the logarithm of the frequency (in $cm^{-3}s^{-1}$) of homogeneous nucleation of crystals in an undercooled liquid with reduced temperature for various assignments of $\alpha\beta^{1/3}$.

Source: D.Turnbull, Contemp. Phys., 10, (1969), 473

$$x = 1 - \exp(-\pi I_v U_c^3 T^{4/3})$$

where x is the fraction of transformed phase in time t and U_c is the crystal growth velocity. For small x, the equation reduces to

$$x \simeq \pi I_v U_c^3 T^{4/3}$$

Substituting for U_c and I_v in the above equation, we get an expression for time t required to achieve an x fraction of crystal, given by

$$t \simeq K \left\{ \frac{x \exp\left(\frac{1.024}{T_r^3 \Delta T_r^2}\right)}{\left[1-\exp\left(\frac{-\Delta H_f \Delta T_r}{RT}\right)\right]^3} \right\}^{1/4}$$

where K depends on η-the viscosity, a_o-the atomic radius, k-Boltzman's constant, T-temperature, N_v-the average volume concentration of atoms and f-the fraction of sites where atomic attachment can occur.

A Time-Temperature-Transformation curve may be constructed by using the above equation. The time t is expressed as a function of T_r to transform to a barely detectable fraction of crystals which is arbitrarily chosen to be 10^{-6}. Computed curves for some metallic systems are shown in Figure 7. The form of the T-T-T curves and the magnitude of the time at the nose is largely a reflection of the competition between the increasing driving force for nucleation and decreasing

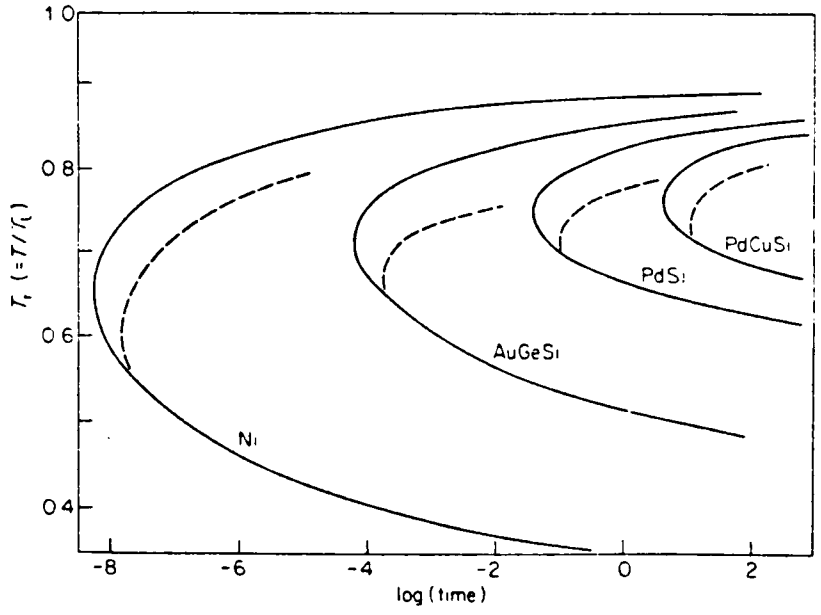


Fig. 7 - Time-Temperature-Transformation curves (solid lines) and the corresponding Continuous-Cooling-Transformation curves (dashed lines) for the indicated systems.

Source: 'Metallic Glass Formation' by H.A.Davies, Amorphous Metallic Alloys edited by F.E.Luborsky, BMM, (1983), 18

atomic mobility, a result of increasing η, with decreasing T_r. Large reduction in T_ℓ along with a slight increase in Tg - the glass forming temperature, as a result of alloying, substantially retard the process of crystallization in alloys as compared to pure metals.

In the entire treatment of glass formation kinetics so far, it was assumed that the crystallization process is partitionless i.e. the crystals have the compostion of the melt. But this may not be the case especially in systems which exhibit a steep depression of the liquidus. Hence the theoretical treatment of glass forming kinetics needs certain modifications to account for the additional diffusion involved in partitioning, particularly for more readily glass forming systems. Nevertheless, the validity of the kinetic approach may be established by the fact that broad agreement exists between experimental observations and theoretical results.

CHAPTER 4

IRON AND ITS ALLOY SYSTEMS

4.1 Pure Iron

Amorphous pure iron has been formed by the low temperature condensation process by several investigators.[43-47] Low temperature condensation means the condensation of a metal vapor onto a substrate cooled by liquid nitrogen or liquid helium. Fujime[43] has reported that the amorphous iron films prepared at 4.2°K undergo crystallization within several seconds at temperatures near 180°K. This temperature is about a tenth of the melting point of iron. A similar relation was observed in the case of chromium too. Mikhailov et al[46] have reported a superconducting state of an iron film prepared on a substrate cooled by liquid helium. Lazarev et al[47] have observed that at about 40°K, a sudden irreversible change of electrical resistance occurs in iron films prepared by a similar technique. They could not, however, find a superconducting state of iron films in contrast with the work of Mikhailov et al. Bennet and Wright[48] and Felsch[49] have reported that for pure iron and iron with impurities up to 2%, the films, which are highly disordered but crystalline, show no sudden drop in resistance as reported by Lazarev et al and exhibit no superconductivity as observed by Mikhailov et al.

There is no evidence of glass formation of pure iron either by splat quenching technique or by laser irradiation process. Splat quenched pure iron forms ferrite and martensite, with the tendency of

martensite formation and the amount of martensite increasing with residual carbon content.[50]

4.2 Iron Base Alloy Systems

Fe-Si and Fe-Ge amorphous alloys have been prepared by the vapor quenching technique.[51-56]

Thin films of amorphous Fe_x-C_{1-x} [$0.75 < x < 0.50$] have been prepared by the sputter deposition technique.[57] An interesting point to note is that in the case of carbon sputtering, the percent of carbon deposition is a function of Argon pressure with the nominal composition of the target attained at very low (P_{Ar}<5μm) Argon pressures. This effect seems to be confined to carbon containing alloys only. There is no mention of glass formation of Fe-C alloys by either splat quenching or by laser irradiation. However, amorphous quasibinary alloys of composition $[Fe_{1-x}\text{-}Mn_x]_{.75}\text{-}P_{.15}\text{-}C_{.10}$ with $0.0 < x < 1.0$ were synthesized by splat quenching for their magnetic behaviour characterization.[58]

Fe-B is one of the most widely investigated metallic glass systems which forms a glass at relatively moderate cooling rates, at about 15 to 20at% boron. The deep eutectic found between 18 and 19at% boron favors glass formation, even though glass has been formed at as low a boron content as 5at% using a pico-second laser.[38] Glasses in the range of 17 to 20at% boron have been intensively studied[59-61] and constitute a model system for metal-metalloid glasses. The eutectic temperature of interest is 1161°C. Hypo-eutectic compositions form primary γ whereas hyper-eutectic compositions form primary Fe_2B under equilibrium

conditions of cooling. The α phase starts to form at 910°C on further cooling.

Iron-Boron glasses have been found to possess exceptional mechanical properties such as high strength and high compressive or bending ductility. $Fe_{80}B_{20}$ has an ultimate tensile strength of $0.36MN/cm^2$, one of the the highest reported for a binary metallic glass.[62] The modulus of elasticity of $Fe_{80}B_{20}$ glasses ($16.9MN/cm^2$) compares quite well with that of plain carbon steels ($20.5MN/cm^2$) exhibiting a similar stiffness as plain carbon steels. Hardness is an effective measure of intrinsic strength of the material. In Fe-dominated glassy alloys, Naka et al[63] have established a relatively good correlation between microhardness and average electron concentration per metal atom. The authors attribute the strength of metallic glasses to the bonding between the transition metal and the metalloid and conclude that this bonding is diminished by alloy additions which result in an increased d-electron concentration. It is known that the electron transfer from metalloid to transition metal is less for B than that for P.[64] Hence the $Fe_{80}B_{20}$ glass is much stronger ($H=1100Kg/mm^2$) than the $Fe_{20}P_{16}C_3B_1$ ($H=835Kg/mm^2$) glass.

In general, the microhardness increases with B content. Additions of a second metalloid in $Fe_{80}B_{20-x}N_x$ glasses (N stands for a metalloid (P,Si,Ge,C) other than B) result in a drop in hardness, thus further confirming the contribution of B towards hardness increase. However, with the exception of P, substituting up to 3% of the other metalloid for B raises the crystallization and embrittlement temperatures.[61]

Three distinct crystallization modes occur in the Fe-B glasses. Primary crystallization of α-iron in the alloys with a B content up to 16at%, eutectic crystallization into (non-equilibrium) α-iron and a tetragonal Fe_3B phase for compositions between 16 and 24at% and polymorphous crystallization into Fe_3B beyond 25 upto 26at% B. At higher B contents eutectic crystallization into stable phases α-iron and Fe_2B is obtained.[65]

Fe-Zr alloys are known to be ready glass formers near the eutectic composition of Fe-10at%Zr, Fe-67at%Zr and Fe-75at%Zr, in all cases towards the Zr rich side.[66,67] But the iron-rich glasses have gained more importance because of their application as magnetic materials.

In general, the Fe-Zr alloys have slightly inferior hardness and strength values compared to those of Fe-B or Fe-P alloys. But the crystallization temperature is higher, implying a better thermal stability. Typical values of hardness for Fe-Zr alloys are in the range of 630-660 VPN, fracture strength of around 2100 MPa and crystallization temperature of about 500°C.[68]

Recently iron based amorphous alloy formation was reported by the process of solid state reaction.[69] Layers of elemental iron and zirconium were deposited onto oxidized silicon wafers by electron beam evaporation. The average composition was $Fe_{61}Zr_{39}$ and the compositional wavelength was 22nm. The alloy amorphized when it was annealed at 623 K for 2 hours, which was confirmed by X-ray diffraction technique.

The combination of zirconium and boron as glass forming elements is extremely effective both in expanding the formation range and incresing stability against crystallization for Fe-based amorphous

alloys.[70] Figure 8 shows a part of the Fe-B-Zr ternary diagram where the crystallization temperature is plotted as a function of composition of the amorphous alloy. Fe-B-Zr alloys seem to show a lot of potential towards the development of Fe based glasses which could be produced on a commercial basis possessing high crystallization temperatures and good magnetic properties.

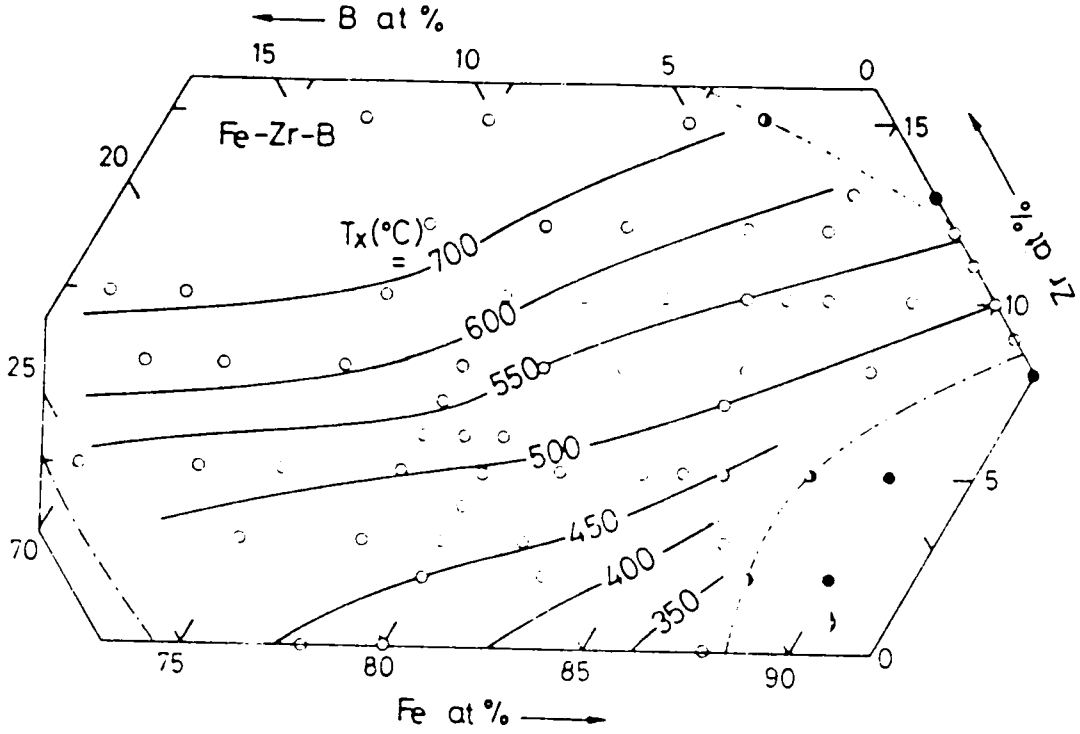


Fig. 8 - Amorphous phase formation in Fe-Zr-B system and composition dependence of crystallization temperature.
Source: S.Ohnuma, M.Nose and K.Shirakawa, Sci. Rep. Res. Insts. Tohoku Univ., 29A, (1981), 254

CHAPTER 5

SAMPLE PREPARATION AND EXPERIMENTAL PROCEDURE

Pure iron, Fe-B and Fe-Zr systems were investigated in this research. Different sample preparation techniques were used for different alloys depending on the form of the starting material available. Various analytical techniques used are described below.

Pure iron samples, with chemical analysis given in Table 1, were cut with an abrasive cut-off wheel to the required size, mechanically polished and subsequently electropolished with a solution of Glacial Acetic acid (90ml) and Perchloric acid (10ml) at 5°C. The polishing was carried out in an interrupted manner at 30V. A horse shoe magnet used as a magnetic holder for electropolishing greatly simplified sample manipulation.

Excimer laser irradiation experiments were carried out at the Oak Ridge National Laboratory (ORNL) Solid State Division in collaboration with Dr. Lowndes. Two types of pulsed lasers were used, a Krypton Fluoride excimer laser with a wavelength of 249 nm and a full width half maximum (FWHM) pulse duration of 46 ns and a Xenon Chloride excimer laser with a wavelength of 308 nm and a FWHM pulse duration of 41 ns. Both lasers were equipped with a calorimeter to measure the input energy density of up to 4.5J/cm^2. As shown schematically in Figure 9, the optical system can be adjusted to give various energy outputs. The beam energy density was measured by inserting the calorimeter between the lens used for focussing the beam and the rectangular aperture. Once the beam energy was known, the required energy density was obtained

Table 1 - Analysis of research iron

Element	Iron B Mass Spectrometer Analysis (ppm in weight)
Ca	0.04
Co	2.
Cr	0.5
Cu	2.
Mn	0.6
Mo	<0.2
Ni	1.
P	0.05
S	0.2
Si	<1.5
Ti	<0.1
Zn	<0.6
C	1.7[a] - 7[b]
H	0.1
N	<0.3[a] - <0.4[c]
O	1.5

a - Internal friction analysis.
b - Combustion-conductometric analysis
c - Vacuum fusion analysis

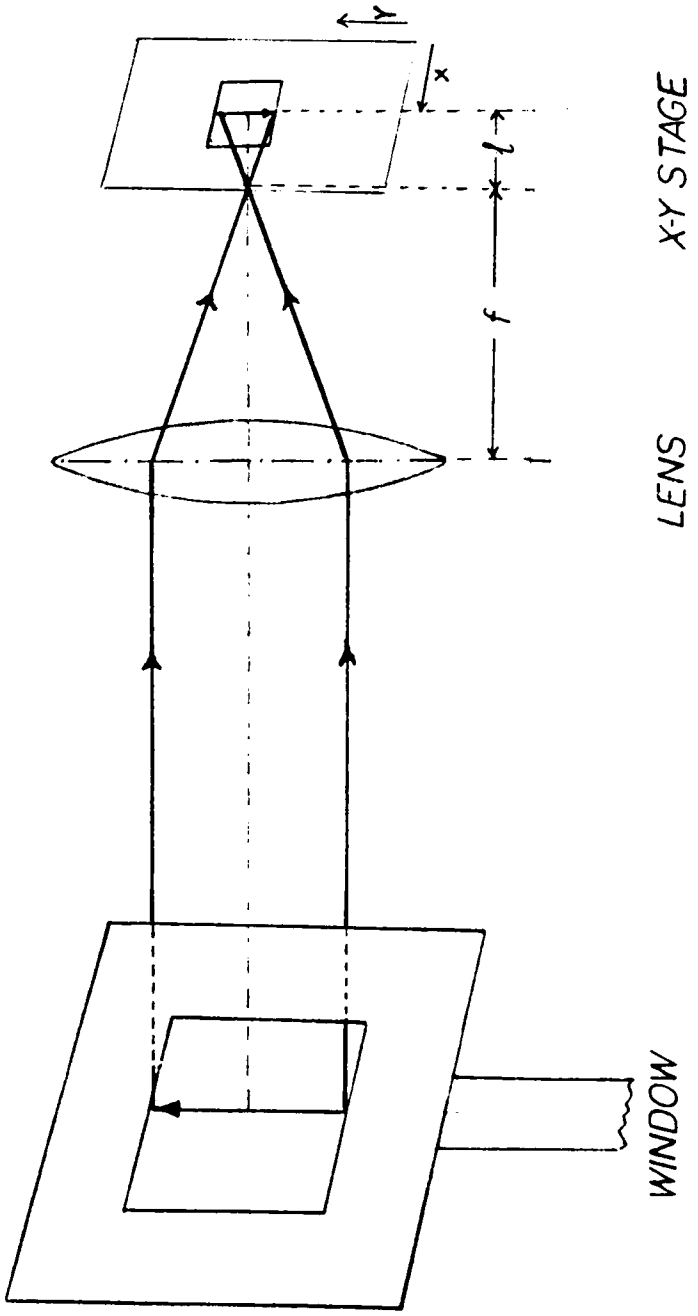


Fig. 9 - A schematic ray diagram of the lens system used for obtaining a range of energy outputs.

by moving the focussing lens so as to concentrate the beam on a smaller area. In this way an increase in the energy density at the test surface was achieved. Corrections were made to account for the reflection of the beam. Calibration was carried out every 30 minutes by first checking the instantaneous beam intensity and then by making the necessary adjustment of the lens. The energy density was increased by a factor equal to the ratio of the areas of the rectangular aperture and the beam on the test surface.

The pulsed KrF laser has a peripheral laser system consisting of a low power HeNe laser (λ = 633nm) and a silicon avalanche photodiode detector and was used for measuring the change in reflected energy from the surface of the sample while being irradiated with the excimer laser.

A Leitz Orthoplan Optical Microscope and an AMR-900 Scanning Electron Microscope were used for microstructure examination and particularly for the analysis of surface damage.

Laue back-scattering X-ray diffraction patterns were obtained on a General Electric Diffractometer with a copper tube as a source and a voltage of 30 kV and a current of 20 mA.

Microhardness measurements were performed on a Kentron microhardness testing machine with loads in the range of 10 to 50g.

$Fe_{80}B_{20}$ and Fe-Zr alloys with different Zirconium content (5, 10, 12 and 15at%) were prepared by sintering. After weighing the proper amounts, the mixtures were compacted into pellets of 10 mm diameter and 10-12 mm length in a hydraulic press. The pellets were stripped off from the die and were sealed in a quartz tube under a 10^{-5} torr

vacuum with zirconium turnings used as getter and sintered at 1100°C for 3-6hrs.

A Rigaku X-ray diffractometer in reflection mode was used for phase identification and measurement of the amorphous layer. This diffractometer system is interfaced with a PDP 11/34 computer with software for qualitative as well as quantitative analysis. The system has its own microprocessor and can be used indepedently of the PDP 11/34 computer. The microprocessor can be programmed to give the desired conditions for an X-ray scan. These conditions include a step scan or a continuous one, axis of rotation, number of cycles, starting and finishing angle, scan speed and time constant. The peak information can be stored in the computer or recorded on a chart paper. The X-ray source was copper and was operated at 35kV and 20mA. A typical user program is shown in Figure 10.

The splat quenched specimens were prepared as follows:

1) First, the sintered pellets were cut, pickled in HCl to remove oxides and dirt and weighed to group them in different weight ranges.
2) A selected piece was then carefully placed upright on a copper anvil which was resting on three pieces of indium and was levelled to match the spring-loaded hammer also made of copper.
3) The glass chamber was closed and evacuated to about 20μm of mercury and flushed with Argon 3 times.
4) The chamber was next filled with argon and an arc was struck on a niobium grounding post. A piece of

Program No. 11

Mode	Continuous scan
Recycle	1
Axis	2θ/θ
Start angle	20.00
Stop angle	120.00
Scan speed	4°/min
Full scale	1000 counts
Time constant	0.2s
Chart speed	40mm/min

Fig. 10 - A typical user program used in X-ray diffraction work.

zirconium, used as a getter, was melted and then the sample was melted on the copper anvil.

5) The arc was removed after the sample was completely molten and the hammer was released to strike on the anvil. The hammer struck the anvil and a splat quenched specimen was produced.

Samples for optical microscopy and scanning electron microscopy were made by electrolytic polishing and etching with either nital or picral. The transmission electron microscopy (TEM) samples were made by thinning the discs in a standard thinning apparatus. The discs were cut out by punching or by spark erosion method for very brittle samples. The thinning was carried out in an electrolyte of 4.5% Perchloric acid with balance Ethanol at -10°C with a current of ≈ 125mA. The TEM work was performed on a JEOL-100C with antimagnetic pole pieces at the Metals and Ceramics Division of ORNL.

CHAPTER 6

RESULTS

6.1 Pure Iron

Iron samples were used for determining the optimum energy density range required to melt the sample uniformly without causing an extensive surface damage. This energy density was used in all further experiments with iron and its alloys.

Energy densities from $0.5J/cm^2$ to $4.5J/cm^2$ were used in steps of $0.5J/cm^2$. Scanning electron microscopy (SEM) and optical microscopy (OM) were unable to show the actual surface melting in the low energy density range of $0.5 - 1.5J/cm^2$. The occurence of some melting in these low energy densities was evident from the diffraction marks produced at the edge of the masked area in the form of molten and unmolten regions due to the diffracted intensity maxima and minima. These are caused when the gap between the masking material and the sample surface gives rise to zones of alternate intensity maxima and minima as a result of the diffraction through the edge of the slit. The effect was seen at intensities as low as $1.0J/cm^2$. Figure 11 shows one such diffraction pattern at $1.5J/cm^2$. At higher energy densities, melting was revealed by surface ripples found on the irradiated samples at high magnification with an SEM. Figure 12 illustrates uniform melting at the energy density of $2.5J/cm^2$. Melting is observed to be uniform without much surface damage up to about $3.0J/cm^2$, above which the laser beam becomes quite non-uniform. The reason for this non-uniformity is that beam divergence angles are different in vertical and horizontal planes which

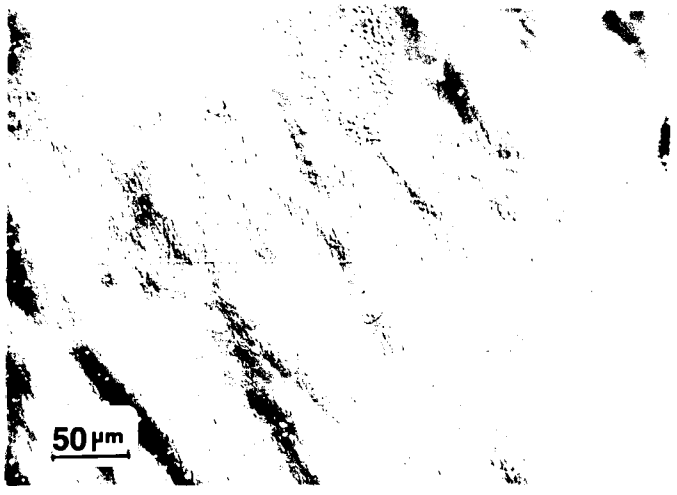


Fig. 11 - Diffraction marks produced at the edge of the masking tape. The energy density used is $1.5 J/cm^2$.

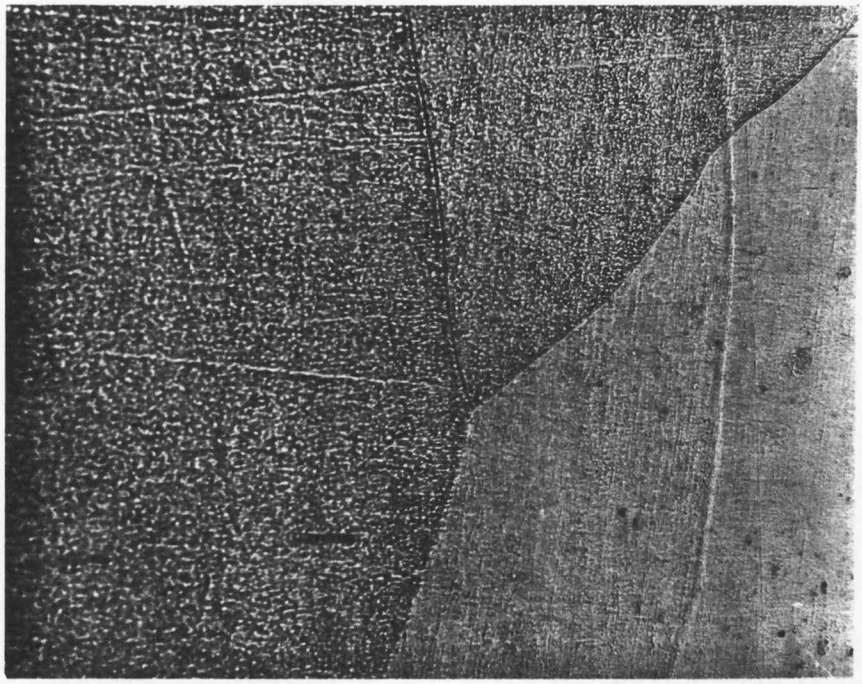


Fig. 12 - Uniform melting of the pure iron polished surface observed at $2.5J/cm^2$.

results in a line focus. High electric fields due to focussing lead to breakdown of air making the beam locally non-uniform. Also during the time the pulse is active, the reflected beam interferes with the incident beam either constructively or destructively. Figure 13 shows a central unmolten spot (non-melting is evident from the presence of the scratches) which is surrounded by a highly damaged wavy pattern of the molten material. The laser beam energy distribution at $4.0J/cm^2$ and above is extremely non-uniform and hence undesirable. Among all the energy densities tested, $3.0J/cm^2$ gives optimum results, viz. uniform melting and low surface damage.

Experiments intended to measure surface reflectivity gave somewhat unexpected results. Figure 14 shows the energy received by the silicon photodiode detector as a function of time. The reflectivity of a polished iron surface for the wavelength of 633nm (HeNe laser) is between 45 and 50%. Since liquid iron has lower reflectivity compared to a well polished solid iron surface, the energy absorbed by the laser should decrease. Instead, an enormous increase in the energy was apparent, probably orders of magnitude higher. The detector is sensitive to a very narrow window of wavelengths around 633nm. Since the absorbed energy indicates more than 100% reflectivity, it is clearly caused by luminiscence from a source other than the HeNe laser. The increase in energy lasted for about 70ns. The energy density used in this experiment was $3.0J/cm^2$ to ensure uniform melting.

Experiments done to determine the solidification mode revealed the presence of epitaxial regrowth. Samples with large grains were etched to reveal the grain boundaries and only a part of their surface

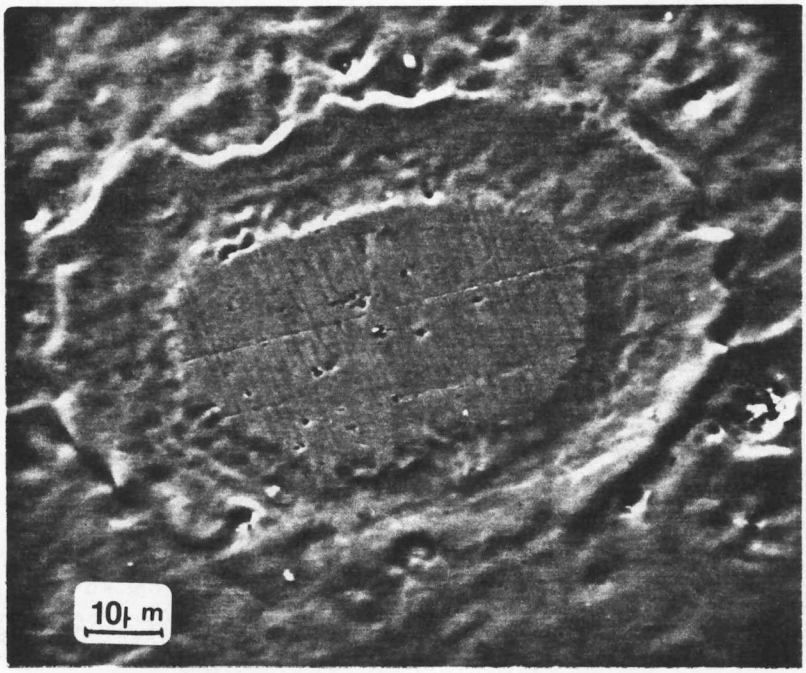


Fig. 13 - An unmolten island in a laser irradiated pure iron sample. The presence of polishing scratches confirms that the island has not been melted. The energy density was $4.7 J/cm^2$.

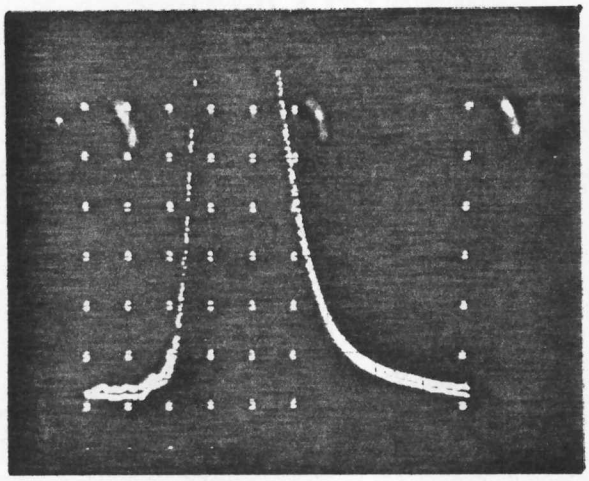


Fig. 14 - Pure iron reflectivity measurement. The excessive increase in the energy received by the silicon photodiode detector is because of the light flash observed during laserr irradiation. The ordinate is 100mV per division and the abscissa is 20ns per division.

was irradiated. The grain boundaries remain in the same position as before melting, as seen in Figure 15, indicating that epitaxial regrowth has occured. An additional confirmation of this result was sought with the following experiment. A single crystal sample checked by a Laue back-scattering pattern, was laser irradiated and another Laue back-scattering pattern was taken to see any changes in the structure. Figure 16 reveals that there is indeed no change in the structure of the sample and that solidification took place epitaxially. Furthermore, hardness measurements done inside the irradiated region did not differ from those ones taken outside. Hardness measurements in the irradiated region are difficult because of the wavy nature of the surface and the small load that has to be applied in order to measure hardness in such a thin layer. Under those conditions, however, the hardness readings inside the irradiated region did not differ from those taken outside. The microhardness results obtained reveal that the hardness in the matrix is about 75 DPH whereas that in the irradiated region is about 90 DPH. Within the experimental error of 10 DPH, the results are the same for two different energy densities, viz. $2.0 J/cm^2$ and $4.5 J/cm^2$.

The melt depth measurements were done using a "step-by-step surface removal by mechanical polishing technique". In this technique, a plate sample with a laser irradiated region is indented at all four corners of the plate by a 136° apex angle diamond pyramid indenter using a microhardness testing machine. Figure 17 shows a schematic illustration. The diagonals of the indentations are measured and noted down. This sample is then mounted and polished on a 0.06μm alumina polishing

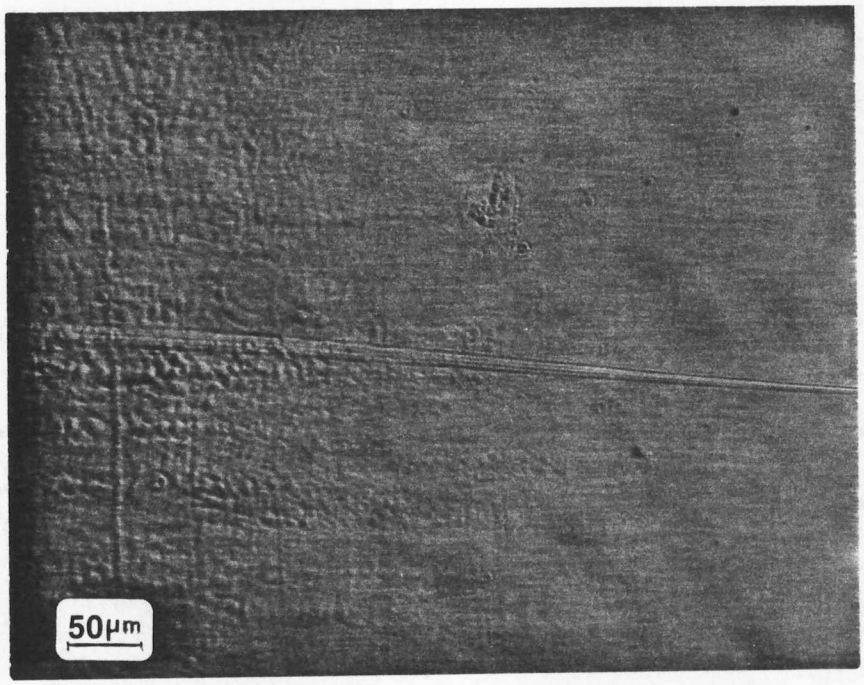


Fig. 15 - Pure iron sample irradiated with an energy density of 3.0J/cm^2. The left side of the image is irradiated while the right side is unirradiated. The single grain boundary runs through both regions.

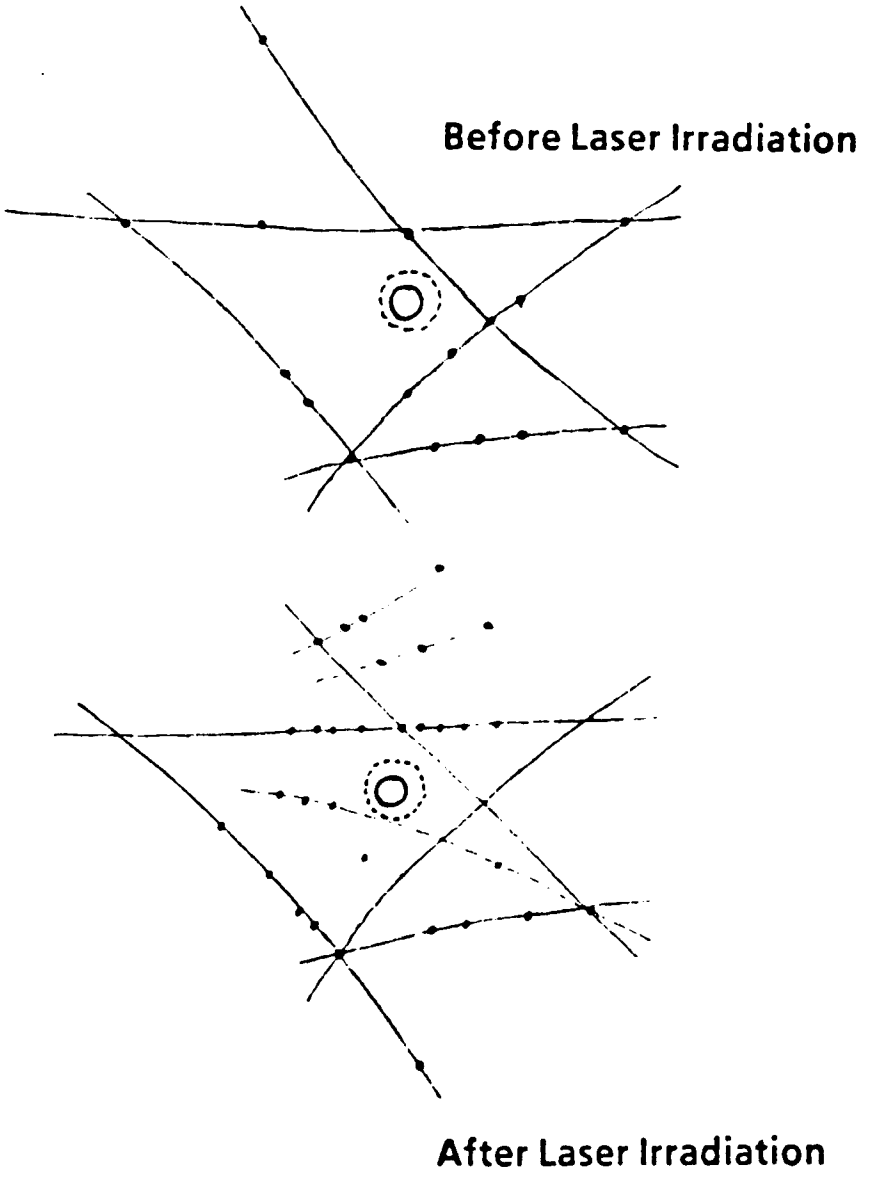


Fig. 16 - Laue back-scattered X-ray diffraction patterns for pure iron single crystal sample before and after laser irradiation. The energy density used was $3.0 J/cm^2$.

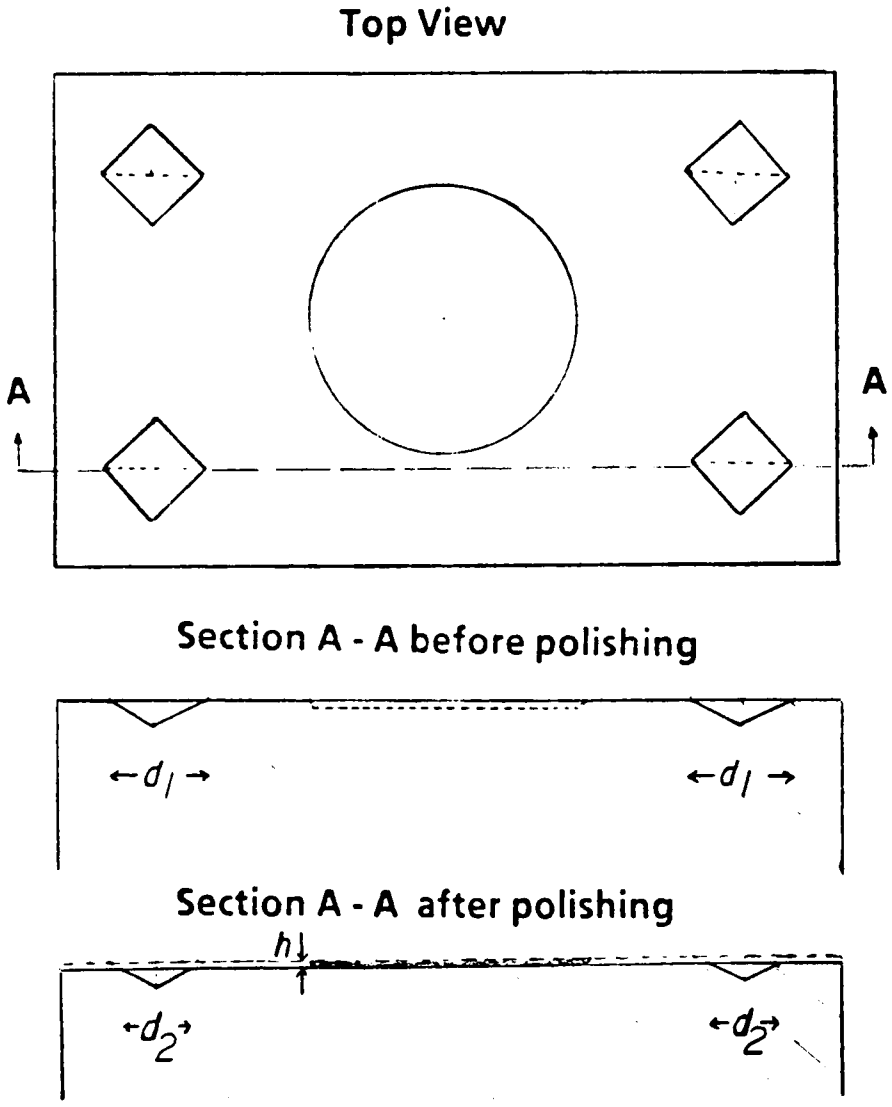


Fig. 17 - A schematic illustration of the 'step-by-step surface removal by mechanical polishing' method used to determine the melt depth.

wheel. The presence of the molten and regrown layer is recognized by the presence of an outline, a 'rim', at the boundary between irradiated and unirradiated regions. The polishing is carried on until the rim disappeares. The absence of the rim implies complete removal of the solidified layer. The diagonals of the indentations are then measured again and the difference with the initial reading is used to calculate the melt depth by the relation,

$$h = (d_1-d_2)/2\tan 68^\circ = 0.2(d_1-d_2)$$

where h is the melt depth, d_1 and d_2 are the diagonal lengths before and after the polishing respectively and 68° is half the apex angle.

Figure 18 shows the melt depth as a function of the input energy density. The energy densities above $4.0 J/cm^2$ do not yield good results because there are deep craters in the surface which continue to exist even after the rim is completely polished off.

6.2 Iron-Boron System

Following the initial experiment with pure iron, an $Fe_{80}B_{20}$ alloy was next investigated. This alloy is known to be an easy glass former when solidified under cooling rates of the order of $10^6 K/s$.

The alloy was prepared by a sintering and annealing technique and its microstructure inspected in the as sintered and annealed state. The microstructure exhibits precipitates of iron boride in the ferrite matrix, as shown in Figure 19, along with voids which almost always appear in a sintered structure. The sample was then mounted on a suitable holder and X-ray diffraction patterns were obtained by a continuous $2\theta/\theta$ scanning method. Figure 20 shows a scan of the

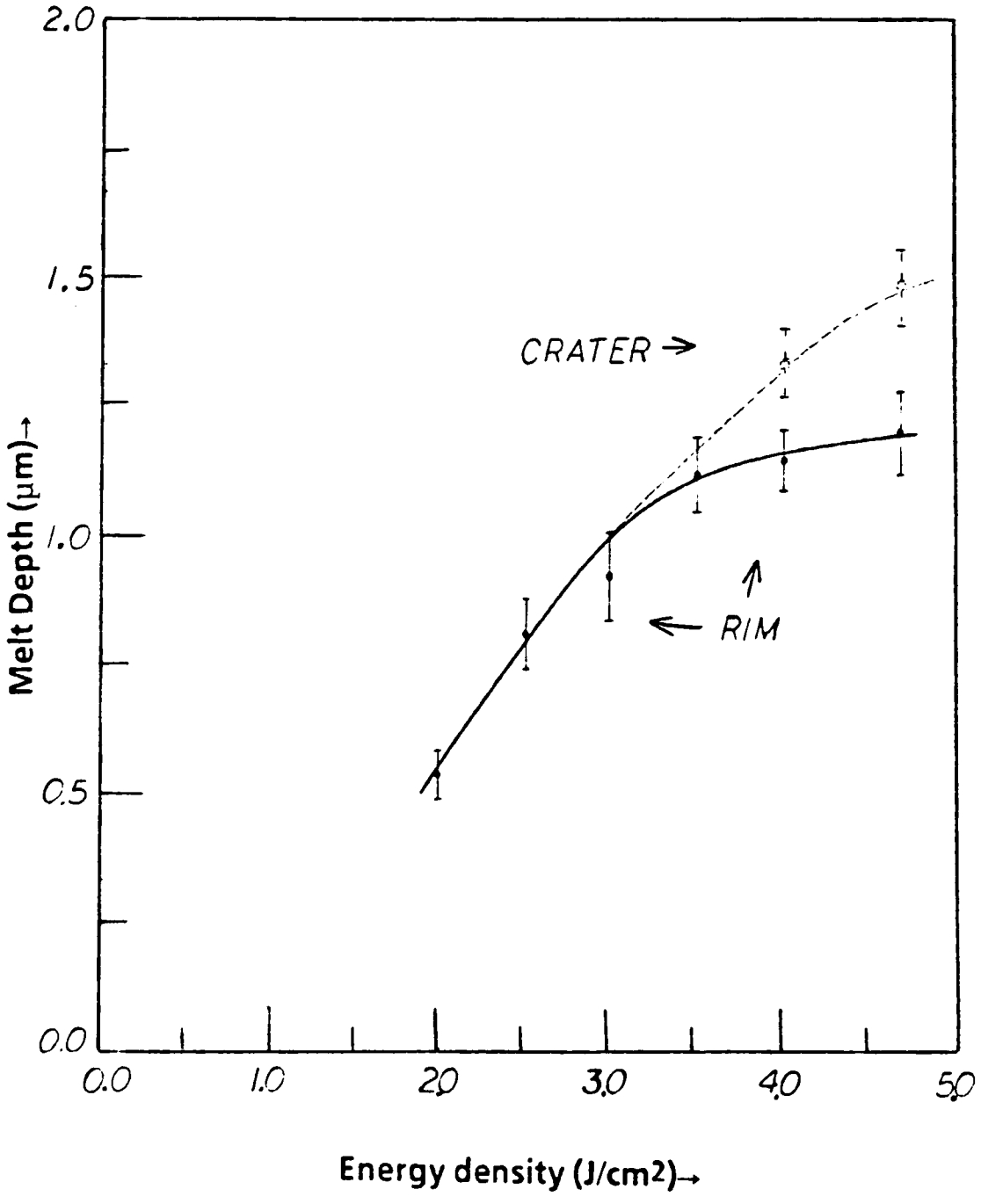


Fig. 18 - Melt depth of the laser irradiated pure iron specimens as a function of the input energy density.

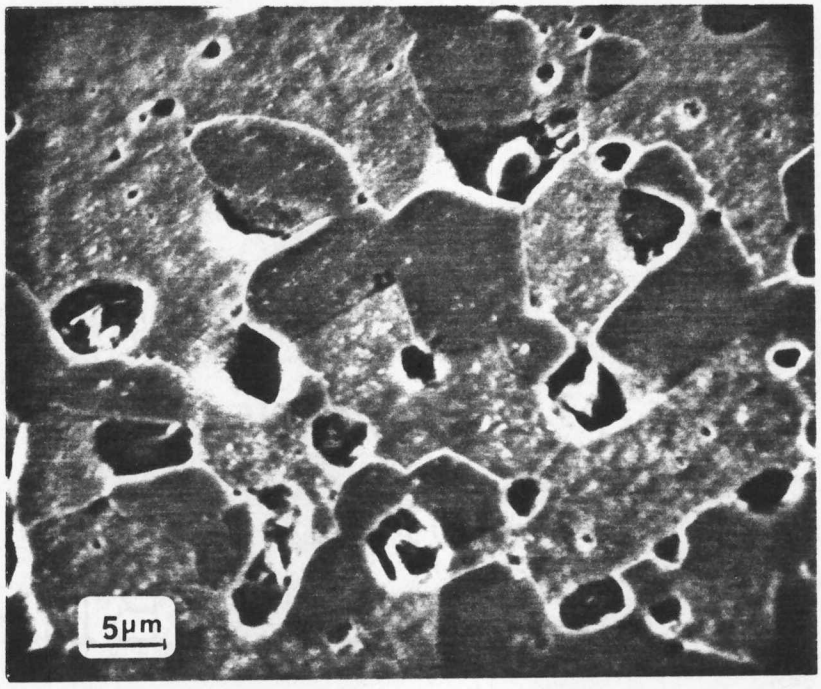


Fig. 19 - As sintered and annealed $Fe_{80}B_{20}$ structure showing precipitates of Fe_2B in ferrite matrix.

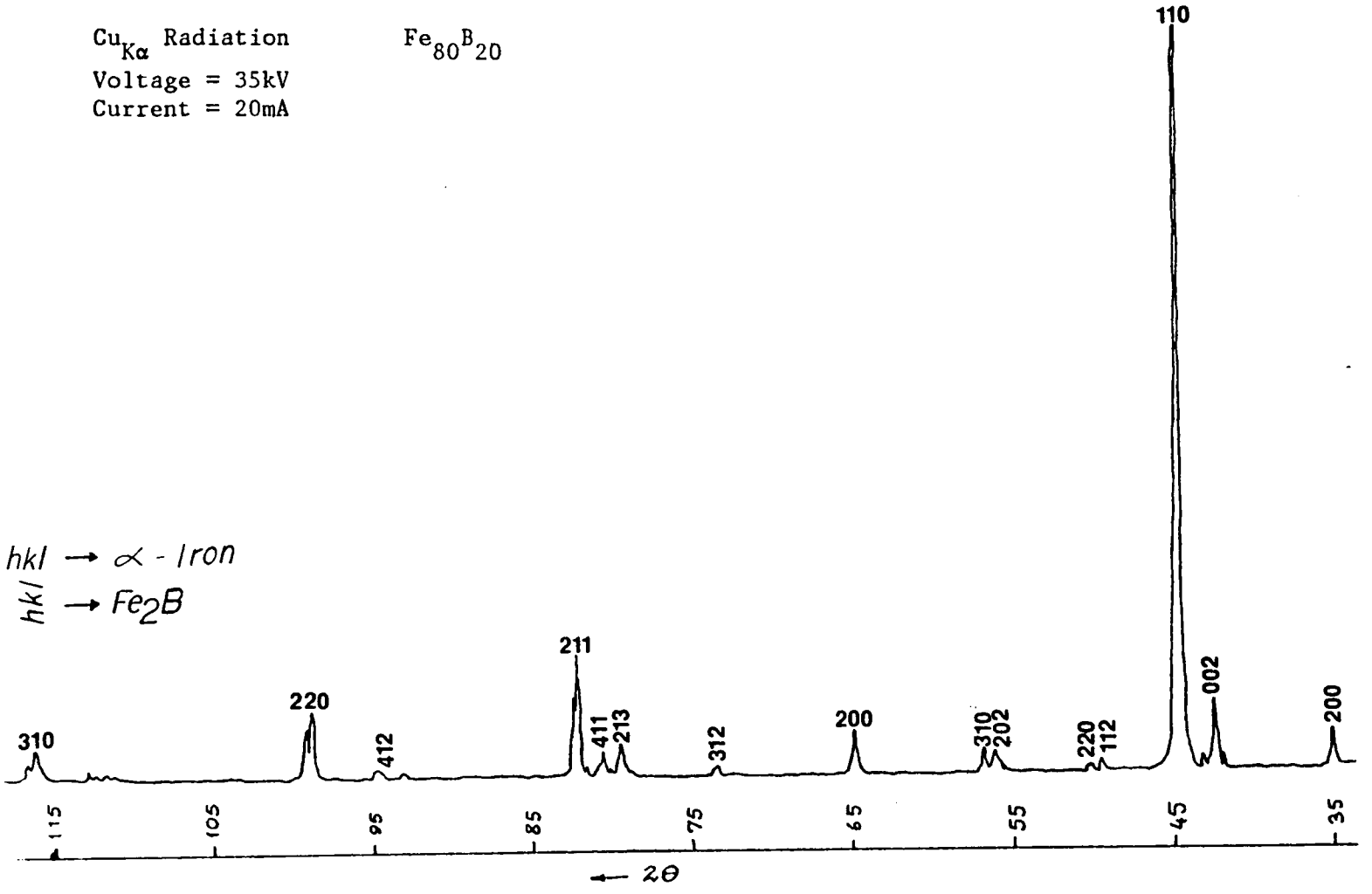


Fig. 20 - The X-ray diffractometer scan of the diffracted intensity vs. the 2θ angle for the as sintered and annealed sample of $Fe_{80}B_{20}$ alloy.

diffracted intensity vs. the angle 2θ for an as prepared sample. A comparison of the diffraction peaks with the JCPDS file cards yielded that the equilibrium phase Fe_2B was present together with ferrite. The compound Fe_2B has a tetragonal structure with lattice parameters a = 0.511nm and c = 0.425nm.

In order to get different initial conditions, splat quenched specimens were made on the hammer and anvil machine for laser irradiation experiments. The sample weights were in the range of 0.1 to 0.3 grams. The as splat quenched microstructure is extremely fine, as shown in Figure 21. An X-ray diffraction pattern was obtained on this sample to determine the phases present in the as-splat quenched condition. The diffracted intensity vs. the angle 2θ scan is shown in Figure 22 and reveals the presence of Fe_3B phase rather than Fe_2B. The non-equilibrium Fe_3B phase is also tetragonal with lattice parameters a = 0.864nm and c = 0.428nm.

The comparison of the peaks of ferrite obtained in both types of samples as shown in Figure 23 reveals that the (110) and the (220) peaks in the sintered and annealed sample are almost double in height compared to those in the splat quenched sample. Also the $K_{\alpha 1}$ and $K_{\alpha 2}$ peak resolution, present in the sintered and annealed sample, is absent in the splat quenched sample.

Both samples were then irradiated with a pulsed laser by scanning over their entire surface area. The laser beam energy density was maintained at $3.0 J/cm^2$. The results obtained showed a remarkable difference in the extent of amorphization of the two samples determined by the non-destructive surface sensitive X-ray diffraction (SSXD)

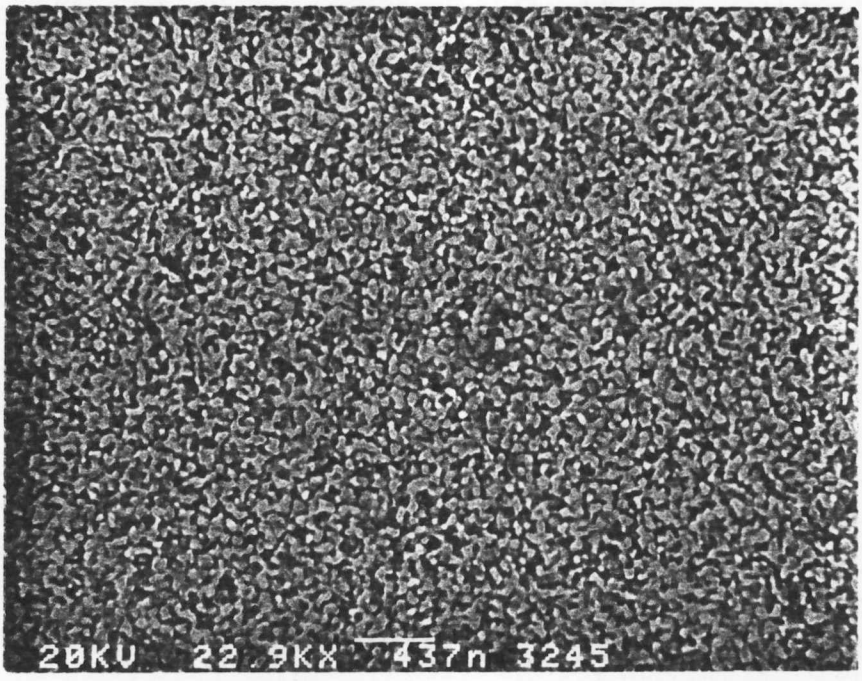


Fig. 21 - As splat quenched microstructure of the $Fe_{80}B_{20}$ alloy. The average grain size is about 60-80nm.

$Cu_{K\alpha}$ Radiation

Voltage = 35kV

Current = 20mA

$Fe_{80}B_{20}$

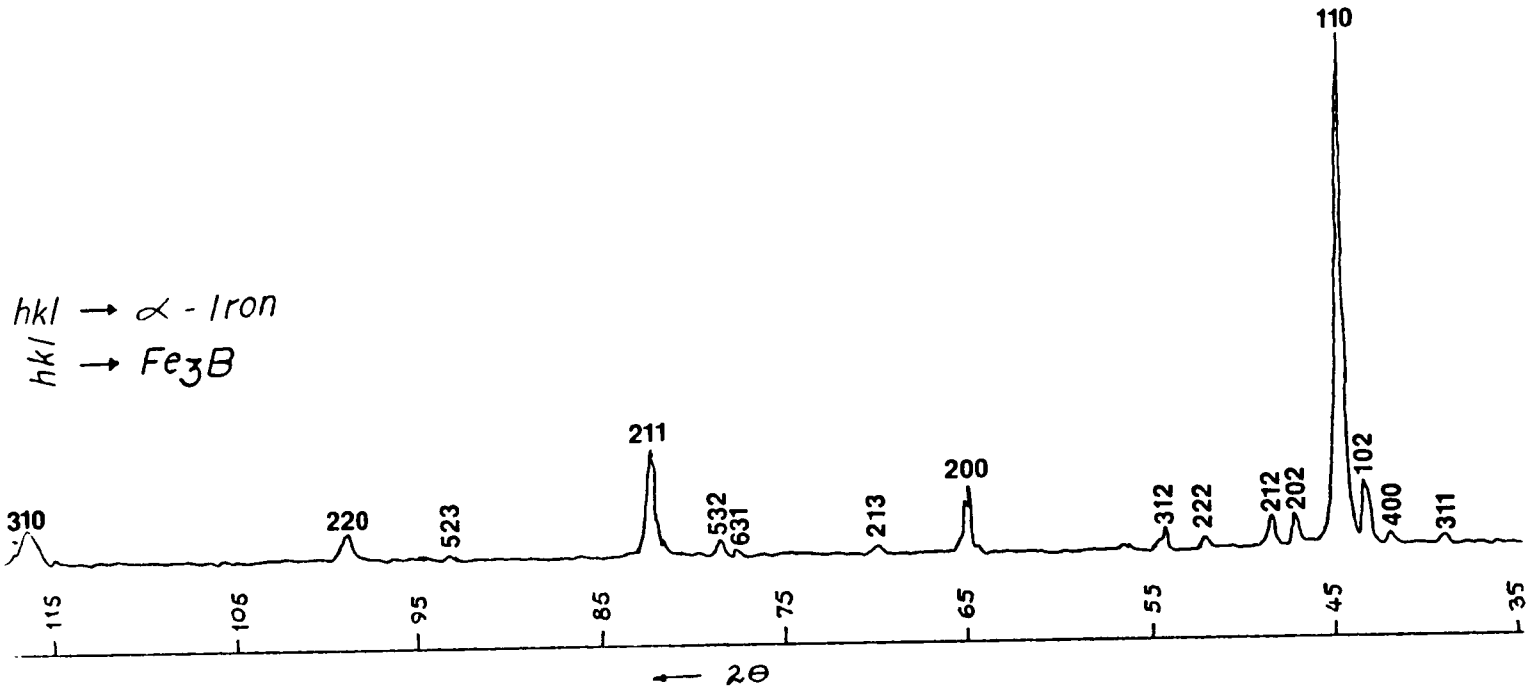


Fig. 22 - The X-ray diffractometer scan of the diffracted intensity vs. the 2θ angle for the splat quenched sample of $Fe_{80}B_{20}$ alloy.

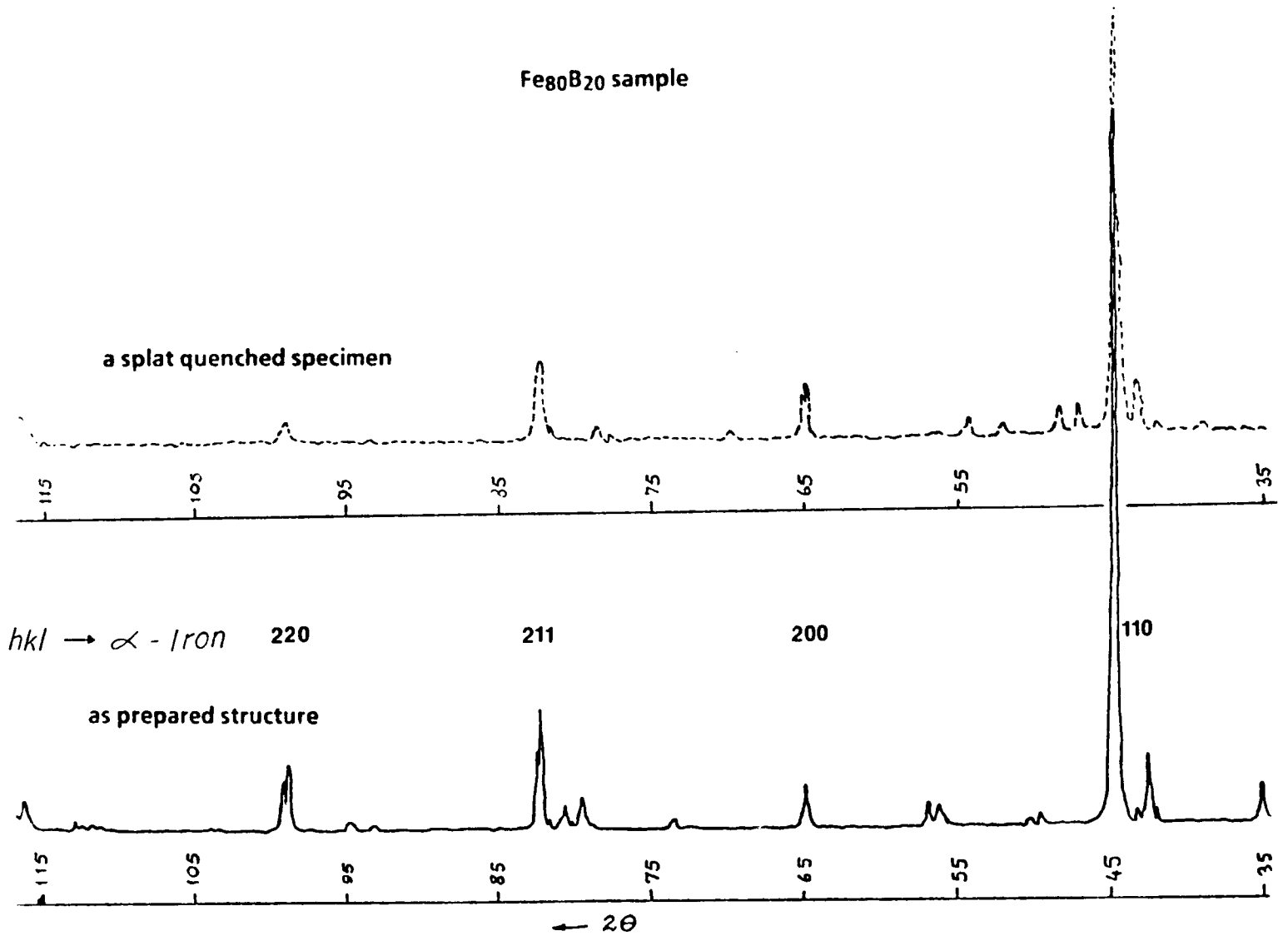


Fig. 23 - The comparison of the X-ray diffraction patterns in as sintered and annealed condition and in as splat quenched condition.

technique. This technique was developed during the course of this research work.

Complete development of the technique and the related mathematical derivations are given in the Appendix 1. Some of the salient features of the method are that it is non-destructive and that it allows one to easily and accurately determine the thickness of the amorphous layer. The technique uses an X-ray diffractometer to measure the reduction in the integrated intensity of several diffracted X-ray lines due to the near surface layer of amorphous material. The target material for the X-ray generation is selected so that the emitted X-rays are strongly absorbed by the sample. The method permits the measurement of the amorphous layer thicknesses down to about 50-100nm.

The X-ray diffraction patterns of the laser irradiated sintered and annealed sample gave very little change in the intensity of the diffracted peaks as compared to that before the irradiation. When the sample was viewed under a scanning electron microscope, it showed regions of mixing near grain boundaries between ferrite and boride particles. Figure 24 shows one such photomicrograph where a boride particle is embedded in the ferrite matrix and the region where compositional mixing has occured. From the microstructural appearence, this region may be amorphous. The width of this region is about 2.5μm.

In the case of the splat quenched sample, however, the entire surface has been amorphized. The X-ray diffraction pattern after laser irradiation shows a marked difference from its counterpart taken before irradiation. Figure 25 shows the comparison of the two patterns and

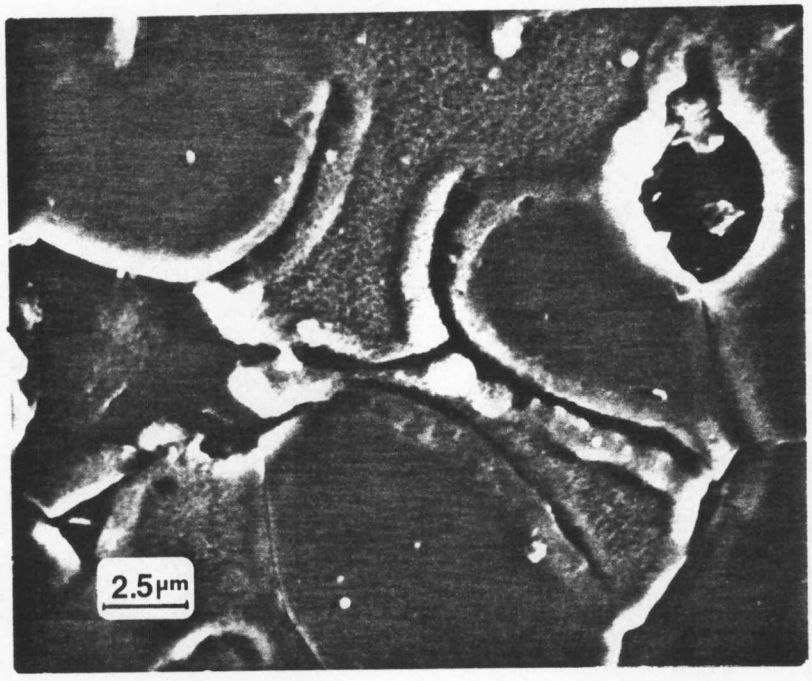


Fig. 24 - Sintered and annealed $Fe_{80}B_{20}$ after laser irradiation.

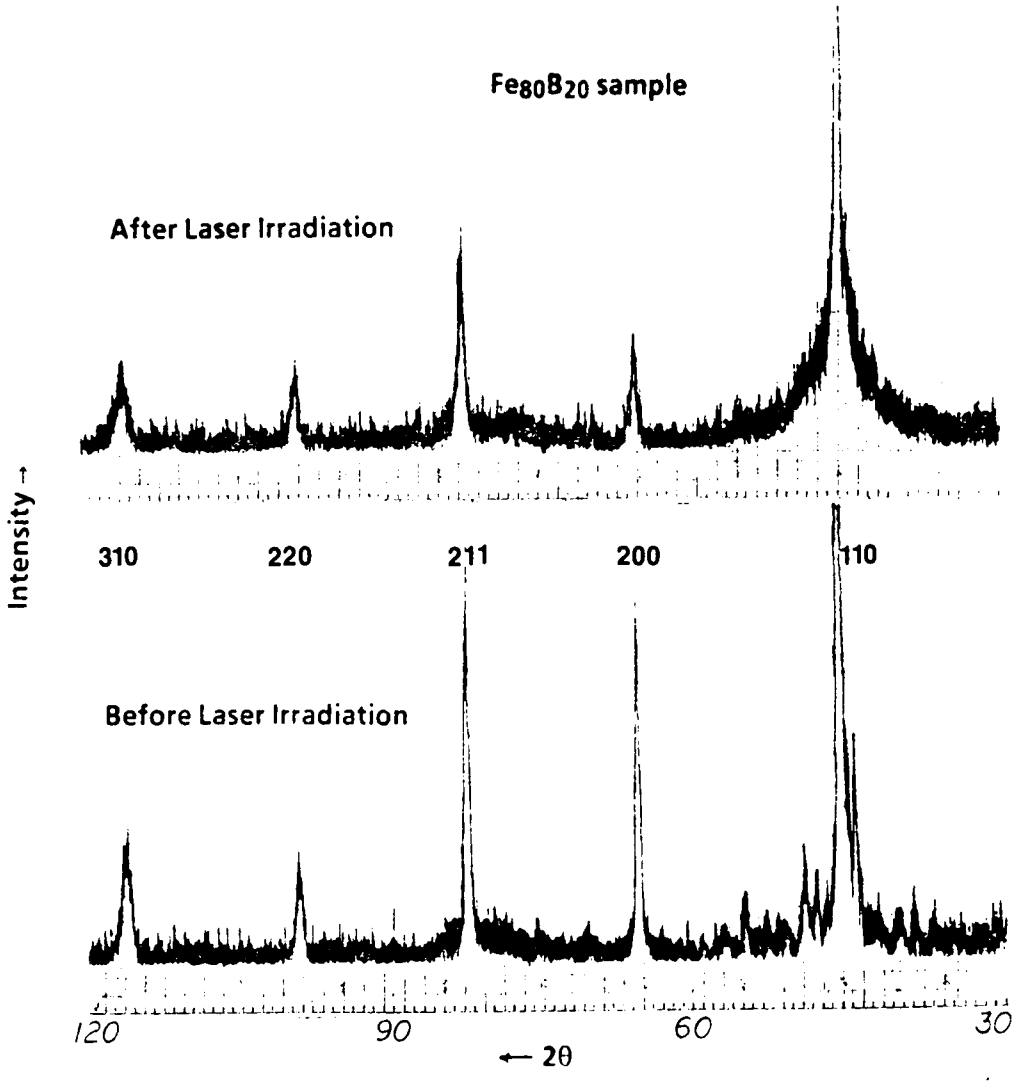


Fig. 25 - The comparison of the X-ray diffraction patterns in the splat quenched condition before and after laser irradiation.

reveals that there is an amorphous hump that appears at the (110) ferrite peak which is characteristic of amorphous $Fe_{80}B_{20}$. Figure 26 shows the X-ray diffraction pattern of an $Fe_{80}B_{20}$ amorphous ribbon prepared by the melt spinning technique that was used as a reference. The amorphous layer thickness calculations were done using the surface sensitive X-ray diffraction (SSXD) method described in Appendix 1. The result shows the layer thickness to be 1.5μm which is close to the earlier melt depth measurements done for the pure iron specimens.

6.3 Iron-Zirconium System

In order to study the Fe-Zr system in the vicinity of the iron rich eutectic, four different alloys with 5, 10, 12 and 15at%Zr were prepared by the sintering and annealing technique.

The X-ray diffraction analysis of these samples in all the four cases reveals that there are three phases present- large amounts of ferrite and Fe_3Zr which are equilibrium phases and a small amount of Fe_2Zr which is a metastable phase for the composition used. The presence of Fe_2Zr can be explained on the basis of diffusion of zirconium in iron. When zirconium starts to diffuse into iron, it forms a large number of intermetallics from the zirconium rich side to the iron rich side. The other intermetallics dissolve with time, but the Fe_2Zr remains. In fact earlier Fe-Zr phase diagrams did not show the presence of Fe_3Zr at all. Instead, Fe_2Zr was the phase present even at low Zr contents.

These samples were then splat quenched for a similar purpose to that explained in the case of the Fe-B system. The splat quenched

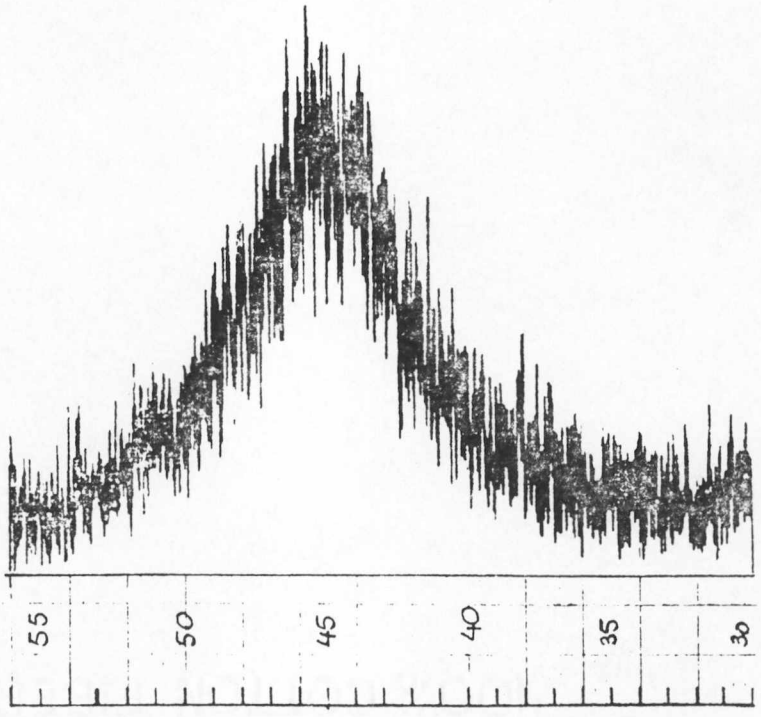


Fig. 26 - The X-ray diffractometer scan of the diffracted intensity vs. the 2θ angle for an amorphous ribbon of $Fe_{80}B_{20}$ alloy prepared by the melt spinning technique.

$Fe_{90}Zr_{10}$ and $Fe_{88}Zr_{12}$ alloys are amorphous when the sample weight is less than or equal to 0.05gms. Between 0.05 and 0.12gms, the splat quenched samples are partially amorphous and partially crystalline and above 0.12gms, they are completely crystalline. Figure 27 shows the X-ray diffraction patterns of the amorphous and the crystalline $Fe_{90}Zr_{10}$ samples in the as splat condition. The pattern of the amorphous sample exhibits the characteristic hump whereas that of the crystalline sample shows numerous peaks. When the crystalline peaks were analyzed, the match showed a mixture of two phases, ferrite and Fe_2Zr unlike the three phases found in sintered and annealed specimens as can be seen in Figure 28. Fe_2Zr is a metastable phase for these compositions which appears in the phase diagram for high zirconium contents and has a melting point much higher than the eutectic temperature. Samples of $Fe_{85}Zr_{15}$ and $Fe_{95}Zr_5$ do not amorphize on splat quenching but are crystalline. The $Fe_{95}Zr_5$ is quite ductile whereas $Fe_{85}Zr_{15}$ is extremely brittle.

Optical microscopy of the cross-section of the amorphous samples reveals that they are mostly free of large crystalline phases resolvable at the optical level. In one case, though, a uniformly crystalline layer was found about 9μm below the surface as shown in Figure 29. The crystals were not revealed by the X-ray diffraction method because the crystallites are 9μm away from the surface and only the first 3μm are probed by the X-rays (see Appendix 1).

The TEM observations of the samples revealed an amorphous matrix whereas some areas showed the coexistence of amorphous and crystalline material. Figure 30 shows one such area where the crystallites were

$Cu_{K\alpha}$ Radiation $Fe_{90}Zr_{10}$
Voltage = 35kV
Current = 20mA

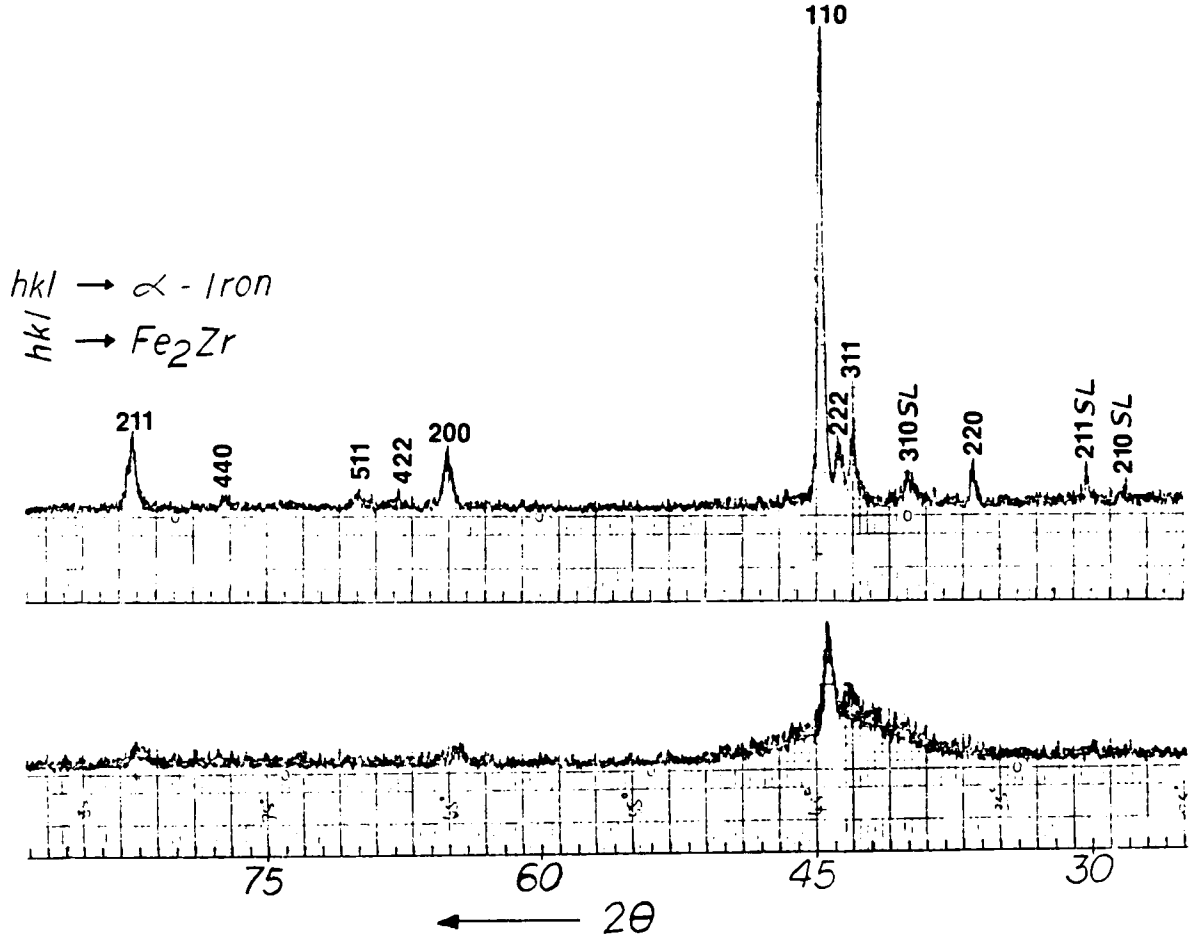


Fig. 27 - The X-ray diffractometer scan of the diffracted intensity vs. the 2θ angle for an as splat quenched amorphous and as splat quenched crystalline sample of $Fe_{90}Zr_{10}$ alloy.

Fe - Zr Phase Diagram

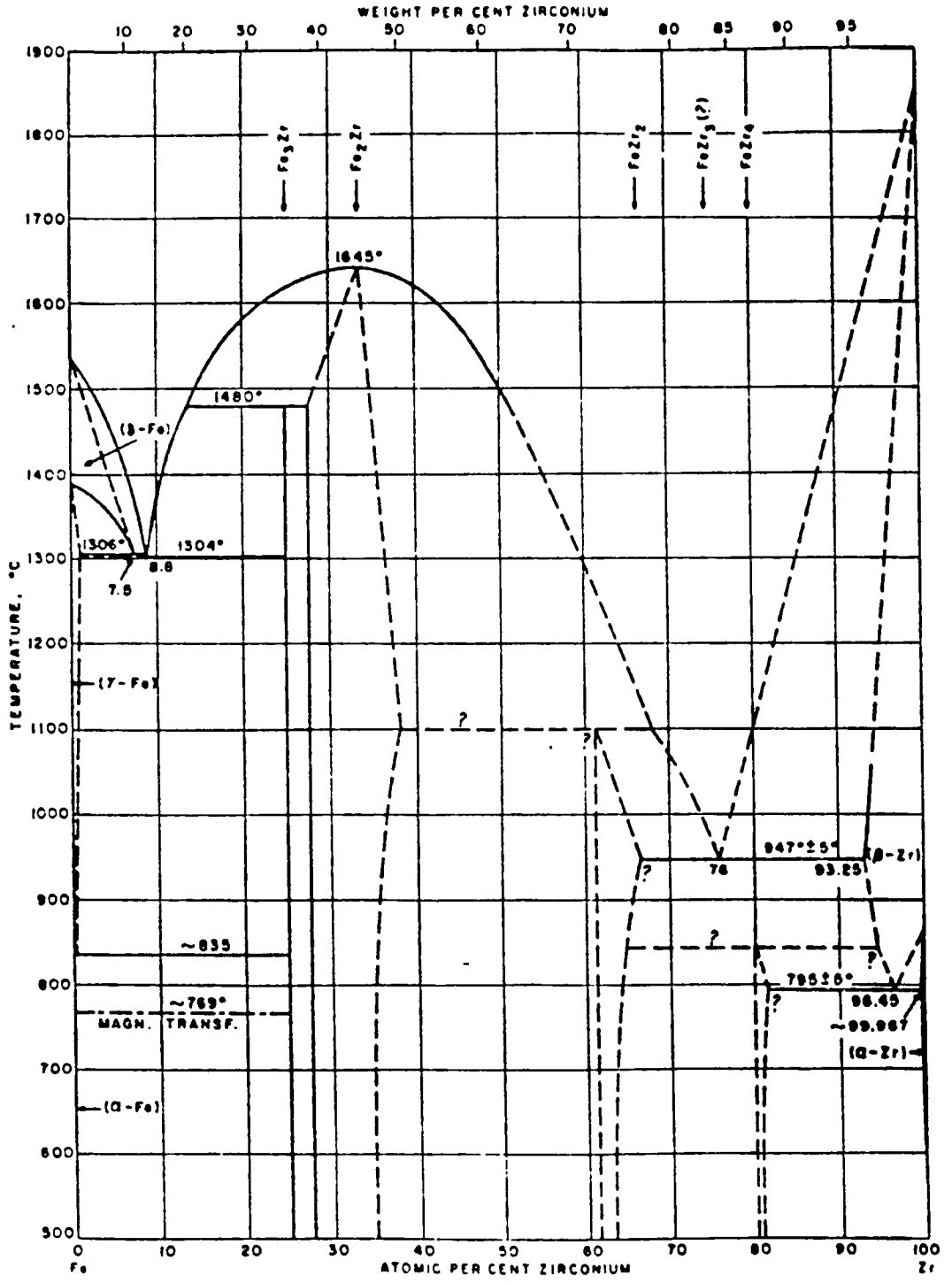


Fig. 28 - The Fe-Zr phase diagram
Source: 'Constitution of Binary Alloys'(second supplement), by F.A.Shunk, McGraw-Hill, (1969), 356

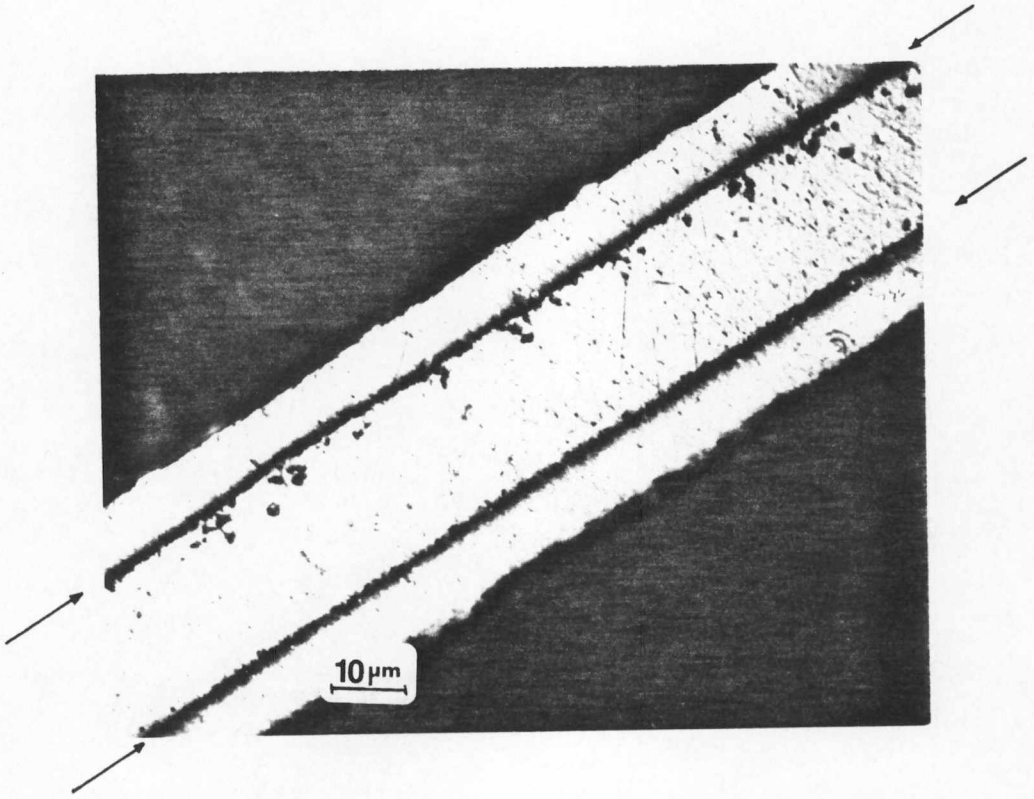


Fig. 29 - The cross-section of an $Fe_{90}Zr_{10}$ as splat quenched amorphous film showing the presence of a crystalline layer beneath each surface.

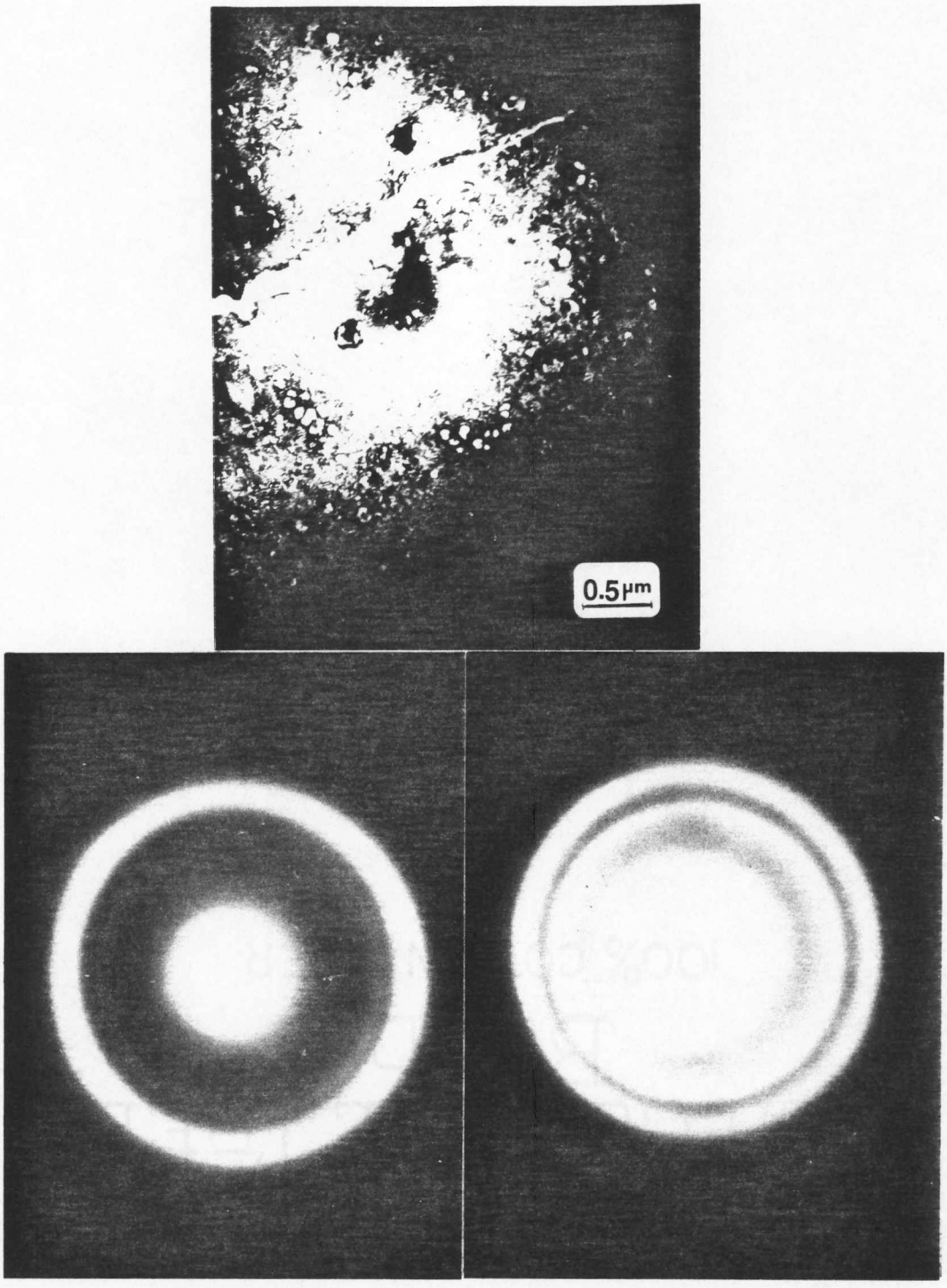


Fig. 30 - TEM image of an $Fe_{90}Zr_{10}$ as splat quenched amorphous sample showing a distribution of fine precipitates. The corresponding diffraction patterns in the amorphous matrix(left) and in the matrix with the precipitates(right).

embedded in the amorphous matrix. The figure also contains the corresponding electron diffraction patterns. The crystallites viewed under higher magnification exhibit a spherulitic nature. Figure 31 shows these spherulites at four different magnifications. The composition analysis reveals that the central particle is rich in zirconium and it forms the nucleus. The surrounding Zr depleted region triggers off a transformation reaction which leads to the formation of a branched spherulitic structure. Apart from these spherulites, the amorphous films also contained some particles extremely rich in zirconium and some very fine crystallites apparently rich in iron.

The composition analysis of the zirconium rich precipitates and the matrix is given in Table 2. The electron diffraction pattern from one such precipitate as in Figure 32 was indexed and the lattice parameter calculated. The camera constant was determined from the Aluminum diffraction pattern under identical conditions. Using this value of the camera constant, the lattice parameter of the BCC lattice was found to be 0.3446 nm which is intermediate between those for pure BCC iron (0.2866nm) and BCC zirconium (0.3609nm). The interpolation using Vegard's law gives the corresponding composition as Fe-78at%Zr whereas the value from the composition analysis gives Fe-93at%Zr. Thus, the lattice parameter vs. the composition curve exhibits an upward concave nature, as shown in Figure 33. The precipitates appear to be β-Zr which has a higher solubility for iron than α-Zr which is the stable phase at lower temperature.

The crystallites rich in iron are extremely small in size, of the order of 10-20nm. Figure 34 shows the fine microstructure of these

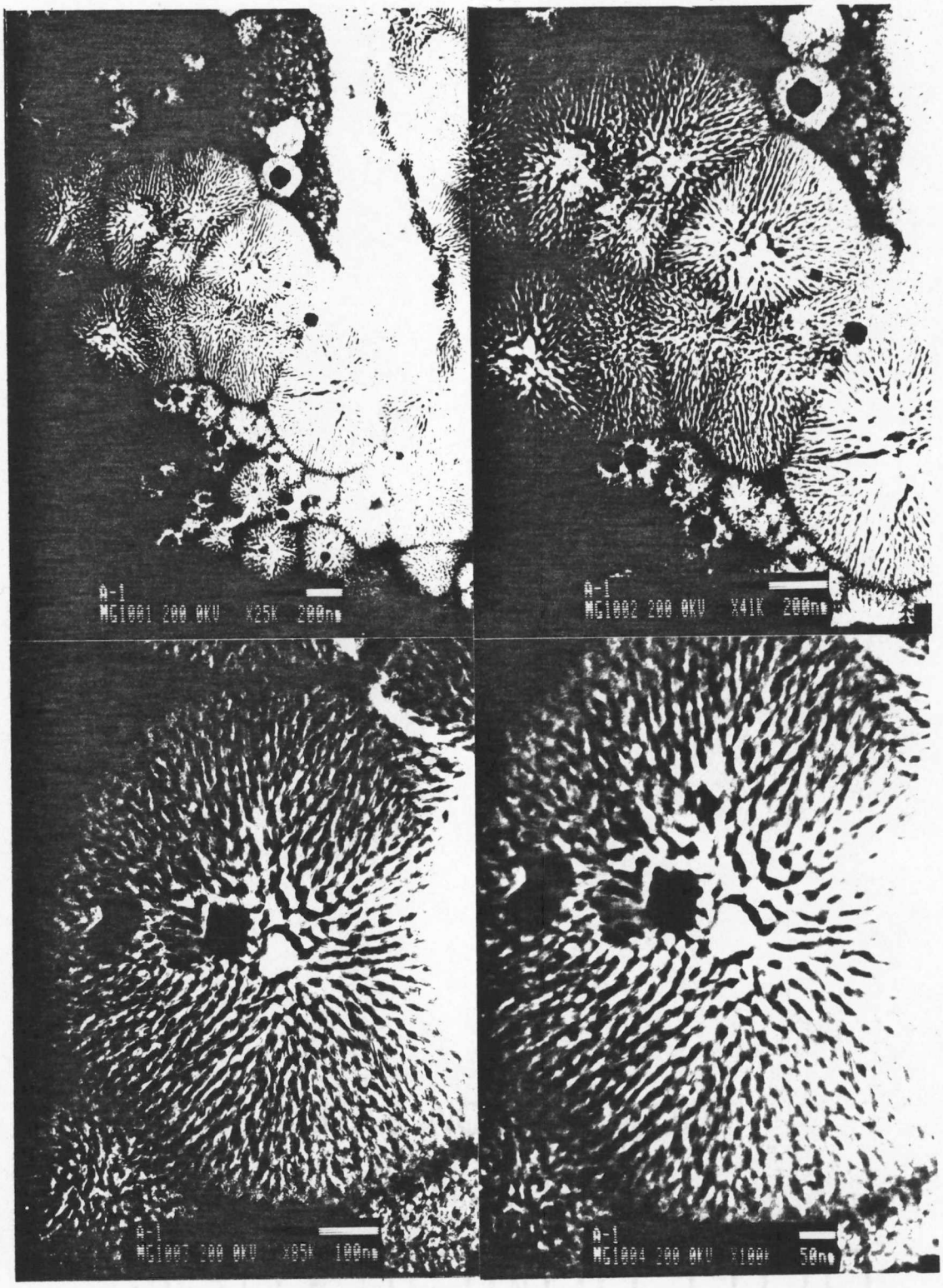


Fig. 31 - TEM image of the spherulitic precipitates in the $Fe_{90}Zr_{10}$ as splat quenched amorphous film at four magnifications.

Table 2 - Average chemical composition of the Zr-rich precipitates

ELEMENT LINE	PEAK COUNT	K-FACTOR	$\frac{C_{EL}}{C_{REF}}$	AT% ELEMENT
Fe-K	2334	1.00	1.00	6.60
Zr-K	12349	2.61	13.81	91.03
Hf-L	340	2.49	0.36	2.37

Beam Direction (100)

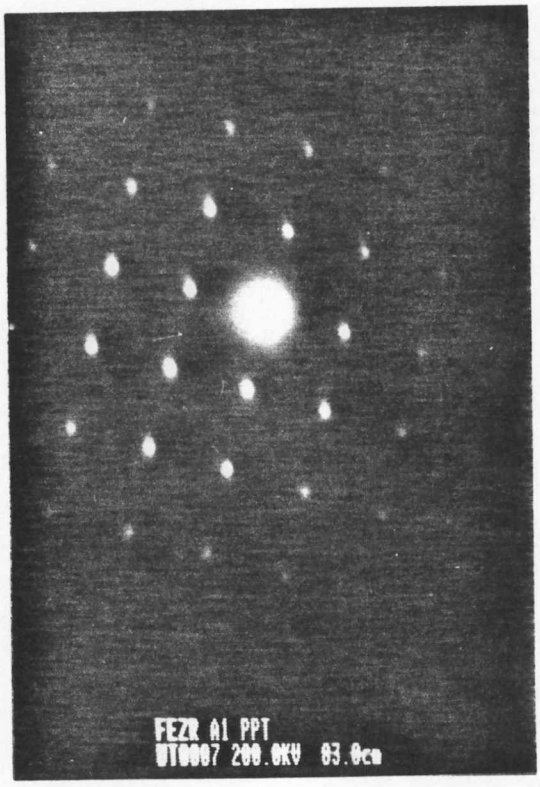


Fig. 32 - A diffraction pattern from a Zr-rich precipitate.

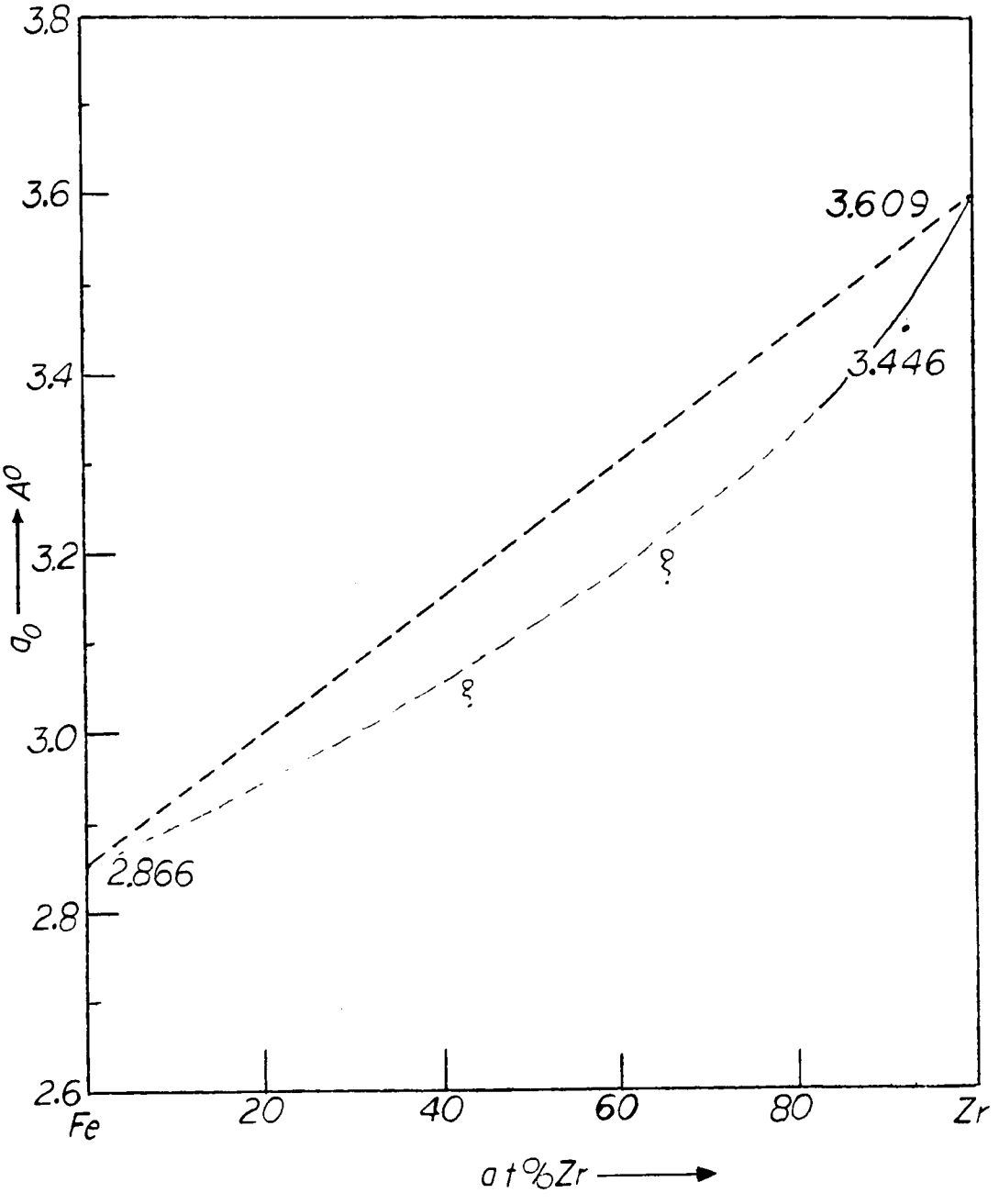


Fig. 33 - The lattice parameter vs. the composition curve for a metastable β-Zr phase showing an upward concave nature.

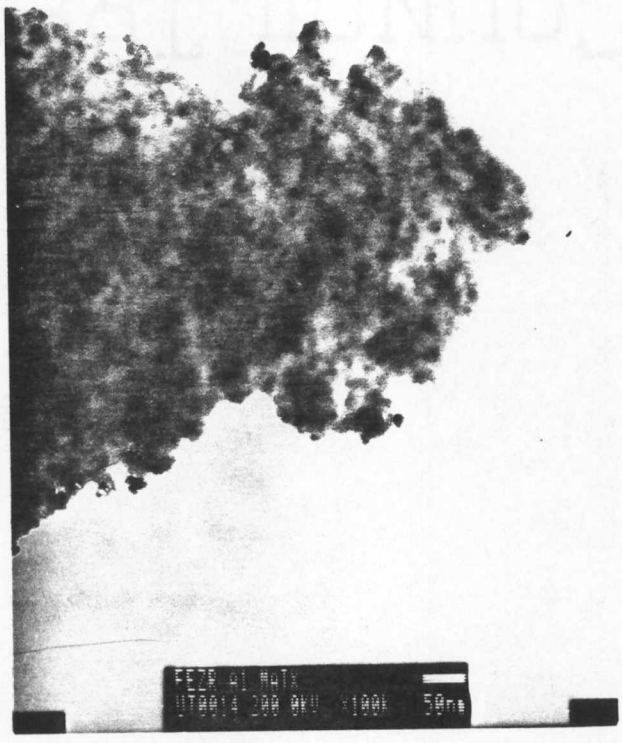


Fig. 34 - TEM image of the $Fe_{90}Zr_{10}$ as splat quenched amorphous film showing a dispersion of Fe-rich fine precipitates.

particles in the amorphous matrix. The electron diffraction pattern from one such particle shown in Figure 35 reveals a BCC lattice structure. The lattice parameter turns out to be 0.2813nm which is less than that for pure iron. This implies that there were fluctuations in the voltage leading to a change in the camera constant. The electron diffraction patterns are not as accurate as the X-ray diffraction patterns for the determination of the lattice parameter, but are useful when the component is present in traces.

The samples that were crystalline in the as splat quenched condition did not reveal any microstructural details when viewed under the optical microscope. When the same sample was observed by SEM, Figure 36, the microstructure was found to be extremely fine with an average grain size of 50nm. The composition analysis by EDAX always gave the same results irrespective of the aperture size. Because of the fine microstructure, it was not possible to analyse phases individualy by SEM. The identification of the two phases in a sample with such a fine microstructure may be possible only with the help of a TEM.

The splat quenched samples of three of the four Fe-Zr alloys(10, 12 and 15at%Zr) became amorphous after irradiation with an excimer laser. The Fe-5a%Zr alloy showed no amorphization in the molten layer. Figures 37 and 38 show the X-ray diffraction patterns before and after the laser irradiation of the 10 and 15at%Zr-Fe samples, respectively. Table 3 summarizes the results of the thickness measurements of the amorphous layer obtained using the SSXD method.

Beam Direction (112)

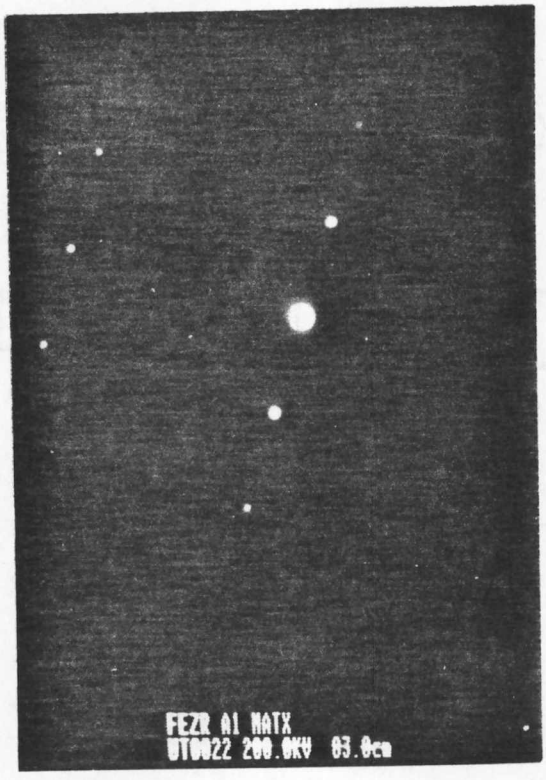


Fig. 35 - A diffraction pattern from an Fe-rich precipitate.

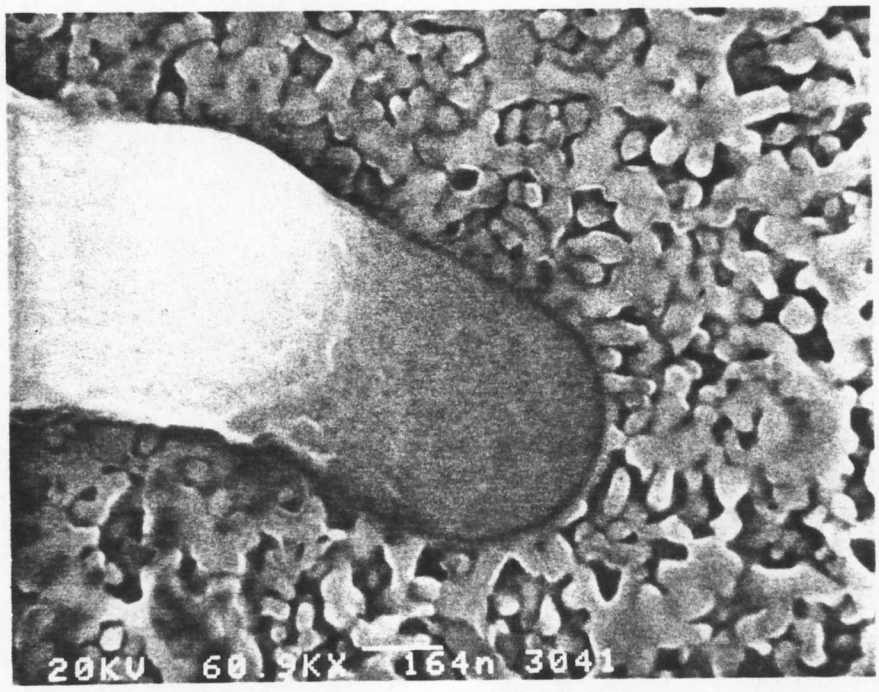


Fig. 36 - As splat quenched crystalline microstructure of the $Fe_{90}Zr_{10}$ alloy.

$Cu_{K\alpha}$ Radiation $Fe_{90}Zr_{10}$
Voltage = 35kV
Current = 20mA

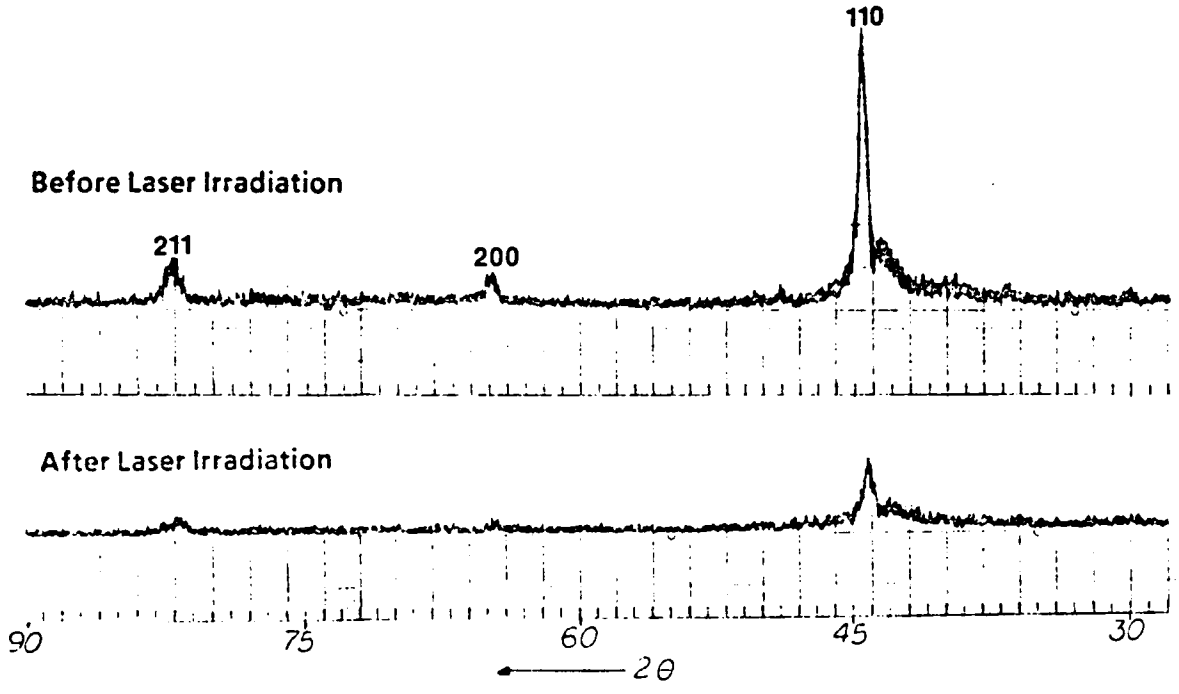


Fig. 37 - The X-ray diffraction pattern for an as splat quenched $Fe_{90}Zr_{10}$ alloy before and after laser irradiation.

$Cu_{K\alpha}$ Radiation $Fe_{85}Zr_{15}$
Voltage = 35kV
Current = 20mA

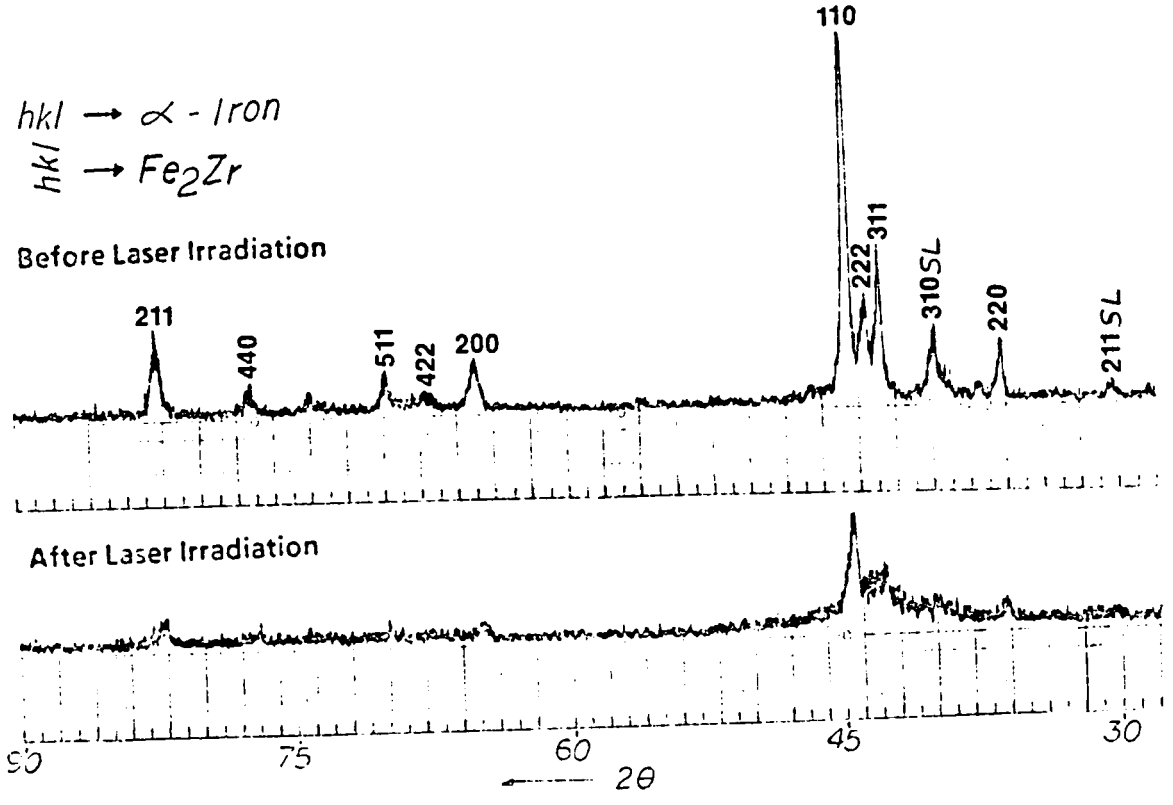


Fig. 38 - The X-ray diffraction pattern for an as splat quenched $Fe_{85}Zr_{15}$ alloy before and after laser irradiation.

Table 3 - Summary of the results of amorphous layer thickness measurements in Fe-Zr alloys.

ALLOY	THICKNESS(hkl)μm				AVERAGE THICKNESS
	200	211	220	310	(μm)
Fe90Zr10	1.84	1.74	----	1.66	1.75
Fe88Zr12	1.51	----	1.72	1.63	1.62
Fe85Zr15	1.54	1.60	----	----	1.57

In order to study the effect of the initial microstructure on the extent of amorphization when processed by pulsed laser irradiation, an amorphous sample was crystallized. X-ray diffraction confirmed the crystallization. Extensive amorphization did not occur when this specimen was laser irradiated as seen from the X-ray diffraction pattern. Figure 39 clearly shows that the microstructure in the annealed condition consists of a dispersion of the Zr-rich phase in ferrite. This structure, though fine, is approximately one order of magnitude larger than that of the splat quenched sample. The composition analysis did not allow to discriminate compositional variations from one phase to another because of the fine microstructure.

A laser irradiated film was mounted to see the amorphized layer under the optical microscope. Figure 40 shows the amorphous layer on the laser irradiated side. The width of this amorphous layer is about 1.4μm, in close agreement with the results obtained from the SSXD method.

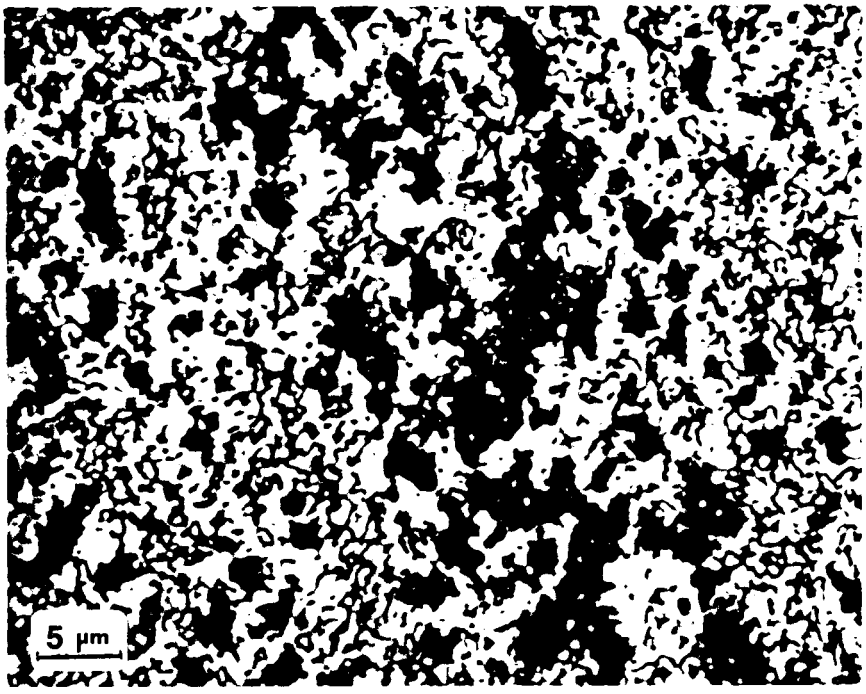


Fig. 39 - Microstructure of a crystallized amorphous film of an $Fe_{90}Zr_{10}$ alloy.

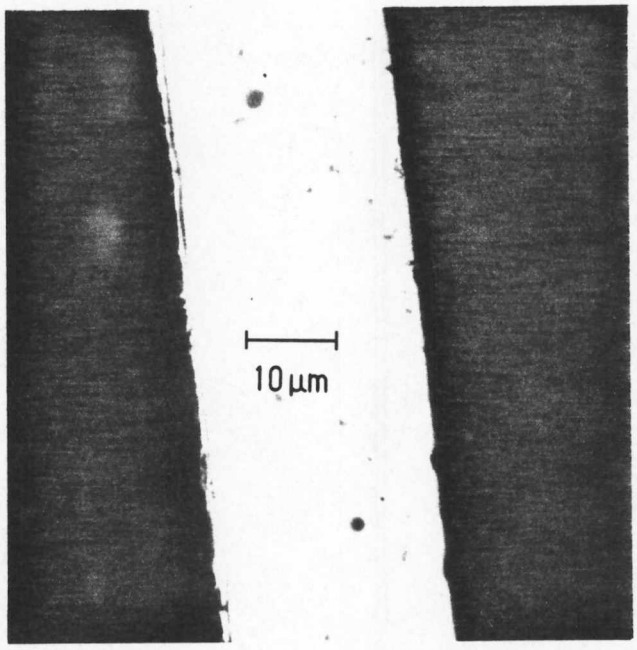


Fig. 40 - The amorphous layer formed on laser irradiation on an $Fe_{90}Zr_{10}$ alloy. The layer thickness is about 1.5µm.

CHAPTER 7

DISCUSSION

Some understanding of Fe based alloy systems can be gained if the transformation in unalloyed iron under extreme cooling rates is first studied. An optimum energy density should be found that may uniformly be applied to all the alloys for melting. This energy density should give maximum melting depth with least surface damage. The surface damage becomes a crucial factor if the process is to be made industrially viable.

7.1 Pure Iron

The results for pure iron indicate $3.0 J/cm^2$ as the optimum energy density which favorably satisfies both conditions viz., maximum melt depth with least surface damage. Higher energy densities are obtained by adjusting the optics of the system so as to concentrate all the energy in a smaller area. The KrF laser used in the pure iron experiments has a line focus rather than a point focus because of different divergence angles in the vertical and horizontal planes. This results in a non-uniform beam intensity distribution as discussed earlier. As can be seen from Figure 18, the melt depth tends to saturate with the energy density. This is due essentially to increased evaporation at these power levels. Surface evaporation has also been detected by luminescence / reflectivity measurements. An increase in the energy level due to decreased reflectivity will produce an increase in evap-

oration especially in the region first melted and the surface damage will also be increased in the same manner as shown in Figure 13.

This mechanism of surface damage can be better understood by correlating it with the metal surface reflectivity[5]. The beam energy dependence of the surface temperature is given by the relation,

$$dT/dt \simeq P(1-R) \; / \; \rho C_p \delta$$

where P is the instantaneous power density, R is the reflectivity, ρ is the density, C_p is the heat capacity and δ, the thickness where heat is absorbed.

Because C_p is a strong function of temperature and usually increases with temperature, a spatial fluctuation in the beam intensity does not lead to large changes in the surface temperature and thus the entire surface is more or less at uniform temperature. But when the reflectivity R strongly decreases with temperature, as is the case with most metals for the visible light wavelength range, small fluctuations of the incident beam energy would lead to a large variation in the temperature of the surface resulting in an extensive surface damage. This is more so at the time of melting when R decreases suddenly resulting in an unstable situation. Extensive damage is possible at such unstable situations. The two cases explained above are shown in Figure 41. The behaviour in curve 'c' results in very little surface damge whereas curve 'b' corresponds to most metals which show extensive surface damage. In curve 'a', the temperature rises linearly with incident energy.

Lower energy densities are associated with lower melt depths. The evidence of melting is confirmed by the presence of a uniform rim that

Case 'a': T linear with I
case 'b': Large temperature fluctuation for fixed ΔI
case 'c': Small temperature fluctuation for the same ΔI

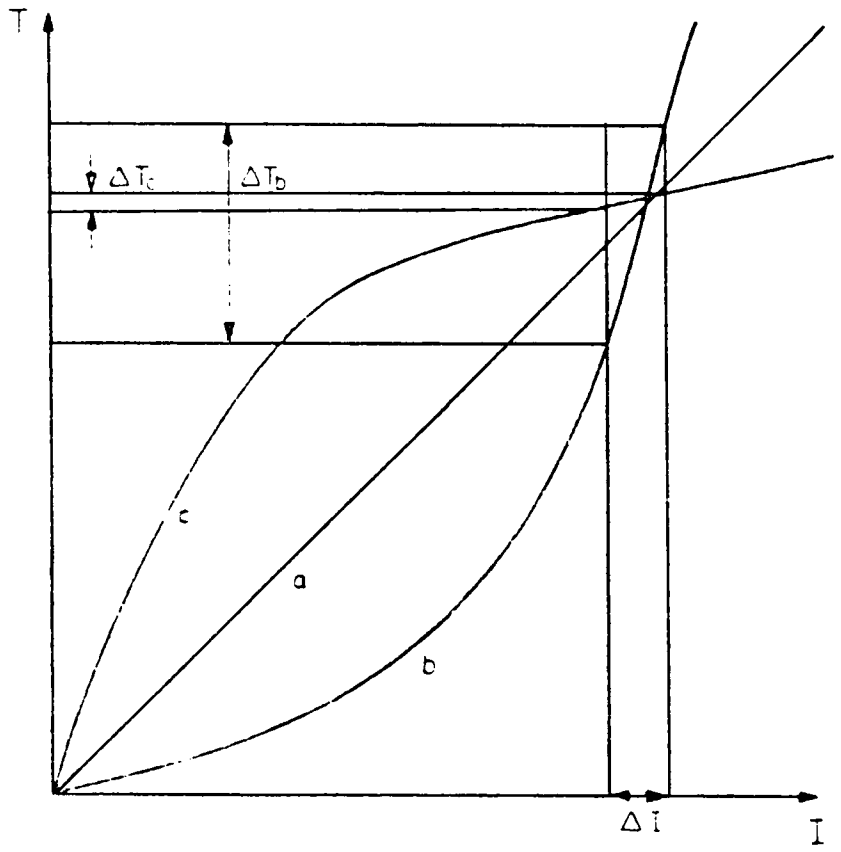


Fig. 41 - Schematic temperature vs. beam intensity curves showing the temperature fluctuation ΔT caused by a fluctuation in the beam intensity ΔI in various cases.

Source: M. von Allmen, "Laser and Electron Beam Processing of Materials" edited by C.W.White and P.S.Peercy, Materials Research Society (1980), 6

is found along the edge of the spot. Though at lower energies some regions are slightly marked by a sequence of dark and light strips, this is due to diffraction of the laser light by the edge of the masking tape. These marks can not be taken as an evidence of uniform melting because at that spot, the intensity can be up to four times larger than the nominal intensity of the incident laser beam. Therefore the choice of the $3.0J/cm^2$ energy density seems to be appropriate in order to have a considerable melt depth ($\simeq$ 1μm) with low surface damage.

The reflectivity measurement shown in Figure 14 that exhibits an enormous increase in absorbed energy during the time the laser was active, strongly indicates the formation of a hot plasma during the process of laser irradiation. In fact Walter and others[72] have studied the optical properties of a copper sample irradiated with a Q-switched Ruby laser. They observed that when the power is increased to $9x10^8 W/cm^2$, the surface temperature rises above the boiling point of the material and forms a plasma on the surface. They measured the line spectrum emitted by the 'light flash' which was the result of plasma formation and found that it contained neutral Cu atoms, Cu ions and Cu^{2+} dimers. Lin[38] has also discussed plasma formation on metallic surfaces during high power laser irradiation in his experiments with a picosecond laser. The presence of an increased radiation received during the reflectivity measurements, the 'light flash' and the generation of the loud sound during irradiation, as already discussed, lead us to believe that plasma formation really occurred while irradiating iron. This abrupt evaporation of the surface of the specimen may produce a shock wave. The effect of this shock wave upon the

dislocation microstructure of aluminum has been reported.[71] Lin[38] [90] observed and measured the pressure rise as a result of the shock wave generation in picosecond irradiation of metallic surfaces.

The possibility of surface evaporation has rarely been explored in most of the numerical models dealing with melting and solidification of metals during laser irradiation. The presence of plasma on the surface would be expected to strongly modify the heat transfer during this process. Hassanein[73] obtained that the vapor shielding drastically modified the surface temperature and the melted thickness, though the energy densities used for these calculations were 2 to 3 orders of magnitude higher than those obtained in excimer laser irradiation.

In contrast with the reflectivity measurements in the case of metals, evaporation seems to be negligible in semiconductors and reflectivity measurements give valuable information about the residence time of the liquid on the surface. Liquid silicon, unlike iron, exhibits higher reflectivity than the solid. Therefore the presence of the liquid can easily be detected with the increase in reflectivity. The nature of the heating and cooling curves differs substantially in the case of iron and of silicon. Figure 42 shows the melt depth-time profiles for silicon and aluminum to represent respectively the semiconductor and the metal behaviour.

Duflos and Cantor[50] have considered three different sequences of phase transformations as possible in pure iron and they are

1) L - δ - γ - α or the conventional equilibrium cooling sequence.

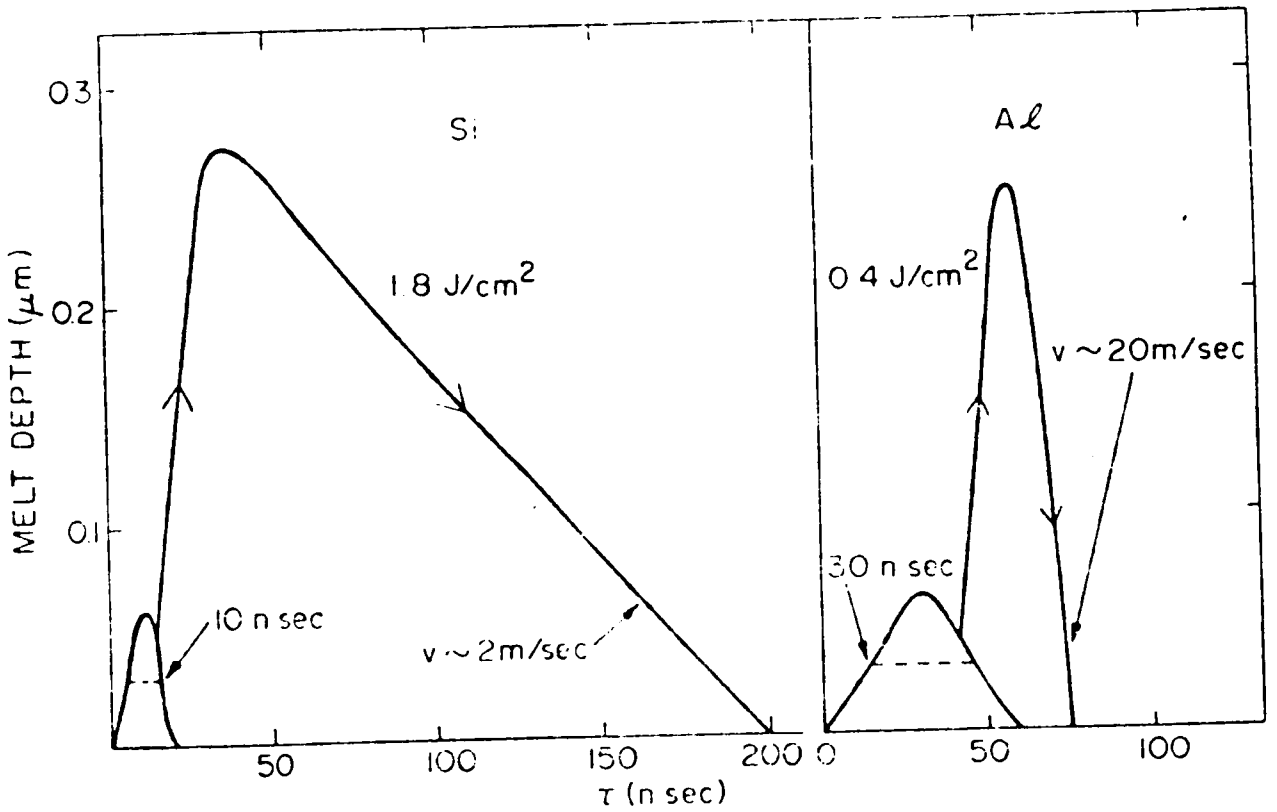


Fig. 42 - Position profiles of melt fronts in Si and Al after irradiation with a pulsed ruby laser.

Source: J.M.Poate, 'Surface Modification and Alloying by Laser, Ion, and Electron Beams' eds. J.M.Poate, G.Foti and D.C.Jacobson, Plenum Press, (1981), 5

2) L - γ - α because of the extreme undercooling present in such processes resulting in the suppression of δ and direct formation of γ and

3) L - δ as has been observed in splat quenching of some steels.

The authors have ruled out the retention of δ ferrite because of the relatively wide region of austenite stability.

In the present case of pulsed laser irradiation experiments, the presence of the crystalline surface and the external surface may influence the conditions under which the transformation takes place. The experimental results show that very large crystals are not changed in orientation and that the grain structure remains the same. If transformation from γ - α had occured during cooling, we certainly would expect the presence of martensitic laths as it has been already reported[74,75]. Moreover, if a massive reaction had taken place, we would expect the grain size much smaller than the original grain structure as reported by Duflos and Cantor.[50] This is because the maximum measured massive velocity of $\simeq$ 2cm/s would yield a maximum grain size of 4nm. But the results do not show any presence of fine grains in the structure. Moreover considering that our cooling rate is much higher than the one obtained by splat cooling, we should expect grain size smaller than the one reported in those experiments and certainly not single crystal as was observed.

The epitaxial regrowth of the melted layer is quite clear from the Laue back-scattering X-ray diffraction patterns (Figure 16) and

the photomicrographs showing no fragmentation of the grains and intact grain boundaries after the irradiation (Figure 15).

We can then conclude that during laser irradiation, the δ - γ phase transformation is avoided at variance with the case of splat quenching. Similar results were obtained by Buene and others[76] when they conducted some studies and reported the presence of epitaxial regrowth in the case of Ni and Fe. Their results suggest the possible absence of the δ to γ phase transformation. They irradiated their samples by raster scanning with 1.06μm focussed radiation from a Q-switched Nd:YAG laser operated at 11kHz with pulse duration of 130ns and a spot diameter of 35μm.

The microstructural analysis has indicated no signs of martensitic transformation in a number of samples. Hardness results are not quite conclusive because of the very low carbon content of the pure iron used. The results neither support nor contradict the possibility of martensitic formation. The presence of epitaxial regrowth, however, seems to indicate that the γ phase was suppressed during solidification.

The melt depth measurements done by the "step-by-step surface removal by mechanical polishing technique" are useful and match reasonably well with the theoretical calculations performed by Mehrabian et al.[6] The main feature of this method is the presence of the rim around the edges. This rim shows up as a bright circle (or rectangle depending on the shape of the masking window used) even after the surface layer has been removed partially. The rim does not show up in reflection type microscope, but must be observed holding the sample

at a slanting angle against the light and therefore it can not be shown in a photomicrograph.

Based upon these measurements, the fraction of laser beam energy used for melting can be estimated. This is shown in Appendix 2 and the result shows that about 54% of the incident energy is used for melting, confirming that the reflectivity of the polished surface is very low. Surface evaporation, as already discussed, may be the main cause of the substantial loss of incident energy.

7.2 Iron-Boron System

A technique developed to measure the melt depth produced by laser irradiation was tested on an iron alloy which is an easy glass former. $Fe_{80}B_{20}$ is known to be one of the most readily amorphized iron alloys. It has been extensively studied and many of its properties have been reported. The presence of a deep eutectic point and the large difference in the atomic radii of the two elements (a_{Fe} = 0.124nm and a_B = 0.046nm) make it feasible for the glass to form at high cooling rates (10^6K/s).

Sample preparation by sintering of compacted pellets and subsequent annealing was chosen because it involves lower than melting temperatures, thus avoiding Boron evaporation. Moreover, the possibility of contamination is reduced because there is no liquid present during the entire process. However, entrapped gases during compaction may diffuse into the lattice and the desired purity may not be maintained. In order to reduce this effect, the material was baked out under

10^{-6}torr. The voids present were of no concern because the sintered material was eventually melted.

The surface sensitive X-ray diffraction (SSXD) method was developed to study the changes that take place in the near surface region as a result of a surface modification treatment. One of the most important criteria for the selection of the target material for the X-ray source is the ability of the X-rays to penetrate about double the thickness of the affected layer. It is necessary that more than 60% of the diffracted intensity come from the layer that has undergone some kind of a change for the method to be accurate. In other words, it is essential that part of the beam penetrate the unaffected substrate material. Otherwise the method will not measure the precise thickness of the modified layer. Thus the X-ray source selection for performing the measurements on a particular test material will depend upon the thickness of the modified layer. If the modified layer is thick, say of the order of 20-30μm, then an X-ray source ordinarily used for detecting massive structural changes is adequate. However, if the modified layer is thin, say about 1-2μm, then a different source is required so that the test material has a very high absorption coefficient for the corresponding X-ray wavelength.

In our study, the SSXD technique has been used for the measurement of the amorphous layer thickness formed on the surface after laser irradiation. The method by itself is quite general in nature. It can determine the amount of crystalline volume fraction present in the amorphized layer that has the same crystal structure as the substrate along with the amorphous layer thickness. We, however, used a simpli-

fied formula where the crystalline volume fraction in the amorphous layer is assumed to be zero. This simplification is valid for $Fe_{80}B_{20}$ because of its ease of glass formation. Microstructural examination of the amorphized layer showed an absence of any crystalline phase.

This assumption, however, does not hold true in all the glass forming systems. Competitive growth of a crystalline phase in an amorphized surface formed by excimer laser irradiation in Cu-Ti alloys has been reported and discussed on thermodynamic grounds by Massalski et al.[77] Thus the simplification will not be true for this system. In X-ray diffraction experiments, however, if one of the constituents is less than 5% by volume, it is not easily detected. Another instance where the presence of a crystalline phase does not affect the results to a considerable extent is where the crystalline phase has a crystal structure different from that of the underlying substrate. In this case, crystals in the amorphous layer simply behave as an absorbing medium to the incident and the diffracted X-ray beam. The diffraction peaks from these crystals are different from those of the substrate. In other words, they do not contribute any intensity to the peaks from the substrate and behave similar to an amorphous material as far as absorption is concerned. Thus the ratios of the intensities before and after laser irradiation can be used without any corrections to calculate the depth of the melted thickness as already explained.

The splat quenched samples as well as the sintered and annealed samples were used for the laser irradiation experiments. The results clearly show that the prior microstructure of the sample is very critical in determining whether the sample would amorphize or not. The

sintered and annealed samples have a very coarse microstructure. Thus the Fe_2B particles can be clearly seen in a ferrite matrix. However, in the splat quenched samples, the ferrite and the Fe_3B are so closely spaced that ordinary optical microscopy is unable to resolve the phase separation.

The presence of the metastable phase Fe_3B in the splat quenched samples is clearly indicated by the fact that under similar conditions used in the X-ray diffraction, the intensities of the (110) and the (220) peaks are almost halved in the case of the splat quenched sample when compared with those in the sintered sample. In an Fe-20at%B alloy, 60 atoms of iron are required to be associated with 20 atoms of Boron to form Fe_3B whereas only 40 atoms of iron need to be attached to 20 Boron atoms to form Fe_2B. Thus the sintered and annealed structure has 40 atoms to form α iron (assuming the solubility of boron in α iron to be zero) whereas splat quenched sample has only 20 atoms available to form α iron. Thus the intensities should fall to half the value from the equilibrium annealed specimen to the splat quenched specimen, in agreement with the X-ray diffraction patterns of the respective samples, Figure 23.

The presence of Fe_3B helps the amorphization process, because Fe_3B contains 25at.% B which is closer to the nominal 20at.% B composition. This composition is known to be an easy glass former.

7.3 Iron-Zirconium System

The Fe-Zr system was studied to characterize its glass forming tendency and help to understand the Fe-B-Zr ternary system. This

ternary system has been found to produce amorphous alloys with 10-15at% B and 20-30at% Zr. These compositions have a crystallization temperature in the range of 620K to 970K. T_x, the crystallization temperature for glassy materials is defined as the temperature at which the glass transforms to a crystalline form. It is necessary for the glassy materials to have T_x high enough so that the glass does not crystallize at the intended working temperature in a reasonable lifetime in such applications as electric motors and transformers. In case of surface glazing, a high T_x ensures that the overlapped region is not crystallized during successive scans.

The Fe-Zr system has a fairly deep eutectic at 8.8at% Zr and therefore alloys in the vicinity of this composition are known to readily amorphize. In our case, $Fe_{90}Zr_{10}$ and $Fe_{88}Zr_{12}$ amorphized when splat quenched, but $Fe_{95}Zr_5$ and $Fe_{85}Zr_{15}$ did not. Thus cooling rates of 10^6K/s are not sufficient to amorphize zirconium contents little further away from the eutectic point. The X-ray diffraction showed that splat quenched $Fe_{90}Zr_{10}$ and $Fe_{88}Zr_{12}$ films were completely amorphous. But optical microscopy and TEM work done later showed that in some specimens, crystalline phases are present. Clearly, substantial amount of crystalline phases are not present in the near surface region since the X-rays did not detect them. Even if present near the surface, they ought to be in small amounts.

Three different kinds of crystals embedded in the amorphous matrix were characterized. One type of crystal has a spherulitic shape with branching of the two phases clearly seen. The individual phases could not be identified, but it is likely that they are a mixture of ferrite

and Fe_2Zr judging from the microstructure in Figure 31. All these crystals seem to have a zirconium rich center particle first formed and subsequent crystal growth occurs radially outward like branching until individual crystal growth is inhibited by another nearby crystal.

Along with the spherulites, there are two more types of crystals embedded in the amorphous matrix. One of the types is extremely rich in Zr and has a BCC structure similar to that of β-Zr. The other type is iron rich and also has a BCC structure. The reason why Zr-rich crystals form in an alloy that has only 10at% zirconium is not clear. From a thermodynamic point of view, it is expected that the liquid would have a very deep free energy curve because of the highly negative enthalpy of mixing.(-28 kcal./g-atom) Most probably, there are kinetic reasons that determine this behaviour. The formation of the Fe-rich particles, however, can be explained by the nature of the free energy curve. At 1500°C, the liquid is stable over the entire range except at the Fe-rich side where the fine particles of ferrite precipitate out. Since the cooling continues at a very rapid rate, the remaining liquid then transforms to glass inhibiting any further growth of the already formed crystals.

The Zr-rich particles are about 500-1000nm in size whereas the Fe-rich particles are only 10-20nm. This difference in size of 1.5 to 2.0 orders of magnitude implies that the Zr-rich particle formed much before the Fe-rich particle which is consistent with the Zr-rich particle having been solidified near 1800°C. (1870°C is the melting point of pure zirconium) The Zr-rich particles had about a 30μs longer growth time than the Fe-rich particles which formed at about 1500°C for an

assumed cooling rate of 10^7K/s. The fact that both phases are BCC implies that β-Zr, a high temperature phase, is retained at room temperature.

One of the $Fe_{90}Zr_{10}$ samples showed a very unusual feature of having two narrow bands of crystals about 9-10μm from the surfaces of the splat quenched specimen in the otherwise amorphous structure. The mode of formation of this unusual sequence can only be hypothesized. The possibility of segregation in the liquid state may have been the cause of the crystal growth. But its presence precisely parallel to the surface is difficult to explain. One possible reason for the crystal formation is the momentary reduction in cooling rate as a result of the recoil of the hammer after the initial impact with the anvil. In that case, the high cooling rate can be reestablished on second impact giving rise to a second phase of amorphization.

The chemical composition analysis of the larger particles was done by the EDAX method on the SEM. For smaller particles, the composition analysis was done using a STEM. The results from the STEM analysis are reported elsewhere.[78]

The homogenization of the liquid is a critical stage that has to be reached in order to ensure that the proper composition for amorphization is achieved. This homogenization can be obtained in two different ways. First, by having a very fine starting microstructure that will permit the homogenization by diffusion while the material remains liquid and second, by having the solid already homogenous before melting. In the first case, an approximate estimate of the maximum

dimension that will allow amorphization (homogeneous liquid) can be obtained by using the random walk approximation,

$$x = \sqrt{2Dt} \simeq 45nm$$

where D is the diffusion coefficient in the liquid ($\sim 10^{-4} cm^2/s$) and t is the residence time of the liquid which for our experiment can be estimated as twice the pulse duration.(see Fig. 42)

In agreement with this estimate, a microstructure with grains of the order of 50nm (Fig. 36) produces a fully amorphous structure after laser irradiation while one with 500nm grain size (Fig. 39) does not, clearly indicating that diffusional homogenization is the most predominant homogenization mechanism in the laser irradiation experiments.

In the case of laser irradiation of $Fe_{80}B_{20}$ sample in as sintered and annealed condition, we have detected the presence of convective mixing. But that may have been caused because of the large grain size. The sudden volume expansion due to melting would be sizable leading to convective mixing at the grain boundaries. This effect is negligibly small, however, in the case of fine grained microstructures such as those observed in splat quenched specimens.

Chumbly[79] amorphized a Ti-5at%Si alloy by melt spinning, but a crystalline material was obtained when that alloy was processed with a continuous CO_2 laser in spite of the higher cooling rate attainable with the laser. The original coarse starting microstructure in the latter experiment together with the low solid solubility of Si in α-Ti are the causes of this apparent contradiction. Similar results were obtained by Jain et al[80] further stressing the importance of the initial microstructure conditions in laser processing.

An important result out of these laser irradiation experiments is that there is an increase in the range of composition which could become amorphous. Three of the four samples - Fe-10, 12 and 15at%Zr-amorphized on laser irradiation, as against only Fe-10 and 12at%Zr alloys which amorphized on splat quenching. This may be attributed to the increased cooling rate that can be attained by the excimer laser compared with that attained in more conventional techniques such as splat quenching.

CHAPTER 8

CONCLUSIONS

8.1 Pure Iron

1) The optimum energy, i.e. maximum melt depth with minimum surface damage, for excimer laser processing is $3.0 J/cm^2$.

2) The extremely high cooling rates obtained during laser processing ($\sim 10^{10}$-10^{11} K/s) inhibit the δ to γ solid state phase transformation in pure iron.

3) The 'light flash' detected during laser irradiation by reflectivity measurements indicate that a hot plasma is produced each time the laser pulse strikes the sample.

4) The melt depth in pure iron as determined by 'step-by-step surface removal by mechanical polishing' is of the order of 1.0-1.5 μm.

8.2 Iron-Boron System

1) The surface sensitive X-ray diffraction (SSXD) technique can be used to determine the average thickness of the amorphous layer with a high degree of accuracy.

2) Splat quenching of Fe-B alloys produces the Fe_3B metastable phase in ferrite.

3) The prior microstructure of a sample is important in determining whether the sample will amorphize or not on laser irradiation. The finer the microstructure, the higher the probability of amorphization. This is so because finer microstructure implies

better surface homogenization which is a key to the process of amorphization.

8.3 Iron-Zirconium System

1) Amorphous and crystalline phases can form simultaneously in a sample that has been rapidly solidified.
2) The compositional range for amorphization in Fe-Zr system is widened in excimer laser processing as compared to conventional rapid solidification techniques.
3) Splat quenching of Fe-Zr alloys produces the Fe_2Zr metastable phase together with ferrite.
4) Different conditions in the hammer and anvil apparatus produce a range of metastable phases. For instance, for sample weight of 40mg, an amorphous alloy is produced while with a 120mg sample, a mixture of crystalline metastable phases is produced.
5) In laser processing, the thickness of the amorphous layer is a function of the Zr content.

LIST OF REFERENCES

LIST OF REFERENCES

1) N.Bloembergen, "Laser-Solid Interactions and Laser Processing - 1978" Materials Research Society Publication edited by S.D.Ferris, H.J. Leamy and J.M.Poate, (1979),1

2) L.E.Greenwald, E.M.Breinan and B.H.Kear, "Laser-Solid Interactions and Laser Processing -1978" Materials Research Society Publication edited by S.D.Ferris, H.J.Leamy and J.M.Poate, (1979), 189

3) See F.Wooten, "Optical Properties of Solids", Academic Press, (1972)

4) See "Thermophysical Properties of High Temperature Solid Materials (TPRC)" Vol. I, The McMillan Company, New York (1967), 602

5) M. von Allmen, "Laser and Electron Beam Processing of Materials" edited by C.W.White and P.S.Peercy, Materials Research Society (1980), 6

6) R.Mehrabian, S.Kou, S.C.Hsu and A.Munitz,"Laser-Solid Interactions and Laser Processing -1978" Materials Research Society Publication edited by S.D.Ferris, H.J.Leamy and J.M.Poate, (1978), 129

7) S.C.Hsu, S.Chakravorty and R.Mehrabian, Metall. Trans., 9B, (1978), 221

8) L.Buene, D.C.Jacobson, S.Nakahara, J.M.Poate, C.W.Draper and J.K.Hirvonen, MRS Symposium "Laser and Electron Beam - Solid Interaction and Materials Processing" Vol. I edited by J.F.Gibbons, L.D.Hess and J.W.Sigmon, 1, (1981), 583

9) L.Buene, E.N.Kaufmann and C.M.Preece, MRS Symposium " Laser and Electron Beam - Solid Interaction and Materials Processing " Vol. I edited by J.F.Gibbons, L.D.Hess and J.W.Sigmon, 1, (1981), 591

10) See "Physical Metallurgy" edited by R.W.Cahn, North-Holland, (1965), 661

11) G.F.Bolling and D.Fainstein, Phil. Mag., Ser.8, 16, (1971), 45

12) B.P.Fairand and A.M.Clauer, "Laser - Solid Interactions and Laser Processing" edited by S.D.Ferris, H.J.Leamy and J.M.Poate, AIP Conf. Proc., (1978), 27

13) D.Lowndes, Solid State Division at Oak Ridge National Laboratorry - Private communication.

14) G.E.Possin, H.G.Parks and S.W.Chiang, "Laser and Electron Beam - Solid Interaction and Materials Processing" Vol. I edited by J.F.Gibbons, L.D.Hess and J.W.Sigmon, North Holland, 1, (1981), 73

15) T.R.Anthony and H.E.Cline, Jour. of Appl. Phys., Vol 48 No. 9, (1977), 3888

16) W.Klement Jr., R.H.Willens, and P.Duwez, Nature, 187, (1960),809

17) D.E.Polk and B.C.Giessen, ASM Seminar on Metallic Glasses, (1976)

18) J.Dixmier and J.F.Sadoc, Metallic Glasses, ASM (1978),97

19) M.R.Hoare and P.Pal, Adv. Phys., 20, (1971), 161

20) R.L.Maitrepierre, J. Appl. Phys., 40, (1969), 4826

21) K.Sinha and P.Duwez, J. Phys.and Chem. Solids, 32, (1971), 267

22) C.H.Bennet, J. Appl. Phys., 43, (1972), 2727

23) D.J.Adams and A.J.Matheson, J. Chem. Phys., 56, (1972), 1989

24) J.F.Sadoc, J.Dixmier and A.Guinier, J. Non Cryst. Sol., 11, (1972), 179

25) D.Turnbull, Contemp. Phys., 10(5), (1969), 473

26) D.M.Kroeger, W.A.Coghlan, D.S.Easton, C.C.Koch and J.O.Scarbrough, J. Appl. Phys., 53, (1982), 1445

27) M.Ohring and A.Haldipur, Rev. Sci. Instrum., 42, (1971), 530

28) H.S.Chen and C.E.Miller, rev. Sci. Instrum., 41, (1970), 1237

29) R.E.Maringer and C.E.Mobley, J. Vac. Sci. Tech., 11, (1974), 1067

30) R.E.Maringer, C.E.Mobley and E.W.Collings, in Proc. Second Internat. Conf. on Rapidly Quenched Metals, Section I, edited by N.J.Grant and B.C.Giessen, MIT Press, Cambridge, Massachusetts (1976), 29

31) S.Kavesh, Metallic Glasses, ASM, (1978), 36

32) M.H.Cohen and D.Turnbull, J. Chem. Phys., 31, (1959), 1164

33) S.Takayama, J. Mater. Sci., 11, (1967), 313

34) T.Masumoto and R.Maddin, J. Mater. Sci., 19, (1975), 1

35) D.E.Polk and B.C.Giessen, Metallic Glasses, ASM, (1978), 18

36) D.E.Polk, Acta. Met., 20, (1972), 485

37) P.Duwez, R.H.Willens and R.C.Crewdson, J. Appl. Phys., 36, (1965), 2267

38) Lin, Chien-Jung, Ph.D. Dissertation, Harvard University, (1983)

39) D.Turnbull, Contemp. Phys., 10, (1969), 473

40) E.R.Buckle and A.R.Ubbelohde, Proc. Roy. Soc., 259A, (1960), 325

41) D.R.Uhlmann, J. Non-cryst. Solids, 7, (1972), 337

42) H.A.Davies, J.Aucote and J.B.Hull, Scripta. Met., 8, (1974), 1179

43) S.Fujime, Jap. Jour. of Appl. Phys., 5, (1966), 1029

44) V.M.Amonenko, L.N.Ryabchikov, G.F.Mikinskii and V.A.Finkle, Dokl. Akad. Nauk SSR, 128, (1959), 977

45) H.Konig, Naturwis., 3, (1946), 71

46) Yu.G.Mikhailov, E.I.Nikulin, N.M.Reinov and A.P.Smirnov, Soviet Phys.- Tech. Phys., 4, (1960), 844

47) B.G.Lazarev, A.I.Sudovtsov and E.E.Semenenko, Soviet Phys.- JETP, 13, (1961), 75

48) M.R.Bennet and J.G.Wright, Phys. Stat. Sol., (a) 13, (1972), 135

49) W.Felsch, Z.Phys., 195, (1966), 201

50) E.Duflos and B.Cantor, Acta. Metall., 30, (1982), 323

51) Y.Shimoda and H.Kajima, J. Appl. Phys., 47, (1976), 4156

52) G.Marchal, Ph.Mangin and Chi.Janot, Solid State Comm., 18, (1976), 739

53) G.Marchal, Ph.Mangin, M.Piecuch and Chi.Janot, J. Physique, C6, (1976), 763

54) G.Suran, H.Daver and J.C.Bruyere, AIP Conf. Proc., 29, (1976), 162

55) G.Suran, H.Daver and J.Systern, Physica, 86-88B, (1977), 810

56) G.Suran, H.Daver and J.Systern, AIP Conf. Proc., 34, (1976), 310

57) N.Kazama, N.Heiman and R.L.White, J. Appl. Phys., 49(3), (1978), 1706

58) A.K.Sinha, J. Appl. Phys., 42(1), (1971), 338

59) M.Takahashi and M.Koshimura, Jap. J. Appl. Phys., 16, (1977), 1711

60) E.Coleman, Tech. Mem. TM 78-1521-42, Bell Labs, Murray Hill (1978)

61) M.Naka, T.Masumoto and H.S.Chen, J. Phys. Colloque., 41 C8 Suppl.8, (1980), 53

62) L.A.Davies, R.Ray, C.P.Chou and R.C.O'Handley, Scripta. Met., 10, (1976), 541

63) M.Naka, S.Tomizawa, T.Masumoto and T.Watanabe, Rapidly Quenched Metals, Second Internat. Conf., Section I, edited by N.J.Grant and B.C.Giessen, MIT Press, (1976), 273

64) R.C.O'Handley, R.Hasegawa, R.Ray and C.P.Chou, Appl. Phys. Lett., 29, (1976), 330

65) U.Koster and U.Gerold, in "Glassy Metals I" edited by M.J.Guntherodt and H.Beck, Topics in Applied Physics, Springer-Verlag, 46, (1981), 225

66) M.Nose, K.Esaki and T.Masumoto, Abstract of annual meeting of Japan Inst. of Met., 18, (1979), No.85, 340

67) K.H.J.Buschow, A.M.van Diepan, N.M.Beckmans and J.W.H.Biesterbos, Solid State Comm., 28, (1978), 181

68) M.Nose and T.Masumoto, Sci. Rep. Res. Insts. Tohoku Univ., 28A suppl., (1980), 232

69) B.M.Clemens and M.J.Suchoski, Appl. Phys. Lett., 47(9), (1985), 943

70) S.Ohnuma, M.Nose and K.Shirakawa, Sci. Rep. Res. Insts. Tohoku Univ., 29A, (1981), 254

71) W.F.Bates Jr., 'Application of Lasers in Materials Processing' ed. E.A.Metzbower, ASM(1979), 317

72) W.T.Walter, N.Solimene, K.Park, T.H.Kim and K.Mukherjee, 'Lasers in Metallurgy' eds. K.Mukherjee and J.Mazumder, Conference Proceedings, The Metallurgical Society of AIME, (1981), 179

73) A.M.Hassanein, Ph.D. Dissertation, Univ. of Wisconsin, (1982)

74) C.M.Wayman and C.J.Altstatter, Acta metall., 10, (1962), 992

75) K.P.Singh and J.Gordon-Parr, Acta metall., 9, (1961), 1073

76) L.Buene, E.N.Kaufmann, C.M.Preece and C.W.Draper, 'Laser and Electron-Beam Solid Interactions and Materials Processing' eds. J.F.Gibbons, L.D.Hess and T.W.Sigmon, MRS North-Holland, (1981), 591

77) T.B.Massalski and C.G.Woychik, Acta metall., 33, (1985), 1873

78) M.J.Godbole, G.L.Lehman and A.J.Pedraza, to be published

79) C.G.Woychik, D.H.Lowndes and T.B.Massalski, Acta metall., 33, (1985), 1861

80) S.Chumbly, Univ. of Illinois, Private Communication

APPENDICES

APPENDIX 1

A method for detecting and precisely measuring the thickness of an amorphous layer on a crystalline substrate has been developed. An X-ray diffractometer in parafocussing reflection geometry is used, the target being selected so that the emitted X-rays are strongly absorbed by the specimen.

The integrated intensity of each diffracted beam for the specimen arrangement used in the diffractometer is given by,

$$dI_d = \frac{I_o ab}{\sin\Theta} \exp\left(-\frac{2\mu x}{\sin\Theta}\right) dx$$

where I_0 is the intensity of the incident beam, a is the specimen volume fraction having particles with the right orientation for diffraction, b is the fraction of I_0 that is diffracted per unit volume, μ is the linear absorption coefficient, θ is the Bragg angle and x is the penetration distance normal to the specimen surface. For a thick and uniform specimen,

$$I_d = \frac{I_o ab}{2\mu}$$

If there is an amorphous surface layer of thickness δ present, containing a uniform dispersion of crystalline phase whose volume fraction is v, we must take the contribution from both the crystalline portion in the amorphous layer and the substrate. The contribution from the amorphized layer is given as,

$$I_d = \frac{I_o b}{2\mu'} v a_i^{\ell} \left\{ 1 - e^{-2\mu'\delta/\sin\Theta} \right\}$$

where μ' is the linear absorption coefficient of the layer and superscript ℓ stands for the layer. Similarly, the diffracted intensity from the substrate is given as,

$$I_d' = \frac{I_o' b}{2\mu} a_i^{s} \qquad\qquad I_o' = I_o e^{-\mu'\delta/\sin\Theta}$$

However, this intensity is further attenuated by a factor $\exp(-\mu'\delta/\sin\theta)$ when the diffracted beam goes through the upper layer. Therefore, the total diffracted intensity is

$$I_d' = \frac{I_o b}{2\mu} \left\{ \frac{\mu}{\mu'} a_i^{\ell} v \left[1 - exp\left(-\frac{2\mu'\delta}{\sin\Theta}\right) \right] + a_i^{s} exp\left(-\frac{2\mu'\delta}{\sin\Theta}\right) \right\}$$

The ratio of the intensities before and after the layer is formed is given by,

$$R_i = \frac{I_d'}{I_d} = r_i^{\ell} v' [1 - exp(-\frac{2\mu'\delta}{\sin\Theta})] + r_i^{s} exp(-\frac{2\mu'\delta}{\sin\Theta})$$

$$r_i^{\ell,s} = \frac{a_i^{\ell,s}}{a_i} \qquad and \qquad v'\mu' = v\mu$$

gives the change in preferred orientation in the specimen after the layer is produced. r = 1 if there is no change. The subscript i refers to each diffraction peak.

Consider the first case where the crystalline orientation of the crystals embedded in the amorphous layer is the same as that of the

substrate and no changes have occured relative to the crystalline orientations of the original material. This assumption applies whether the crystalline orientations are or are not randomly distributed. This yields an implicit equation for v,

$$R_2 - v' = (R_1 - v')^{n_{12}} (1 - v')^{1-n_{12}}$$

$$n_{12} = \frac{sin\Theta_1}{sin\,\Theta_2}$$

and the indices 1 and 2 refer to any two peaks. The thickness can then be obtained from

$$\delta = \frac{sin\,\Theta_i}{2\mu'} \; ln\,(\frac{1 - v'}{R_i - v'})$$

using any ratio R_i and the corresponding Bragg angle $2\theta_i$. The expression shows that $v' = 1$ only when $R_1 = R_2 = 1$, as expected, while $v' = 0$ occurs when $R_2 = R_1^{n12}$.

If the produced layer is fully amorphous, i.e., $v = 0$,

$$R_i = r_i^s \, exp\,(-\frac{2\mu'\delta}{sin\,\Theta_i})$$

then, selecting two diffraction peaks that will have the same value of r^s, e.g. the (110) and (220) in a BCC material, the magnitude of δ can be determined from

$$\delta = \frac{P}{2\mu'} \ln \frac{R_1}{R_2}$$

$$P = (\sin\Theta_2)^{-1} - (\sin\Theta_1)^{-1}$$

In the case where the substrate has not changed, on the average, its crystalline orientation, $r_i = 1$ for all the peaks, and then

$$\delta = \frac{\sin\Theta_i}{2\mu'} \ln R_i^{-1}$$

yields an independent evaluation of δ from each line. The multiplicity of lines thus offers the possibility of testing the validity of the assumptions made in deriving the final form of the expression and also of assessing the measurement error.

Another independent way of computing the thickness of the amorphous layer is to integrate the area under the diffuse halo obtained in the diffraction pattern of the specimen and compare it to the area under the halo of a fully amorphous sample of the same composition. The ratio of the two areas (which is a measure of the intensities) is

$$R_a = \frac{I_a^\delta}{I_a} = \frac{\int_{\Theta_a - \Delta\Theta}^{\Theta_a + \Delta\Theta} b'(\Theta) \left[1 - \exp\left\{-\frac{2\mu'\delta}{\sin\Theta}\right\}\right] d\Theta}{\int_{\Theta_a - \Delta\Theta}^{\Theta_a + \Delta\Theta} b'(\Theta)\, d\Theta}$$

where θ_a is the angle around which the halo is centered, $2\Delta\theta$ is the angular extension of the halo and b' is the fraction of energy diffracted per unit volume per unit angle at θ In the cases considered

here, it has been found experimentally that $b'(\theta)$ is an approximate symmetric function of θ around θ_a. When the exponential factor varies linearly with θ in the integration interval $2\Delta\theta \simeq 6°$, the following approximation may be used

$$\int_{\Theta_a - \Delta\Theta}^{\Theta_a + \Delta\Theta} b'(\Theta) \exp\left\{-\frac{2\mu'\delta}{\sin\Theta}\right\} d\Theta \simeq \exp\left\{-\frac{2\mu'\delta}{\sin\Theta_a}\right\} \int_{\Theta_a - \Delta\Theta}^{\Theta_a + \Delta\Theta} b'(\Theta)\, d\Theta$$

In this approximation,

$$\delta = \frac{\sin\Theta_a}{2\mu'} \ln\,(1 - R_a)^{-1}$$

APPENDIX 2

Assume that the temperature of the molten layer rises from room temperature(25°C) to 1600°C uniformly. Various constants are listed below,

C_p (Fe α) = 4.18 + 5.92x10^{-3}T cal/degree-mole

from 298 K to 1033 K.

C_p (Fe β) = 9.00 cal/degree-mole

from 1033 K to 1181 K.

C_p (Fe γ) = 1.84 + 4.66x10^{-3}T cal/degree-mole

from 1181 K to 1674 K.

C_p (Fe δ) = 10.5 cal/degree-mole

from 1674 K to 1808 K.

C_p (Fe ℓ) = 10.0 cal/degree-mole

from 1808 K to 1873 K.

for Fe α - Fe β, ΔH_{trans} = 1200 cal/mole at 1033 K.

for Fe β - Fe γ, ΔH_{trans} = 220 cal/mole at 1181 K.

for Fe γ - Fe δ, ΔH_{trans} = 210 cal/mole at 1674 K.

for Fe δ - Fe ℓ, ΔH_{trans} = 3300 cal/mole at 1808 K.

Using these constants, ΔH for 1 mole of Fe to go from 298 K to 1873 K is

= 18470 cal/mole

= 330.7 cal/g

= 1383.6 J/g

Mass of the molten region per unit area is

$$= 1.5\text{x}10^{-4}\text{cm} \times 7.8\ \text{g/cm}^3$$

$$= 1.17\text{x}10^{-3}\ \text{g/cm}^2$$

Thus the energy required to raise the temperature of the molten region per unit area is

$$= 1383.6\ \text{J/g} \times 1.17\text{x}10^{-3}\ \text{g/cm}^2$$

$$= 1.62\ \text{J/cm}^2$$

Therefore the fraction of the incident energy(3.00J/cm^2) required to melt the layer is

$$= (1.62/3.00)\text{x}100$$

$$= 54\%$$

VITA

Mukund Janardan Godbole was born in Sangli, India on May 15, 1959. He attended elementary and secondary schools in that city and stood eighth in the state of Maharashtra in the Secondary School Examination. After one year of college at The University of Bombay, he attended The Indian Institute of Technology, Kharagpur, in 1976 and received the Bachelor of Technology degree in Metallurgical Engineering in June, 1981.

He accepted a job as a Junior Engineer after graduation at Tata Engineering and Locomotive Company and served for two years before entering The Graduate School of The University of Tennessee in September, 1983. He received the Master of Science degree with a major in Metallurgical Engineering in June, 1986.

The author had been actively involved in the student council in his undergraduate days where he served as the President of the council, in addition to many other positions. He represented his school in many cultural and sports activities. He is a student member of the American Society of Metals and The Metallurgical Society. He intends to continue his research activity and join the Doctoral program at The University of Tennessee.